Measurement and modelling of fast electron transport in solid materials

Rachel Jane Dance

Doctor of Philosophy

University of York

Physics

March 2014

Abstract

This thesis presents an investigation into the properties of relativistic electron beams generated by the interaction between an intense laser and a solid density target. Described are novel x-ray spectroscopic techniques for measuring the electron beam divergence, electron currents and to explore the electron distribution.

A key aim of this work is the constraint of fast electron beam parameters by the comparison of well characterised experimental data to computational plasma models. Multi-dimensional imaging of a single spectral line allows insight into heating and inferred spatially resolved temperatures, which are around 300eV, are compared to simulation. By comparison of imaging data and simulation, the electron beam is found to diverge with a half angle of approximately $70^\circ \pm 10^\circ$, and is found to have a diameter greater than that of the laser focal spot.

Measured hollow ion spectra are shown, and calculations imply that there are two distinct ionisation mechanisms. The generation of hollow ion states is seen to be dominated by photoionisation in the range of 7.2Å−7.7Å, and by collisional ionisation in the range 7.9Å−8.1Å. This implies the existence of an intense radiation field, and high fast electron flux within the target.

The velocity distribution of electrons is explored by observation of polarised x-ray emission. Using a pair of HOPG crystal spectrometers, each of the polarised components of the x-ray spectra are measured independently to obtain the degree of polarisation. The anisotropic population of magnetic sublevels results in a net polarisation in the spectral emission, and the polarisation degree measured is indicative of the degree of anisotropy in the velocity distribution of the return current. The large, positive degree of polarisation found implies that polarised emission is caused by the return current, and that it contains the necessary energy to excite ions into a hydrogenic state.

Contents

List of Figures

List of Tables

Acknowledgements

It is very hard to thank such a large group of people, but first I wish to thank Dr Nigel Woolsey for his supervision, and for creating opportunities for me throughout the last three or so years. I also gratefully acknowledge the funding provided by the EPSRC, and the support of the Fusion Doctoral Training Network at the University of York which have made this PhD possible. The University of York Department of Physics Research Services team, in particular Richard Armitage, Neil Johnson and Dave Coulthard for their hard work and support of experiments, and valued assistance in building the York Plasma Institute laser laboratory.

The experimental work in this thesis was made possible by the dedicated teams of staff and scientists at the Central Laser facility at the Rutherford Appleton Laboratory who work tirelessly to deliver successful experimental campaigns for the user community. Thanks also to Dr Alex Robinson and Dr Raoul Trines who continue to support computational work carried out in support of experimental data.

I would like to extend great thanks to my collaborators Dr Ingo Uschmann and Kai Schulze who it has been my great pleasure to work with. Their input and support with data analysis and experimental work has been invaluable. Thanks must also go to Martin Ramsay, for providing simulation results and support in the analysis of the experimental data. Thanks must also go to Dr Nicola Booth, Dr Sergey Pikuz and Dr James Colgan who by sharing experimental data and simulation expertise, allowing me to become involved in the ongoing analysis of experimental data relating to polarised x-rays and hollow ions.

I would like to thank Dr Erik Wagenaars, Dr John Pasley, Dr Kate Lancaster and Dr Andrew Rossall, for their unwavering support, optimism and humour throughout the last few years, no matter how tight the deadline or how stupid the question asked, and special thanks to Dr Koki Imada, without whom I have no doubt I would be still be fighting frustrating battles.

Thank you to the other kind students at York who have supported me, particularly Reem Alraddadi, Tom Fox, Scott Silburn and many others who have been a great help on numerous occasions. To those individuals who have endured long and often late night phone calls on physics or otherwise, you know who you are, and I am indebted to you for putting up with me in the trials of writing this thesis, it will not be forgotten.

Finally, to my family. For letting me find my own path. For always having faith in my decisions however abstract they must have seemed, and most importantly, for never letting me give up.

Declaration

I declare that the work presented in this thesis, except where it is otherwise stated, is based on my own research and has not been submitted previously for a degree in this or any other university. Parts of the work presented in this thesis have been published in:

Measurement and simulations of hollow atom X-ray spectra of solid-density relativistic plasma created by high-contrast PW optical laser pulses. High Energy Density Physics **9**, 3, 560-567 (2013) S.A. Pikuz, A.Ya. Faenov, J. Colgan, R.J. Dance, J. Abdallah, E. Wagenaars, N. Booth, O. Culfa, R.G. Evans, R.J. Gray, T. Kaempfer, K.L. Lancaster, P. McKenna, A.L. Rossall, I.Yu. Skobelev, K.S. Schulze, I. Uschmann, A.G. Zhidkov, and N. C. Woolsey

Exotic Dense-Matter States Pumped by a Relativistic Laser Plasma in the Radiation-Dominated Regime. Physical Review Letters **110**, 125001 (2013) J. Colgan, Jr. J. Abdallah, A. Ya. Faenov, S. A. Pikuz, E. Wagenaars, N. Booth, O. Culfa, R. J. Dance, R. G. Evans, R. J. Gray, T. Kaempfer, K. L. Lancaster, P. McKenna, A. L. Rossall, I. Yu. Skobelev, K. S. Schulze, I. Uschmann, A. G. Zhidkov, and N. C. Woolsey

Chapter 1

Introduction

Intense lasers striking a solid target create high currents of relativistic electrons. These beams of energetic electrons are capable of carrying large amounts of energy into solid material. Approximately 30% of the laser energy can be coupled into the target, allowing transport of energy to regions where the laser cannot reach. This has generated significant interest, and a large number of applications have emerged [1–3]. This thesis addresses fundamental aspects of the transport of these currents in high density materials. The approaches taken include experimental x-ray spectroscopy and computational spectroscopy and plasma simulation.

An application of particular interest is the fast ignition approach to inertial confinement fusion (ICF) [1]. The fast ignition approach uses the electron beam generated by an ultra-intense laser to heat a pre-compressed ICF target to thermonuclear temperatures. Critical to this work is the predictive understanding of the electron beam in the dense ICF plasma. The key parameters are the laser-electron beam coupling efficiency, the collimation or divergence of the beam and the beam temperatures. These same key parameters are critical to other applications which result from the production of secondary sources by the laser-solid interaction.

The propagation of high electron currents causes the acceleration of intense beams of protons [4, 5]. These energetic beams of protons can be used for a range of applications [6, 7]. Examples range from the use of plasma diagnostics [8], to the use of proton beams for oncology [9]. Proton beams have also been proposed as the

ignitor in a further development of the fast ignition scheme for fusion, which may benefit from lower angular divergence and advantageous energy deposition qualities [10].

Highly energetic beams of electrons can also produce very bright sources of x-rays [11] which have long been recognised for applications in medical imaging [12, 13]. In addition, matter at extreme conditions of temperature and density are produced in laser-plasma experiments, which allows these conditions relating to stellar and planetary interiors to be studied [14].

The key features of the complex interaction between an intense laser with a solid target is shown schematically in Figure 1. Some of the processes pertinent to this work will be explained in more detail in Chapter 2.

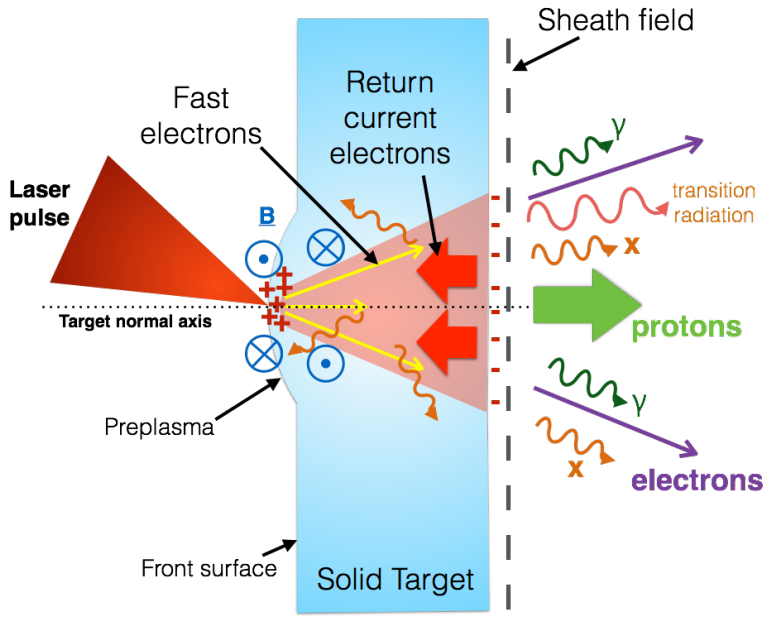

Figure 1.1: Interaction between an intense laser pulse and a solid density target. Fast electrons are generated at the front of the target and travel at an angle to the target normal axis towards the rear, setting up a large electric field. The large current of forward moving fast electrons causes the propagation of a return current. Self generated magnetic fields are also shown.

A high intensity laser is incident onto a solid density target from the left of Figure 1.1. As the laser strikes the front surface of the target it is rapidly heated, it becomes ionised and plasma is formed on the front surface. A beam of fast electrons

is accelerated away from the interaction region and a large current flows through the target. The fast electron beam travels through the target, typically at a large angle, known as the divergence angle, as depicted on Figure 1.1. This causes the production of a counter propagating return current beam that nearly balances the forward current. The return current is less energetic and results in collisional heating of the target. The fast electrons originate from the laser-target interaction region, and as they are accelerated away from this region leave behind positively charged material, an electric field is set up across the target. Sheath fields form at the rear surface of the target. These fields accelerate protons from the rear surface to high energies.

Although key parameters such as the angular divergence and electron beam current are conceptually simple, accurate and reliable measurement remains an ongoing task. Direct measurement of the electron beam is difficult and as such, experimental values are almost always by inference from related diagnostics. Measurements of hot electron beams have been made previously by optical diagnostics such as transition radiation and shadowgraphy, or by the emission of x-rays, each is described below.

The first application of x-ray spectroscopy to petawatt laser interactions with solid density matter showed time resolved measurement of x-ray spectra, deriving plasma temperatures of up to 600eV, and electron densities of 10^{23}cm^{-3} [15]. Such techniques continue to be applied [16, 17]. Electron beam divergence measurements are frequently made using the K-α spectral line to estimate the size of the beam at different depths into a target, either by observing the line emission from the rear surface, or from targets containing a buried layer [15, 18–21]. A review of electron beam divergence measurements has been carried out by Green et al. [19]. In this review it is noted that electron beam divergence increases from approximately 20° to 50° with laser intensity increasing from $5\times10^{18}\text{Wcm}^{-2}$ to $5\times10^{20}\text{Wcm}^{-2}$. It has been highlighted that K-α measurements may be affected by the electrons trapped in the target by the sheath fields generated at front and rear surfaces, creating an x-ray image that is wider than the electron beam [22].

Additionally, coherent transition radiation (CTR) may be used as a diagnostic tool. CTR is radiation emitted by electrons crossing the boundary between two materials with different dielectric properties, i.e. the target to vacuum boundary at the rear surface [23]. As electrons cross the boundary, optical radiation is emitted which propagates out into the vacuum. CTR provides evidence of fast electrons that initially escape the rear surface of the target. The size of the emission is used to estimate the size of the beam of fast electrons that escapes the target rear surface. This diagnostic has reported electron divergence angles of 17° from Al targets up to 400μm thickness [24], and of 16° from Al targets up to 100μm thickness [25]. Annular beam propagation and electron beam filamentation were also reported by the same authors.

Measurements of electron beam divergence have also been made by using shadowgraphy. In this method, the expansion of either the front or rear surfaces is diagnosed by casting a shadow onto the target by a transverse probe beam. The probe beam strikes the plasma and is refracted out of the laser line and an image is formed. The diagnosis of electron beam divergence is done by comparison of the size of the expansion of the front and rear surfaces, from the image created by an optical probe. Lancaster et al. [20] show a divergence angle of approximately 45° estimated by this method for incident laser intensities of $5\times10^{20}\mathrm{Wcm}^{-2}$.

1.1 Chapter overview

Chapter 2 This chapter outlines the theory underpinning the remainder of this thesis. The topics in this chapter can be broadly split into three main categories. These are the discussion of the laser and plasma parameters, fast electron transport, and spectroscopy / atomic physics. The laser and plasma parameters category aims to go through the key stages of the interaction in greater depth than is shown in Chapter 1. The Vulcan laser facility is reviewed, and key plasma physics topics are discussed. The elements of fast electron transport and atomic spectroscopy relevant to this thesis are also

summarised.

Chapter 3 This chapter details the diagnostics and instrumentation used in the collection of experimental data presented in this thesis. This chapter provides an overview of the Vulcan laser facility at which the experiments were carried out, giving an overview of the laser and at the laser focal spot profile temporally and spatially. The diagnostics used in this thesis are crystal spectrometers. X-ray diffraction from crystal surfaces is briefly summarised before an overview of each of the spectrometers in turn.

Chapter 4 This chapter details the experimental data collected by the 2D imaging crystal and toroidal crystal spectrometer to make measurements of the electron beam divergence angle. Details are included of the analysis and interpretation of the data.

Chapter 5 This chapter shows the experimental data collected by a focussing spectrometer with spatial resolution (FSSR) which was used to make measurements of x-ray emission from hollow atoms, in relation to the electron beam current.

Chapter 6 This chapter details the use of a pair of mosaic crystal spectrometers to measure the polarisation of x-ray emission arising from a laser-solid interaction. It also contains an investigation into the electron kinetics related to the source of this polarised emission.

Chapter 7 This chapter summarises the key conclusions of the thesis and highlights areas of further work.

1.2 Role of the author

The author contributed experimentally to all measurements made within this thesis. Analysis detailed in Chapter 4 is entirely the work of the author. Spectral analysis and simulation presented in Chapter 5 was the work of S. Pikuz and J. Colgan with input from the author. Simulation of the atomic cross sections was the work

of the author and is ongoing. Results presented in Chapter 6 are a sample of experimental data that is currently in preparation for publication. The analysis of the shot presented and all subsequent simulations have been completed by the author.

Chapter 2

Theory

2.1 Overview

In this chapter the key elements of plasma physics, spectroscopy and modelling methods that relate to this work are described. The interaction of the high intensity laser with a solid target rapidly heats and ionises the front surface and the laser pulse impacts on a plasma gradient at the target surface. This discussion begins with the plasma state and some fundamental parameters of the plasma, before moving on to important laser parameters. The absorption of the laser beam into the target and fast electron beam generation is also described with regards to the scalelength of the interaction. The propagation and transport of the beam are briefly discussed. An overview of the collisional radiative model and the assumptions of local thermodynamic equilibrium are discussed as they are used throughout the remainder of the thesis. A brief overview of the computational models that have been used in this thesis is given to be referred to in later chapters.

2.2 Plasma

Often called the 4th state of matter, plasma is seen in staggering variety. From the interiors of the many billions of stars in any given galaxy including our own, to the flame of a candle, plasma is frequently quoted to constitute 99% of all observable matter in the universe. The definition of a plasma is quoted directly from reference [26], *"A plasma is a quasineutral gas of charged and neutral particles which exhibits*

collective behaviour". In this context collective effects means that the electric and magnetic fields couple charged particles over large distances. A plasma is quasineutral. Electrons are attracted to the ions, until a sufficient number of electrons are accumulated to screen over a Debye length the charge from the remaining plasma. The charge from the ion and the surrounding electrons is balanced by the electrons in the Debye sphere for cold plasma. For a finite temperature, the shielding is imperfect as electrons can have sufficient energy to escape the electrostatic potential. The distance over which a plasma shields the electric potential is the Debye length, which is dependent only on the plasma temperature and density. Where the size of the plasma is many times larger than the Debye sphere the plasma is said to be quasineutral [26].

2.2.1 Plasma Frequency

If an electron in the plasma is perturbed from its equilibrium position and then released, it will overshoot its original position and oscillate about the equilibrium position with a characteristic frequency known as the plasma frequency ω_p. It is dependent only on the number density n_e, charge e and mass m_e of the plasma species in question, either electrons or ions. For electrons the plasma frequency is

$$\omega_p^2 = \frac{n_e e^2}{\epsilon_0 m_e} \tag{2.1}$$

where ϵ_0 vacuum permittivity. This frequency defines a fundamental timescale which characterises the ability of the plasma to respond to a perturbation [27].

2.3 Critical Density

The dispersion relation that describes the propagation of an electromagnetic wave in a plasma is given as [28]

$$\omega^2 = \omega_p^2 + k^2 c^2 \tag{2.2}$$

Where ω_p is the characteristic plasma frequency, k is the wavenumber of an incoming electromagnetic wave and c is the speed of light. In (2.2), if ω_p and ω become equal,

the wavenumber k must become zero. Therefore ω_p specifies a minimum frequency which an electromagnetic wave must have to propagate in the plasma. At this point the wave cannot propagate and is reflected or absorbed. Substituting in the plasma frequency from (2.1), a critical density can be defined beyond which a wave cannot propagate. By setting $\omega = \omega_p$, and including the relativistic correction factor γ,

$$n_{crit} = \frac{\epsilon_0 m_e \gamma \omega_L}{e^2} \tag{2.3}$$

This can be expressed for convenience in terms of the wavelength in micrometers, $\lambda_{\mu m}$ of the incoming wave and put into units of cm^{-3} this is rewritten as

$$n_{crit} \approx \gamma \frac{1.1 \times 10^{21}}{\lambda_{\mu m}^2} \ [\text{cm}^{-3}] \tag{2.4}$$

In the interaction of an intense laser beam with a plasma of increasing density, there is a density beyond which the laser cannot propagate. This density defines a critical surface from which the laser is reflected. For a 1μm laser, where $\gamma = 1$ the critical density $n_{crit} \approx 1 \times 10^{21}\text{cm}^{-3}$. The inverse dependence on the wavelength means that the critical density takes a higher value for shorter wavelengths, i.e. shorter wavelength lasers can propagate to higher density regions of the target. For the relativistic case where $\gamma > 1$, the laser is able to propagate to a density that is increased by the factor γ.

2.4 Single electron in a laser field

The Lorentz equation describes the force exerted on a point charge in an electromagnetic field. In this context this is the force exerted on the electron by electric and magnetic fields of the laser. The force $\mathbf{F}$ on the electron is given by the Lorentz equation.

$$\mathbf{F} = \frac{d\mathbf{p}}{dt} = -e(\mathbf{E} + \mathbf{v} \times \mathbf{B}) \tag{2.5}$$

Where $\mathbf{v}$ is the electron velocity, $\mathbf{B}$ and $\mathbf{E}$ are the magnetic and electric fields, and e is the electron charge. The momentum $\mathbf{p} = \gamma m_0 \mathbf{v}$ where m_0 is the electron rest mass and $\gamma = 1/\sqrt{1-\beta^2}$ and $\beta = v/c$. If the electron velocity is much less than the speed

of light, the electric field term $e\mathbf{E}$ is dominant, and the laser accelerates electrons along the direction of the electric field, or laser polarisation. If the electron velocity approaches c, the magnetic field term $-e(\mathbf{v}\times\mathbf{B})$ becomes large and its effects must be taken into account.

For a time varying electric field such as the laser field $E = E_0\cos(kx-\omega t)$, where k and x are the wave number and position, ω and t are the frequency and period of the wave. The electron has the following quiver velocity.

$$v_{qu}(r,t) = -\frac{eE_0}{m\omega_0}\sin(kx-\omega t) \tag{2.6}$$

The above equation 2.6 represents the non-relativistic electron motion in an electric field. The onset of the relativistic regime of laser pulses is indicated by the quiver velocity approaching the speed of light, and the addition of a gamma (γ) factor in the denominator of this equation. For a laser wavelength of 1μm, this implies that the electric field must be $E_0 \geqslant 5\times10^{11}\mathrm{Vm}^{-1}$ to cause $v_{qu}\simeq c$. This further implies that for a 1μm wavelength laser that the intensity must be greater than $1.37\times10^{18}\mathrm{Wcm}^{-2}$.

In the relativistic regime, the effect of the magnetic field term of the Lorentz equation ($\mathbf{v}\times\mathbf{B}$) becomes significant and accelerates electrons, perpendicular to the electric field. If there is a gradient in the electric field, as there is in a focussed laser beam, the ponderomotive force F_p,

$$F_p = -\frac{e^2}{4m_e\omega_L^2}\nabla\mathbf{E}^2 \tag{2.7}$$

pushes electrons towards regions of low field [28].

The normalised vector potential of a laser beam is a dimensionless quantity used to describe all lasers taking into account the peak intensity and pulse duration such that all lasers can be described. This vector potential a_0 is given by [29].

$$a_0 = \frac{eE}{\omega m_0 c} = (0.73 I_{18}\lambda_\mu m^2\ [\mathrm{Wcm}^{-2}\mu\mathrm{m}^2])^{1/2} \tag{2.8}$$

When $a_0 << 1$, the energy contained in the laser beam is not sufficient to accelerate electrons to relativistic speeds and $v_{qu} << c$. When $a_0 \geqslant 1$ the oscillation

of the electron in the laser field becomes relativistic. For a laser intensities of $5 \times 10^{20}\text{Wcm}^2$ and a wavelength of 1μm, $a_0 \approx 20$.

2.5 Laser contrast and plasma scalelength

In this section the scalelength and laser contrast are discussed. The scalelength is dependent on the contrast between the peak and background intensity of the laser and is important for the absorption of the laser light into the target.

2.5.1 Laser Contrast

High intensity laser pulses do not instantaneously reach their peak intensity, there is a finite rise time associated with the temporal profile of a laser pulse. The contrast of the laser pulse is the ratio between the pulse peak intensity, and the intensity of the laser light that precedes it. The contrast of a pulse at time frames of nanoseconds or picoseconds before the peak of the pulse. Figures of 10^{-10} of the peak intensity nanoseconds before the main pulse arrive are now achievable [30]. For example, a laser of peak intensity 10^{20}Wcm^{-2}, an intensity of 10^{10}Wcm^{-2} is present on the target surface for 1ns before the peak. This intensity can be enough to create plasma at the target front surface, and the main pulse peak arrives to find a plasma gradient already in place. This situation is sketched in Figure 2.1.

Figure 2.1 illustrates a laser entering density gradient present at the target front surface. The laser is able to propagate to the critical density at which point it is reflected. The density gradient is along the z axis.

2.5.2 Scalelength

The scalelength of the plasma is denoted as L_s, and is used to characterise the amount of plasma present as the main pulse strikes the front surface of the target. The density scalelength L_s is defined as

$$L_s = n_e \frac{dz}{dn_e} \approx c_s \tau_L \tag{2.9}$$

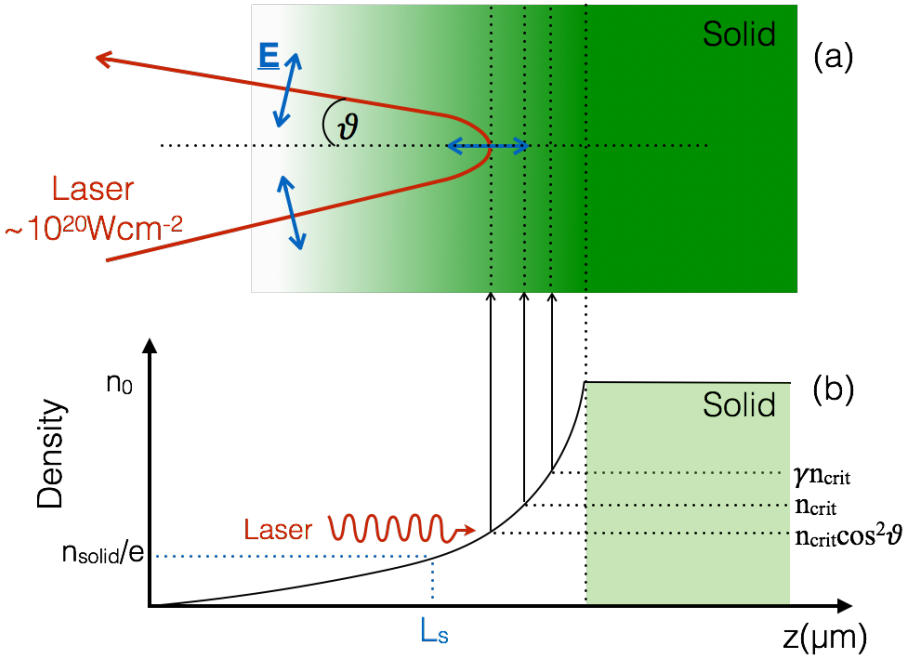

Figure 2.1: Schematic of a p-polarised laser beam incident on a density gradient in the z direction (a) The electric field of the incoming beam is perpendicular to the density gradient at the apex of the beam. (b) The laser propagates to the critical density, corrected for relativistic effects by γ, and is reflected or absorbed. The contrast of the laser is given as $I\lambda^2_{max}/I\lambda^2_{prepulse}$.

where the ion sound speed $c_s = \left(\frac{Z_{eff}k_BT_e}{m_i}\right)^{1/2}$, m_i is the ion mass, τ_L the laser pulse duration, and Z_{eff} is the ionisation state of the plasma. The temperature of the plasma described here as k_BT_e is dependent upon the wavelength and intensity of the laser.

For an exponential decay in plasma density described by (2.10) for a distance z from the original target surface, where $n = n_0$ before the interaction began.

$$n_e = n_0 e^{-z/L_s} \tag{2.10}$$

2.5.3 Laser Polarisation

A laser pulse can be s- or p- polarised. An s-polarised laser has the electric field perpendicular to the target surface normal. A p-polarised beam has a its electric field vector perpendicular to the direction of propagation and also parallel to the

target surface normal. Therefore at the reflecting point of the laser at the critical density surface, the electric field direction is parallel with the density gradient. The incoming beam in Figure 2.1 is a p-polarised beam. The electric field of an incoming s-polarised beam would out of the page.

2.6 Absorption mechanisms

In this discussion, interactions are separated into two regimes according to their plasma scalelength. Interactions with a scalelength that is greater than the laser wavelength λ_L are defined as a long scalelength. Short plasma scalelengths are described as $L_s \leqslant \lambda_L$, occurs for high contrast laser solid interactions.

2.6.1 Low density gradients

2.6.1.1 Resonance Absorption

For obliquely incident laser light, the laser reaches its turning point before the critical density surface. For an angle of incidence θ this occurs at $n_{crit} \cos^2 \theta$. The distance remaining between the turning point and the critical density parallel to the density gradient can be tunnelled by the electric field component in that direction [2], exciting a resonant wave at the critical density.

The optimal angle for maximum resonance absorption is given by $\theta = sin^{-1}(\omega_L L_s/c)$ where L_s is the density scalelength and ω_L is the laser frequency. This is described by the Denisov function that describes the angular dependence of resonance absorption for long density scalelengths [31].

2.6.1.2 Inverse Bremsstrahlung

Bremsstrahlung radiation is produced by an electron when it is decelerated in the Coulomb field of another charged particle. Its inverse process is the absorption of radiation in an interaction with another charged particle. A free electron in a plane laser field is oscillated by the Lorentz force, and once the laser field is turned off the electron goes back to its rest state. However, if an electron in an oscillating laser

field, interacts with the electrostatic field of an ion during an oscillation, and its kinetic energy is changed. The laser energy gained by the electron is thermalised, and the electron will not undergo a reverse process once the laser cycle has passed. This is also known as collisional absorption or free-free absorption as the electron remains free throughout [28].

This absorption mechanism is maximised when we have low temperature, high Z plasmas with long density scalelength [2]. When considering high intensity lasers ($> 10^{18}\mathrm{Wcm}^{-2}$) the distribution of electron velocities is no longer considered to be Maxwellian [2].

2.6.1.3 $\mathbf{j} \times \mathbf{B}$ Heating

First discussed by Kruer et al. in 1985, this heating mechanism arises from the ponderomotive force of the laser [32]. In addition to the quiver energy, electrons undergo a second source of motion along the laser propagation direction. The oscillation of the electrons due to this $\mathbf{j} \times \mathbf{B}$ heating is along the laser axis and at twice the frequency of the laser [33]. In this way, a fraction of the electrons can gain sufficient energy to penetrate into the overdense plasma. At high intensities the dominant mechanism for laser absorption is dependent on the magnitude of the $(\mathbf{v} \times \mathbf{B})$ term of the Lorentz force, compared to the component of the electric field of the laser normal to the surface of the target. Therefore an angle of incidence at or near target normal results in the $\mathbf{j} \times \mathbf{B}$ mechanism being dominant [34].

2.6.2 Steep density gradients

For short scalelength plasmas where $L_s < \lambda_L$, the density gradient is steep and a sharp boundary between vacuum and solid density is observed. In this regime, the vacuum heating mechanism and $\mathbf{j} \times \mathbf{B}$ heating are important.

2.6.2.1 Vacuum Heating

First highlighted by Brunel in 1987 [35], this arises due to very steep density gradients. If no density gradient is present electrons oscillate symmetrically about the

laser axis with the laser field. As with resonance absorption, the electric field of the laser lies perpendicular to the direction of propagation driving electrons across the critical density surface. Electrons propagated into the overdense region i.e. $n_e > n_{crit}$, no longer feel the full restoring force as the laser field is not present [35, 36]. The restoring force ensures that there is no net gain of energy by the plasma. However, without the restoring effect energy can be lost from the electrons into the plasma. The fraction of the energy absorbed corresponds to the energy of the re-entering electrons. This excursion of electrons into vacuum only happens to those near the vacuum-plasma boundary, where the density gradient is steep $L_s > \lambda_L$ [36]. Where this is the case, this mechanism dominates over resonance absorption [37]. For resonance absorption in longer scalelength interactions the laser electric field causes resonant excitation of an electron plasma wave at the apex of the laser light, no such resonance can exist here. Vacuum heating is the non-resonant coupling of laser light to electron plasma wave, or is resonant absorption in the limit of a step function in density.

2.6.2.2 Profile Steepening

The ponderomotive force as given in (2.7) results in a net force being applied to electrons in the direction of ∇E^2. The laser pulse has a spatial profile, and as such, the effect of the ponderomotive force is greatest at the regions of high E, or on the laser axis. Ponderomotive pressure $f_p = \nabla(\gamma - 1)m_0c^2$ where $\gamma = 1 + p^2/m_0^2$ and p is the momentum of the electron in the direction of electron oscillation. The pressure exerted causes the density gradient to become steepened [33].

For high intensities, the radiation pressure from the incident laser pulse can push against the thermal pressure of the expanding front surface plasma given by $n_e k_B T_e$ [38]. This causes the density profile to steepen at the critical density.

2.7 Fast electron temperature

Several fast electron temperature scalings exist for different laser-solid interaction regimes. The fast electron temperature is typically calculated from knowledge of the lasers wavelength and intensity, which defines the conditions of the interaction [39].

The characteristic electron temperature in a regime where resonance absorption is assumed to be the dominant process is $14(I_{16}\lambda^2_{\mu m})^{1/3}T^{1/3}_{fast}$ [40]. This temperature estimation is valid for intensities $< 10^{17}Wcm^{-2}$, and has an optimum angle of incidence described in Section 2.6.1.1. Resonance absorption is present in all scalelength plasmas [31] but other effects become more prominent in short scalelengths.

For $I\lambda^2 < 10^{19}\mathrm{Wcm}^{-2}$, the experimentally inferred Beg scaling [41] gives $T_{fast} = 215(I_{18}\lambda^2_{\mu\mathrm{m}})^{\frac{1}{3}}$, where I_{18} is the laser intensity in units of $10^{18}Wcm^{-2}$, and the laser wavelength is in μm. Haines et al. [42] developed an analytical model that fits well with experiments [43, 44]. The Haines model is valid for laser intensities up to $5 \times 10^{18}Wcm^{-2}$ takes the form $T_{fast} \propto (I\lambda^2)^{1/3}$ [42].

A temperature scaling for use with steep density gradients and intensities $< 10^{17}Wcm^{-2}$ in the regime of vacuum heating, was also derived from PIC simulation to be $T_{fast} = 7(I_{16}\lambda^2_{\mu m})^{1/3}$ [45] . In each of these scaling laws, the electron temperature scales with $T_{fast} \propto (I\lambda^2)^{1/3}$.

The temperature scaling resulting from the $\mathbf{j} \times \mathbf{B}$ heating mechanism is given by [33]

$$T_{fast} = 511[(1 + 0.73I_{18}\lambda^2_{\mu m})^{1/2} - 1]\ [keV] \tag{2.11}$$

This temperature scaling is applicable to short scalelength experiments at relativistic intensities $> 10^{18}Wcm^{-2}$ [46].

For interactions at normal incidence where vacuum heating is the dominant absorption mechanism, $T_{fast} = 3.7(I_{16}\lambda^2)$ [35]. Both the Haines and Wilks scalings are such that $T_{fast} \propto (I\lambda^2_L)^{1/2}$

Certain authors have seen that fast electron temperature is best estimated by

applying a factor of 0.6 to the ponderomotive temperature [47, 48], which in this work is seen to agree with experimental data.

All experiments presented in this thesis are shot at an oblique incidence angle of $\theta = 40^\circ$ to target normal for optimum absorption characteristics and partly due to experimental reasons. The Beg and resonance scalings for fast electron temperatures apply for oblique angles of incidence, but for intensities of approximately $10^{17}\mathrm{Wcm}^{-2}$ to $10^{19}\mathrm{Wcm}^{-2}$. The Wilks or ponderomotive scalings is relevant to the high intensity regimes of $> 10^{18}\mathrm{Wcm}^{-2}$, but for normal incidence. In similar experiments [39, 48–50] the general consensus is that the use of the ponderomotive scaling (2.11) is most representative of the fast electron temperature.

2.8 Fast electron transport

The transport of electrons within the target is responsible for the generation of magnetic fields, and the cause of target heating. The forward propagating fast electrons are not collisional, but the less energetic than return current electrons that are highly collisional, and resistively heat the target. The current density of the two beams is approximately balanced $\mathbf{j_f} + \mathbf{j_r} \approx 0$ [51].

The fast electron current exceeds the fundamental limit on the amount current that can flow in the target, however by drawing a counter propagating return current this limit can be exceeded.

2.8.1 Alfvén Limit

The Alfvén limit I_a describes the maximum current that may be carried in a vacuum, before the self generated magnetic field inhibits the beams propagation [3, 52].

$$I_a = 17\beta\gamma\mathrm{kA} \tag{2.12}$$

Where the multiplication factor in (2.12) is $m_e c^3/e = 17\mathrm{kA}$, $\beta = \nu/c$ and $\gamma = (1-\beta^2)^{-1/2}$. For currents above this limit the magnetic field that is generated is large enough to reduce the Larmor radius of the electrons to less than the beam radius

(described later), and electrons no longer propagate in the beam direction. Within ultra-intense laser plasma interactions, large mega-ampere currents are commonplace, and the beam can only propagate by the generation of a counter-propagating return current. The return current balances the fast electron current spatially and temporally, such that the net current density is approximately zero at any point. Small deviations from this result in the self-generation of magnetic field.

2.8.2 Ohmic heating

The beam of electrons generated in the laser-solid interaction causes the propagation of a counter propagating return current beam such that $\mathbf{j_f} + \mathbf{j_r} \approx 0$. Assuming this balancing effect, the electric field can be given by,

$$\mathbf{E} = -\eta \mathbf{j_f} \tag{2.13}$$

Where $\mathbf{E}$ is the electric field in the target and η is the resistivity of the target material. The Spitzer regime where $\eta \propto ZT_e^{-3/2}$ assumes that the resistivity is due only to electron-ion collisions. The heating power of the return current beam can be given by equation 2.14, and by substitution of equation 2.13 [53].

$$P = |\mathbf{j_f}||\mathbf{E}| = -\eta \mathbf{j_f}^2 = \Big(\frac{3}{2}\Big) n_e e \Big(\frac{\partial T_{cold}}{\partial t}\Big) \tag{2.14}$$

Where T_{cold} is the temperature of the background plasma, and t is time. The heating power of the return current beam $P \propto \mathbf{j_f}^2$.

2.8.3 Magnetic field generation

The generation of a magnetic field during the propagation of a fast electron beam can be described by the combination of the Maxwell-Faraday equation and Ohms law (2.13)[54, 55].

$$\frac{\partial \mathbf{B}}{\partial t} = -\nabla \times \mathbf{E} \tag{2.15}$$

By substitution of the electric field in equation 2.13 this can be written as,

$$\frac{\partial \mathbf{B}}{\partial t} = \eta \nabla \times \mathbf{j_f} + (\nabla \eta) \times \mathbf{j_f} \tag{2.16}$$

The resistively generated magnetic field has two components (2.16), the first pushes the electrons towards areas of low resistivity and the second that pushes electrons towards areas of high resistivity. Robinson et al. showed by simulation that by structuring the target, introducing resistivity gradients, beam collimation can be greatly improved [54]. This was experimentally verified by Kar et al. by using structured targets to produce strong resistivity gradients [56].

Collimation of the magnetic field is determined by the ratio of the radius of the fast electron beam R and the Larmor radius r_g [53]. When $R/r_g > \theta_{1/2}^2$ where the magnetic field is capable of bending the fast electron trajectory by an angle $\theta_{1/2}$ over a distance $R/\theta_{1/2}$. The beam approximately doubles in size over this distance. The collimation condition is $\Gamma > 1$, where Γ is given below for cases where there has been substantial resistive heating, i.e. the temperature of the background plasma is much less than the initial target temperature $T_{cold} >> T_{init}$ [53]. A simple expression for this, using the same model, is shown in terms of the magnetic field and beam energy [21].

$$1 - cos\theta_{1/2} = 0.06\frac{R_{\mu m}B_{MG}}{[E_{511}(2 + E_{511})]^{1/2}} \tag{2.17}$$

Where $R_{\mu m}$ is the beam radius in micrometres, the magnetic field B_{MG} is expressed in units of MG, E_{511} is the fast electron energy in units of 511keV, and $\theta_{1/2}$ is the fast electron divergence half angle. This shows that for a 1MeV beam injected with an angle of 85° to be collimated a 4MG magnetic field is needed [21].

2.9 Spectroscopy

2.9.1 Introduction

The combination of short lifetime and extreme conditions makes the diagnosis of intense laser plasma experiments challenging and interesting. One option to produce reliable information on the properties of a short lived plasma such as this is the capture and analysis of the radiation field that is emitted from it. Spectroscopy is a powerful tool for the diagnosis of this field. It provides a way to indirectly measure

properties such as the plasma temperature or density, or for more detailed analysis of the populations of individual ion charge states. Furthermore, it can be used on a variety of subjects, from the short lived very intense emission of the laboratory plasma to those of remote astrophysical plasmas.

The radiation that is emitted from a plasma contains information on a number of different atomic and hydrodynamic processes. The radiation is like a fingerprint of the plasma, providing information that is unique for each set of conditions. There are many factors which will influence measurements and good understanding of the experiment and the diagnostic is essential.

Some of the key influencing factors on emitted radiation are the hydrodynamic state of the plasma, its size, and its composition. The composition of the plasma can be controlled by experimental design, and to some extent the use of precision targetry.

The emission of radiation from the plasma is a result of the excitation or de-excitation of electrons. In these short timescale experiments the ions are assumed to be fixed in their position, but the electrons can exist in free or bound states. The interaction between these states with the ions gives rise to emission. An electron transition between two bound energy levels results in spectral line emission, this is a bound-bound transition. The wavelength of the emitted radiation is given by the difference in energy between the two states. An electron that is free may recombine into a bound state resulting in the emission of photons. Finally there are transitions between free electron energy levels. The electron remains free throughout the transition, this leads to a continuous background emission, also known as free-free or Bremsstrahlung emission. Although this is a background emission, it still contains information about the plasma [39].

The analysis and interpretation of spectroscopic data containing all of these transitions can be very complicated. The process by which free and bound states can interact for each possible ionisation state and atomic configuration of the ions in the plasma generates many possibilities. The use of detailed theoretical models is

a key part of this analysis and is used to extract the information held in an emission spectrum.

2.9.2 Ionisation kinetics

The ionisation balance in a plasma is determined by the relative rates of all the atomic processes that occur in the plasma. The distribution of ions within the plasma over all bound states determines the overall ionisation state. For a given energy level in a plasma, a rate equation shows the rate of change of its population with respect to time, and takes into account all of the populating and depopulating processes in the plasma. Processes that contribute are broadly split into two categories of collisional or radiative processes.

2.9.3 Collisional processes in plasma

Collisional processes can be further split into elastic and inelastic collisions. The inelastic collision is one in which the overall energy of the system is conserved but energy may be transferred from one form to another. For an electron colliding with an ion, the electron may impart some energy into the ion causing the promotion of a bound electron into an excited state.

An elastic collision between two objects is one in which the kinetic energy is conserved and can occur between electrons, ions or a combination. Elastic collisions result in the exchange of kinetic energy between particles. The velocity distribution function (VDF) is given by the Maxwell-Boltzmann equation,

$$f(v)d\nu = 4\pi v^2 dv\Big(\frac{m}{2\pi \mathrm{k}T}\Big)^{3/2}\exp\Big(-\frac{mv^2}{2kT}\Big) \tag{2.18}$$

where $f(v)$ represents the probability distribution function and T is the temperature, and m is the mass of the particle. This distribution describes just a single particle population, and the plasma consists of two very distinct populations, that of the electron and the ions with separate distributions. Due to their vastly different masses, the electron-ion equilibration time is much longer than for ion-ion

or electron-electron collisions. Therefore the electrons and ions will equilibrate as individual populations much faster than the whole plasma. With regards to laser produced plasmas where the lifetimes can be short (ps) a temperature for each of the populations is usually necessary.

The main collisonal processes that exist in the plasma are each considered in turn. In the following list, z is the degree of ionisation, g denotes the ground state of the ion and α and β represent two states in the plasma.

(a) Collisional ionisation. $(n_\alpha^z + e \rightarrow \mathrm{n}_g^{z+1} + e + e)$. In this process the impact of an electron into an ion causing an electron to be ionised to continuum. This is often the dominant ionisation mechanism in laser produced plasma.

(b) Collisional excitation and deexcitation $(n_\alpha^z + e \rightarrow \mathrm{n}_\beta^z + e)$. In this process the impact of a free electron causes the excitation of a bound electron into a higher energy state. Its inverse process $(\mathrm{n}_\beta^z + e \rightarrow \mathrm{n}_\alpha^z + e)$ is the de-excitation of a bound electron due to the free electron. Electron rates are normally dominant as the ions have a much greater mass and cannot move as quickly as electrons.

(c) Three body recombination $(\mathrm{n}_g^{z+1} + e + e \rightarrow \mathrm{n}_\beta^z + e)$ In this process, two free electrons interact in the sphere of an ion, resulting in the recombination of one electron. The other electron carries away the extra energy. It is the inverse process to electron impact ionisation, and the rate scales as n_e^2 so this is particularly prevalent in high density plasmas.

(d) Dielectronic recombination $(n_g^{z+1} + e \rightarrow \mathrm{n}_{\alpha,\alpha'}^{z-1} \rightarrow \mathrm{n}_\beta^{z-1} + h\nu)$ In this process a free electron is captured by an ion, and the additional energy is absorbed by a bound electron which is excited into a higher state, resulting in a double excited ion. The radiative recombination of an electron back into the ground state completes the process.

The rates of all of these processes scale with the density n_e, with the exception of three body recombination which scales with n_e^2.

2.9.4 Radiative processes in plasma

Radiative processes have a great effect on the ionisation state of the plasma. The key radiative processes are as follows, where the photon energy is denoted by $E_{h\nu}$.

(a) Photoexcitation ($n_\alpha^z + h\nu \rightarrow \mathrm{n}_\beta^z$). This process is the direct excitation of a bound electron by absorption of a photon with energy $E_{h\nu} = E_\beta - E_\alpha$

(b) Photo de-excitation - Stimulated emission ($\mathrm{n}_\beta^z + h\nu \rightarrow \mathrm{n}_\alpha^z + h\nu + h\nu$). A bound electron interacts with a photon causing it to decay into a lower energy level, emitting an additional photon.

(c) Photo de-excitation - Spontaneous emission ($n_\beta^z \rightarrow \mathrm{n}_\alpha^z + h\nu$) The probability of this spontaneous process is determined by the Einstein coefficient, $A_{\beta\alpha}$ where the subscript represents the transition from an upper state (β) to a lower state (α).

(d) Photoionisation ($n_\alpha^z + h\nu \rightarrow \mathrm{n}_g^{z+1} + e$) A photon with an energy greater than the ionisation energy of the bound electron causing it to be ejected into continuum. The rate at which this occurs depends on the photoionisation cross section, and the flux of incoming photons of appropriate energy.

(e) Photo-recombination - Stimulated radiative recombination ($n_g^{z+1} + h\nu + e \rightarrow \mathrm{n}_\alpha^z + h\nu + h\nu$). In this process, an electron is scattered from an ion in a radiation field, and the stabilising transition is stimulated by the absorption of a photon [57].

(f) Photo-recombination - Spontaneous radiative recombination $n_g^{z+1} + e \rightarrow \mathrm{n}_i^z + h\nu$). This process can be combined with the stimulated radiative recombination rate (e) to give a total radiative recombination rate.

For the optically thin plasma, the rates of (a), (b), (d) and (e) are all zero, leaving only spontaneous radiative recombination and spontaneous emission.

To produce an estimate of the population of all bound states in the plasma, each of the allowed collisional and radiative rate equations have to be included and rate equations produced for each. A quantum mechanical description of every bound state requires knowledge of its energy, degeneracy and the oscillator strength of each of the possible transitions. Calculations of this kind require such a tremendous amount of data that simplifications must be made to make it feasible.

2.9.5 Local Thermodynamic Equilibrium (LTE)

The use of an LTE model of the plasma is used primarily to simplify the solution of the rate equations, but still maintain a route to solution that allows prediction of the population distribution.

For a plasma to be in complete thermal equilibrium, there must be equilibrium between all plasma elements, i.e. ions, electrons and photons. In the laboratory, the size of the plasma is such that the particle populations may be in equilibrium with one another, but the photons are not.

For a system of atoms under the assumption of LTE at temperature T, the population of the excited levels is given by the Boltzmann equation,

$$\frac{n_\beta}{n_\alpha} = \frac{g_\alpha}{g_\beta} exp^{-\frac{E_\beta - E_\alpha}{kT}} \tag{2.19}$$

where g_α is the statistical weight of the state α (similarly for β), and $E_\beta - E_\alpha$ is the difference in energy between the two quantum levels.

The temperatures in the Planck and Maxwell equations are equal if the plasma is optically thick for all photon energies, such that a detailed balance can be achieved between photons and particles. For every photon emitted, one of the same wavelength must be absorbed, and the same for the excitation of electrons between two energy levels. However, for a laboratory plasma there is no equilibration between the photons and particles. For laser solid interactions, LTE can only be assumed when the contributions of photons is negligible.

Consequently, the first of the conditions for a system to be considered as being in LTE is that collisional processes must dominate radiative processes. If radiative processes must be minimal, this further implies, that the rate of spontaneous emission must be lower than the probability of de-excitation by collisions. Otherwise, the principle of detailed balance must apply to all processes, and the collisional processes must be balanced exactly by their inverse. The requirement of collisions to be balanced means that the three body recombination and electron impact ionisation rates have to be come nearly equal [58]. As three body recombination is an effect that is only prevalent at high densities, a consequence is that LTE tends to apply at high densities.

In order to prevent atomic processes deviating from LTE, the rate at which the collisional processes occur must be faster than the local changes in temperature and density gradients in the plasma. This results in another condition, that the rate of change of equilibrium distributions, i.e. temperature and density gradients must be low in comparison to the rates of the collisional processes so that locally, the plasma remains in equilibrium. Therefore as implied by the name *local* thermal equilibrium, it is the local temperatures and densities that are used to calculate the population distribution.

In summary, the conditions for LTE are that the plasma must be dominated by collisions, that all atomic processes are in detailed balance and that collisions are sufficiently rapid that the population distribution is adjusted immediately to any change in plasma conditions. Under LTE, the Saha equation and the Boltzmann equation can be used to specify the populations of the electron quantum states for a plasma, provided the electron temperature and density are given by the Saha equation [58]. The assumption of LTE is applied to some of the spectral modelling used in this thesis, except where the contribution of radiation is expected to be high.

2.9.6 The collisional radiative model

In the cases where the LTE assumption cannot be applied another model is used. One such model is called the coronal equilibrium (CE) model, which takes into account plasmas that are optically thin and at low density. This model is used when considering astrophysical plasmas such as the corona of the sun, or in laboratory devices such as tokamaks where low density plasma is produced in large volumes. In this approximation densities of electrons and ions are low and therefore the excitation rates are also low, and the spontaneous decay rate is such that an electron in an excited state will decay by spontaneous emission before another excitation event is encountered. As the plasma is also optically thin, the rates of photoionisation and photoexcitation are low as is the rate of three body recombination [58]. The dominant processes in plasmas under this regime are radiative and dielectronic recombinations. The CE model is very useful for the applications described but is not appropriate for the high density plasmas in laser solid interactions.

For such cases where LTE and CE cannot be applied, the collisional radiative (CR) model is used. In the CR model any process initiated by interaction with a photon is ignored. In steady state, the rates of population and depopulation of an energy level are equal. By disregarding photoionisation, photoexcitation and their inverse processes, we are left with spontaneous decay, electron impact excitation and deexcitation, three body recombination, radiative and dielectric recombination and electron impact ionisation.

For an isolated atom, the number of possible energy levels can be infinite. However the presence of neighbouring atoms and ions as in a plasma limits this number. This is particularly true in a high density plasma where there is continuum lowering, which causes a series of lines to be truncated as their bound states move to the continuum.

The energy difference in between energy levels decreases as principal quantum number rises. To reduce the number of states further still, we can say that levels at high energy their difference in energy is small enough such that the radiative decay

rates can be ignored and the rate of electron impact are higher. With no radiation to take care of, the model in this region is completely collisional in nature and can be solved using the LTE approximation. Single occupancy of high level states is typical and these be treated as hydrogenic.

The remainder of the energy levels at lower principal quantum numbers can be dealt with by detailed configuration accounting (DCA) or by detailed term accounting (DTA). In DCA, the electronic configuration is taken into account and provides detail to the subshell level. As the name suggests in DTA the term which takes into account the multiplicity and spin of the electron. This is spectroscopically the most accurate description, however it is computationally expensive and for $n > 3$, many thousands of levels need to be computed. If interest is only in a select few states, it is possible to group other levels together for computational savings whilst preserving the detail for transitions that are of interest. For atoms with high atomic number and many principal quantum shells, the average atom model may be used, where only a single rate equation using an average number of electrons for each state is used. To summarise, an overview of the detail provided by each of average atom, DCA and DTA is provided in Figure 2.2 [59].

In the following Section 2.10.2, a CR model is used to predict the flux of a specific spectral line emitted from a plasma at a variety of different temperatures. This information is pivotal to parts of the work presented in Chapter 4 and will be referred back to at several points in this thesis.

2.10 PrismSPECT

2.10.1 Brief overview

PrismSPECT is a time dependent collisional radiative model that is capable of both LTE and non-LTE calculations [60]. It contains calculations for electron impact ionisation, recombination, excitation, deexcitation, radiative recombination, spontaneous decay, dielectronic recombination, autoionisation, electron capture, pho-

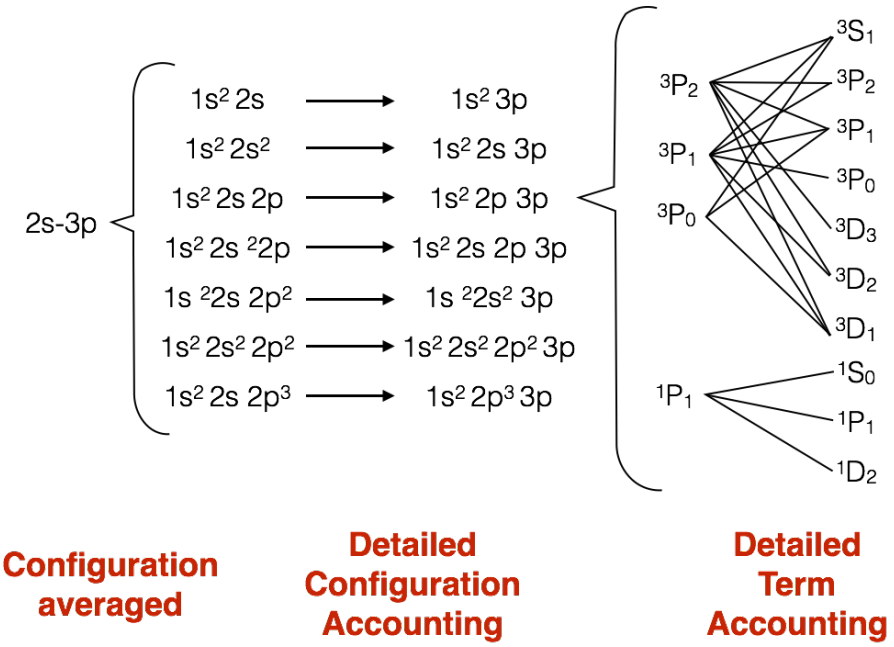

Figure 2.2: Comparison of detail afforded by average atom, detailed configuration accounting and detailed term accounting in the modelling ot atomic states [59]. Standard LS atomic configuration notation is used.

toionisation, photoexcitation and stimulated recombination and deexcitation [61]. There are several relevant examples where PrismSPECT has been used, including its use in a study of target heating by the emission of K-α spectral line [62–64].

2.10.2 Effect of material temperature on emission

Accurate knowledge of the emitted photon flux for a single spectral line with changing temperature and density is critical for the experimental data analysis that follows in this thesis. As we have already seen in previous sections, the balancing of the rates of ionisation and recombination, determines the emitted photon flux for a given spectral line. This is sensitive to material temperature. The collisional radiative spectral analysis code PrismSPECT [60] solves the non-LTE rate equations to calculate the number of photons emitted from materials over a given temperature range. Figure 2.3(a) shows the steady state calculation of the emission helium beta (He-β) line for aluminium with temperature.

Figure 2.3(a) shows that the emission of the Al He-β spectral line is peaked at

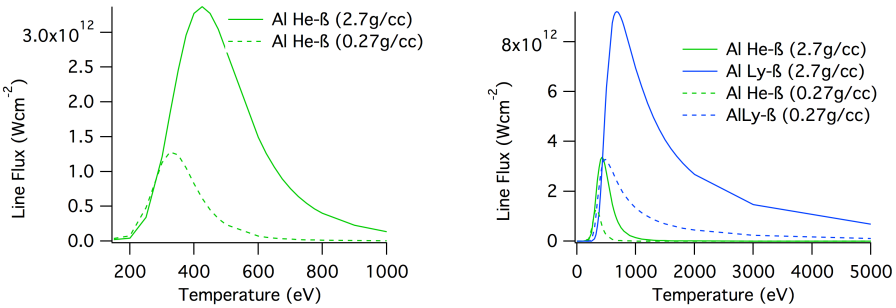

Figure 2.3: (a)Effect of plasma temperature and density on emission flux of aluminium Helium-β at solid density and at one tenth of solid for comparison. Emitted lineflux in the cases of both lines is strongly dominated by emission from the solid density material. (b) Comparison of the He-β and Lyman-β line emission with temperature.

approximately 400eV for solid density. Also plotted in Figure 2.3(b) is line flux of the Lyman beta (Ly-β) line, showing peak emission at the higher temperature of around 700eV. For the He-β line at temperatures greater than 300eV, the emission from solid density material is dominant over lower density material as the rate of recombination scales as n_e^2 and the rate of ionisation scales as n_e. Consequently, as density rises, the rate of recombination becomes greater than the ionisation rate, implying that measurements of this spectral line are suited to the diagnosis of high density experiments. Emission is assumed to be dominated by the emission from solid density material within the target. Material outside of the working temperature range of 300 - 700eV, or at lower densities will show significantly less intense or no photon emission altogether.

2.10.3 Brief overview of time dependent and steady state flux calculation

PrismSPECT can be set to solve the time dependent or steady state rate equations, and these are compared here. Two time dependent gaussian temperature profiles peaking at 400eV and 1keV respectively, each with a FWHM of 825fs were input into the code for solid density aluminium in both cases. The results show the intensity of the emission of the He-β_1 and He-β_2 spectral lines. The results for the 400eV

simulation are shown in Figure 2.4.

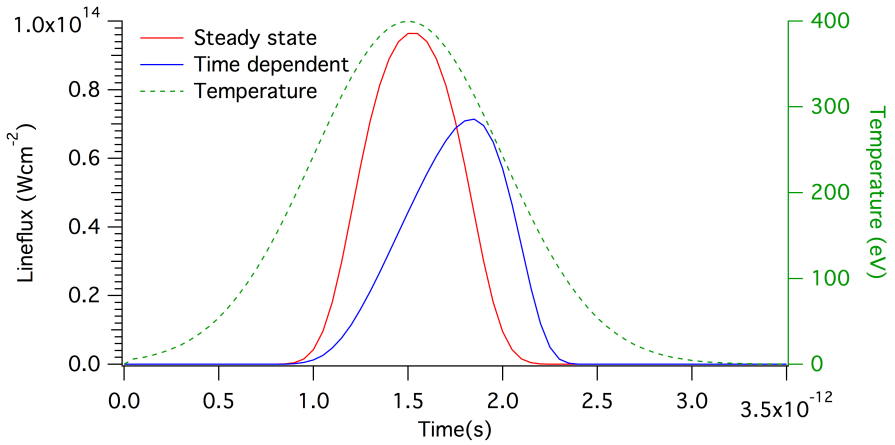

Figure 2.4: Time dependence of emission calculated by PrismSPECT for an input gaussian profile with a FWHM of 825fs, peaking at 1.5ps and at a temperature of 400eV. The time dependent and steady state rate equations are solved as indicated. The input trace (green dashed) is set to the right axis of the plot.

Figure 2.4 shows the time dependent and steady state solutions in blue and red respectively. The input is also plotted for comparison. The steady state simulation is symmetrical about the time at which the input trace peaks at 1.5ps. The peak emission from the time dependent solution is shifted by 0.4ps. The results in Figure 2.4 for the 400eV simulations do not exceed the upper emission threshold and show a smooth increase in lineflux to a peak that then drops away. The peak of the emission is also seen to be approximately 20% higher for the steady state simulation. The ratio of the integrated intensities is $I_{ss}/I_{td} = 1.24$, where I_{ss} and I_{td} are the steady state and time dependent integrated intensities respectively. Figure 2.5 shows the results from the 1keV simulation.

Figure 2.5 shows that when the temperature exceeds the upper threshold for emission at approximately 600eV, or drops below around 200eV the lineflux drops. This produces double peaked profile for the steady state and time dependent cases of the 1keV peaked input profile shown by the green dashed trace.

The peak of the emission profile in the time dependent cases is shifted by approximately 0.4ps later in time compared to the steady state case due to the small

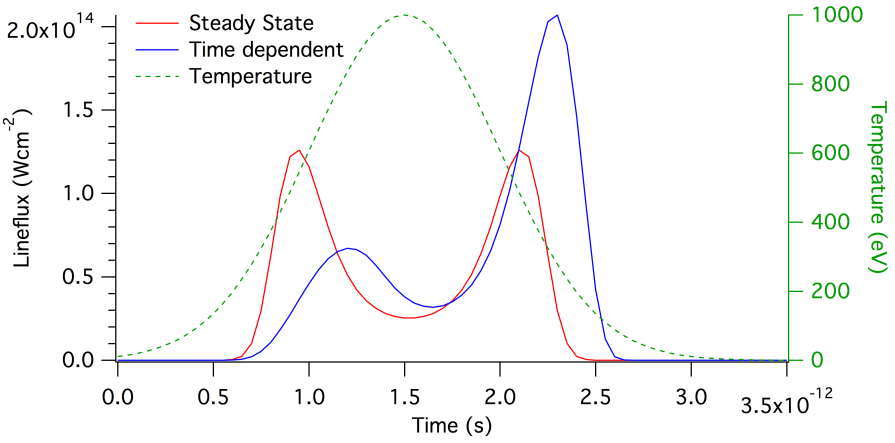

Figure 2.5: Time dependence of emission calculated by PrismSPECT for an input gaussian profile with a FWHM of 825fs, peaking at 1.5ps and at a temperature of 1keV. The time dependent and steady state rate equations are solved as indicated. The input trace (green dashed) is set to the right axis of the plot.

but finite time taken for ionisation, and the subsequent recombination causing the emission of a photon. For the steady state case the emission is symmetrical in time around 1.55ps, indicating a very small delay (50fs) after the peak of the input temperature profile. However, the ratio of the integrated intensities is $I_{ss}/I_{td} = 0.80$. The peak intensities reached by the two peaks in the case of steady state and time dependent is significantly different, with the second peak of the time dependent solution at approximately 2.6ps reaching almost double the peak intensity of the steady state case.

This suggests that there may be some time dependent effects on the emission of the He-β emission line.

2.11 Zephyros: a brief overview

Zephyros is a 3D hybrid-PIC code that takes in user defined laser parameters and injects fast electrons into the target. In this case, the laser is set to be incident on the centre of the target surface. Let z be defined as the depth into the target, and x-y define a plane perpendicular to the target surface normal. The intensity of the laser as a function of radius (transverse) is approximated as a gaussian profile given

by,

$$I(r)\alpha^{\frac{-r^2}{2r_l{}^2}} \tag{2.20}$$

where r_L is the focal spot radius fixed by experimental measurement of the laser focal spot. The number of fast electrons is given by N_{fasts} given by,

$$N_{fasts} = \frac{\eta_{abs} I(r) \Delta \mathrm{y} \Delta \mathrm{x} \Delta \mathrm{t}}{\bar{\varepsilon}_{fast}} \tag{2.21}$$

where η_{abs} is the fraction of the laser absorbed, $I(r)$ is the laser intensity as a function of radius (transverse) and $\bar{\varepsilon}_{fast}$ is the average fast electron energy. Δy and Δx and Δt represent the cell size and timestep. The energy distribution of fast electron energy is assumed to be exponential and given by the form $f(E) \propto \mathrm{e}^{-E/k_b T_f}$ for all simulations. The temperature of the fast electrons is based on the ponderomotive scaling, set up as a default within the code. The angular distribution of the fast electrons has been set to be a uniform distribution over a given solid angle, the half angle specified by the user.

Zephyros creates fast electrons in the simulation by promotion from the cold background. Electrons with energy exceeding 11keV are considered as part of the fast electron population, and those below this threshold are part of the colder background population.

The fast electron population is modelled within the particle-in-cell element of the Zephyros code, and the large numbers of fast electrons are represented within macroparticles which represent many 'real' fast electrons. The use of macroparticles lightens the computational load of a simulation. In Zephyros, the number of particles represented by each macroparticle is determined by the intensity of the laser field at the point which it is injected. All macroparticles are injected at $z = 0$, and have a population given by,

$$N_e = \frac{\eta I(r) \Delta t \Delta y \Delta z}{e T_f n_p} \tag{2.22}$$

where n_p is a constant and represents the number of macroparticles injected per intrinsic timestep of the code Δt. This is the time that it takes to traverse the minimum cell dimension at c, $\Delta \mathrm{t} = \Delta \mathrm{x}/c$, where Δx is whichever is the smallest

out of Δx, Δy and Δz. The output timestep is specified by the user, with a total simulation time of 3ps. The resistivity of the target is calculated from a reduced Lee-More model [65], and the atomic model [66] that is used for the effective atomic number Z of the background ions is a fit to the Thomas-Fermi model used by Davies [66–68]. The reduced Lee-More model makes use of this model to generate the resistivity curve [67]. The ionisation state of the ions affects not only the resistivity curves but the rate of angular scattering from the background ions and the level of drag on the fast electrons due to collisions with the background electrons [67].

2.12 THOR

THOR is a Monte-Carlo Fokker-Planck code that has been used to model the target temperature resulting from the interaction of an ultra-intense laser with a solid density target. The code is part of the AWE suite of codes under development to provide a complete modelling capability for intense laser plasma interactions [69]. The THOR model for fast electron transport uses a hybrid approximation similar to that of Davies et al. [66, 68]. This code considers electrons that have energies greater than 10keV as part of the Monte Carlo portion of the simulation that are subject to collisional drag, scattering processes and self-generated electromagnetic fields [69]. The electric fields present in the simulations are derived from a simplified Ohm's law and the magnetic fields by Maxwell's equations and $j_{rc} = -j_{fast}$. In the THOR model, the electron energy distribution is given by a Maxwell-Juttner. This generalisation of the commonly used Maxwell$-$Boltzmann distribution for relativistic speeds is applicable to this system as the laser intensity produces MA currents of relativistic electrons which affect the target heating. All simulations using the THOR model in this thesis are completed by M. Ramsay at AWE.

2.13 Los Alamos Suite of Atomic Codes

The Los Alamos National Laboratory supports a suite of online atomic codes for performing atomic structure calculations [70, 71]. The complete suite comprises of 5 codes namely Cowan Atomic Structure code (CATS), Relativistic Atomic Structure code (RATS), Another Collisional Excitation model (ACE), an ionisation model GIPPER and ATOMIC [71]. CATS is an atomic structure code that uses the Hartree-Fock method to generate wavefunctions, oscillator strengths and energies in the semi-relativistic regime. The online user interface for the CATS, ACE and GIPPER codes were used in this thesis and are referred as the Cowan codes for convenience [70]. They are used in Chapter 5 for the calculation of atomic state lifetimes and the ionisation cross sections for collisional and photoionisation. RATS is the relativistic equivalent of CATS [72] and was used in Chapter 5 fully relativistic calculations of the work done with CATS [73].

2.14 Convention

Throughout this thesis, the convention used for all simulations is to use z for the laser direction, for a p-polarised beam x would be the direction of polarisation and y is the vertical axis.

Chapter 3

Instrumentation

3.1 Overview

The work presented in this thesis is the result of the interaction of an ultra-intense laser pulse with a solid density, cold target. The physics that arises as a result of these interactions is rich, and x-ray spectroscopy provides a powerful tool with which to probe/observe these physical phenomena. Experimental work was conducted on the petawatt beamline of the Vulcan Laser facility at the STFC Rutherford Appleton Laboratory, and in the first part of this chapter (Section 3.2), the facility shall be described.

In the second part of this chapter, (Section 3.3 onward) the x-ray diagnostics pertaining to each of the following chapters shall be described. Aside from some supporting optical measurements all of the experimental data presented is captured by crystal spectrometers. The spectrometers themselves, and some of the fundamental concepts of x-ray spectroscopy in laser produced plasmas will be described. Some of the limitations imposed on these measurements by the diagnostic will also be described here, and referred to in later chapters.

3.2 Vulcan Laser facility

The Vulcan laser facility is a Nd:glass laser system situated at the Rutherford Appleton Laboratory in Oxfordshire. The Vulcan system in its entirety is an 8 beam system with 6 long pulse and two short pulse beams [74–77]. These beams oper-

ate in two separate target areas, namely target area west (TAW) and target area petawatt (TAP). As its name suggests, TAP runs experiments with the petawatt (PW) beamline and operates as a separate system with an optical parametric chirped pulse amplification (OPCPA) front end.

The original CPA laser system began operation in 1998 and was capable of producing laser pulses with a wavelength of $\lambda = 1054$nm, a duration of 0.7ps in a 5μm focal spot with intensities reaching 5×10^{19}Wcm^{-2} [75]. In 2004 the beamline into TAP was upgraded to have an OPCPA front end, increasing the pulse compression and energy available to produce pulses of the order of 500J in 500fs and peak intensity exceeding 1×10^{20}Wcm^{-2}. The CPA and OPCPA methodologies have been known since 1979 and 1989 respectively, and their detailed operation at Vulcan can be found in references [78] and [79]. A schematic of TAP is shown in Figure 3.1, with the individual beamlines marked for reference.

The Vulcan seed pulse is a nJ Ti:sapphire pulse of approximately 120fs duration that is amplified in three stages. Very briefly, the first stage of amplification is a Nd:silicate rod amplifier, after which it joins the main Vulcan short pulse beamline. During the second stage it passes through Nd:Phosphate rod amplifiers and disc amplifiers, and the third and final stage is a final disc amplifier. The wavefront of the amplified pulse is corrected by an adaptive optics (AO) system, which helps to improve the quality of the focussed spot and its compression. For more details of the exact generation and amplification of the PW pulse see references [74–77].

The amplified pulse that enters the target area is compressed under vacuum by two gold coated diffraction gratings (1480lines/mm). Each of these gratings is approximately 1m in diameter so that the energy contained in the pulse per unit area is less than the damage threshold of the grating surface. The final amplified and compressed laser pulse is delivered into the target chamber and focussed onto target with an f/3 off-axis parabola into a spot of approximately 5μm. This beamline is capable of delivering compressed sub-picosecond pulses with intensities greater than 10^{21}Wcm^{-2}.

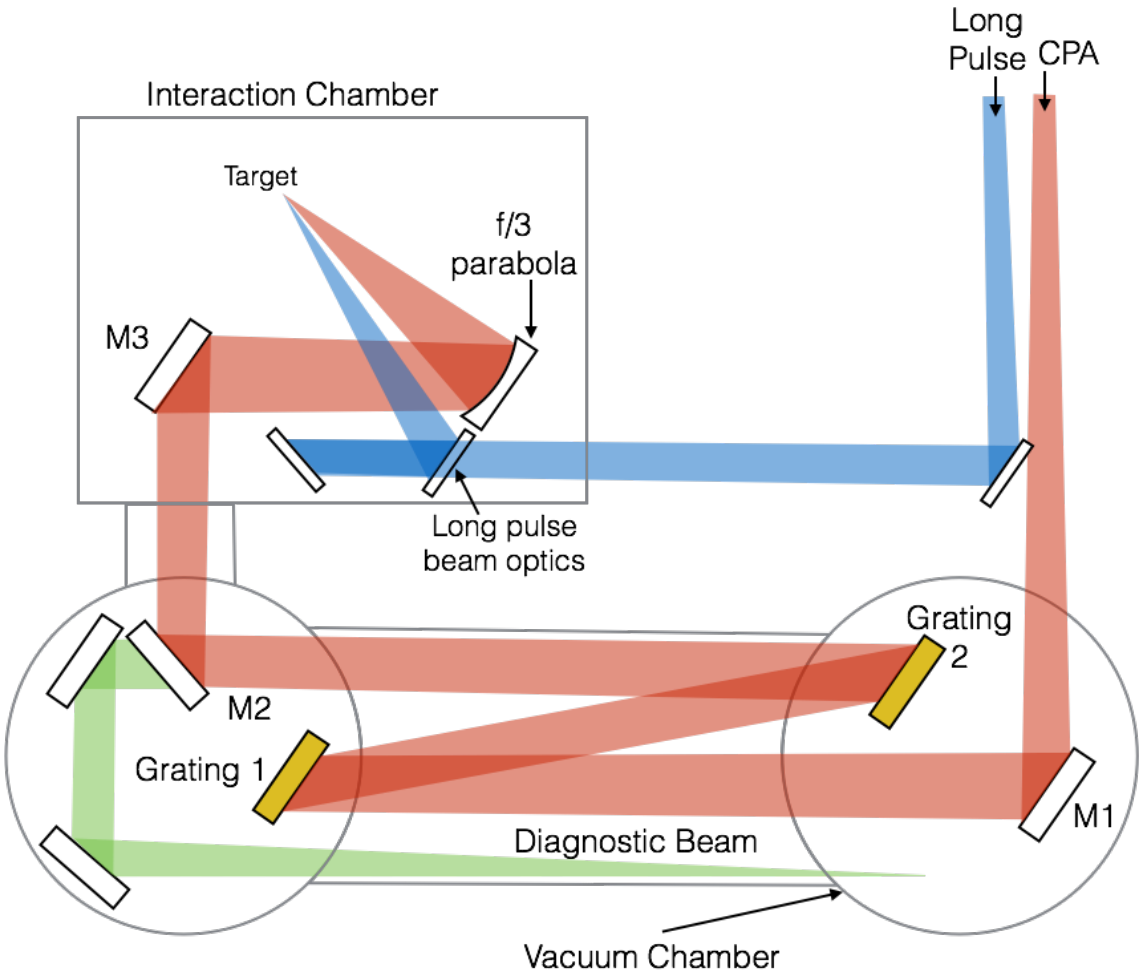

Figure 3.1: Layout of laser beams in TAP (not to scale). The chirped pulse amplification (CPA) picosecond high intensity pulse, initially enters the target area as a long duration expanding beam. It is reflected from mirror M1, and is compressed between gratings 1 and 2 into a short duration disc of laser light that is directed into the interaction chamber by M2 and M3. This is focussed onto the target by an f/3 off-axis parabola, and focussed intensities of 10^{20}Wcm^{-2} are produced. The long pulse beam enters the target area and is directed into the interaction chamber via a set of mirrors, and is focussed onto the target with an f/10 lens producing variable intensities of up to 10^{12}Wcm^{-2}. Also shown is the leakage from M2 in the forward direction which is used for beam diagnostics.

The Vulcan laser in TAP consists of two beams. The short pulse CPA beam as described, and a long pulse beam that is delivered by a separate beamline into the interaction chamber and focuses to the same point as the short pulse beam. This beam was used to provide laser energies of the order of 20J on ns timescales, with intensity of approximately $1 \times 10^{12}\text{Wcm}^{-2}$. This beam produces a front surface plasma on the front surface of the target or preheat it, and can be timed accurately against the CPA pulse such that front surface plasma effects can be studied.

3.2.1 Temporal Profile

The contrast of the laser pulse is defined as the ratio of the peak intensity, to the intensity of the light preceding it. The laser light present at the target surface before the main pulse peak is known as the prepulse. Plasma begins to form on the surface of an aluminium target for intensities exceeding approximately 10^{11}Wcm^{-2}. Arrival of significant levels of laser light at the target surface before the pulse peak will result in target heating, ablation of the target surface, and destruction of thin targets before the main interaction. It is therefore crucial that this prepulse be characterised and the temporal profile of the whole pulse known. The contrast of a laser system is commonly measured at times of 1ns and several picoseconds before the main pulse arrival. Nanosecond and picosecond contrasts of 10^{-8} and 10^{-6} respectively, have been observed on the TAP beamline [30, 80].

Amplified spontaneous emission (ASE) is a major contributor to the prepulse in systems with high gain such as Vulcan. The ASE is the luminescence from spontaneous emission in the gain medium of the amplifier, and is unavoidable. This can present significant power in the prepulse and introduce noise onto an otherwise high contrast pulse. The effects of ASE are seen in the temporal profile of the laser, which for the TAP pulse as used in experiments presented here is shown in Figure 3.2. Figure 3.2 shows that the contrast of the laser is approximately 5×10^{-8} at 100ps, and the contrast has been measured to be 10^{-10} at nanosecond [81]. This corresponds to a prepulse level of 10^{10}Wcm^{-2} at the target for 1ns before the pulse

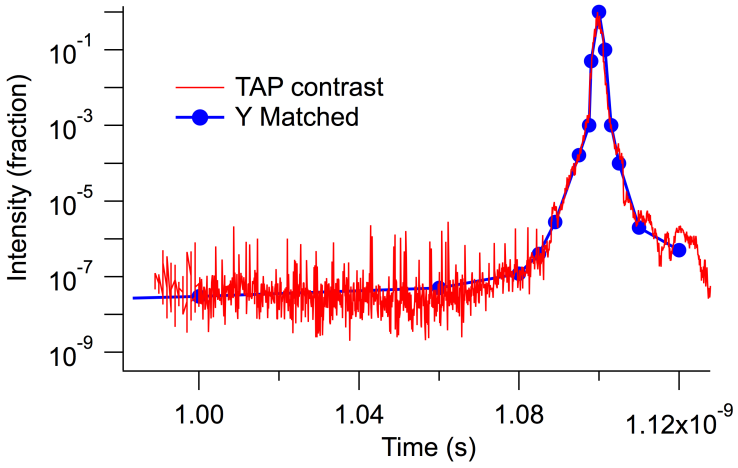

Figure 3.2: The temporal profile of the TAP short pulse laser, with normalised intensity.

arrives.

The temporal profile of the pulse as shown in Figure 3.2 with a peak intensity of 1×10^{20}Wcm^{-2} and $3 \times^{20}$ Wcm^{-2} used as the input for hydrodynamic simulation, to illustrate how the front surface of the target is effected by this prepulse. Due to the restriction of the model to non-relativistic pulses, the pulse has been modelled up until 100ps before the peak as the pulse (at 1.09ns on Figure 3.2) exceeds $\approx 10^{15}$Wcm^{-2} at this point. Figure 3.3 shows the results.

Figure 3.3 shows that for the 1×10^{21}Wcm^{-2}, the predicted scalelength is approximately 10μm. Owing to the fact that this is a 1-dimensional approximation, we must take into account that beyond time frames approaching 200ps the plasma has had time to expand laterally across the target surface, beyond the width of the laser spot and not all effects can be captured in one dimension.

3.2.2 Spatial Profile

To obtain the spatial intensity profile of the laser spot as it strikes the target, an image of the focal spot is recorded. The sheer intensity of the laser beam at full power prohibits direct measurement, and use of an equivalent plane monitor here is impractical. In this case, the focal spot is measured by operation in a low intensity

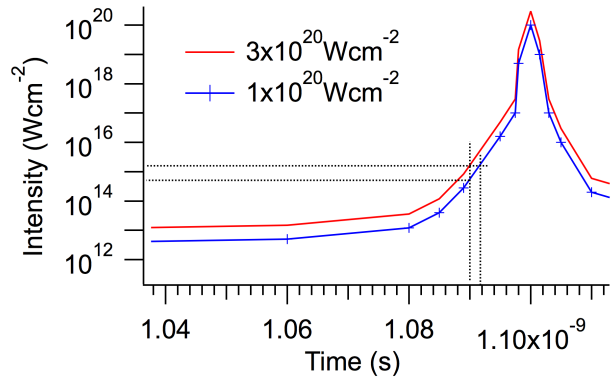

(a) Input profile for a peak intensity of $1 \times 10^{15}\mathrm{Wcm}^{-2}$ and $3 \times 10^{15}\mathrm{Wcm}^{-2}$

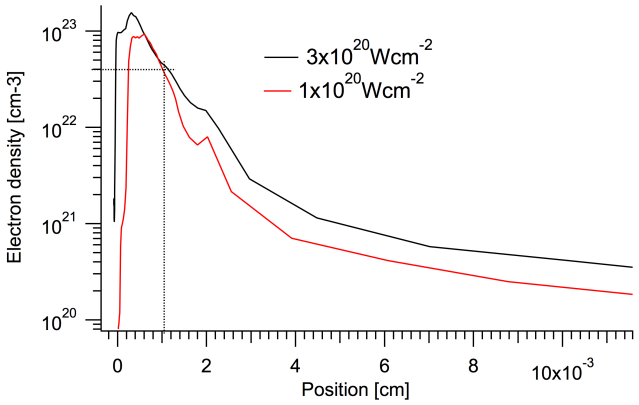

(b) Electron density profile

Figure 3.3: 1D hydrodynamic modelling of TAP pulse profile up to $5 \times 10^{15}\mathrm{Wcm}^{-2}$ at 1.09 ns before the pulse peak. Two peak input intensities of $1 \times 10^{20}\mathrm{Wcm}^{-2}$ and $3 \times 10^{20}\mathrm{Wcm}^{-2}$ were used to show the sensitivity of the predicted scalelength to peak intensity.

continuous wave (CW) mode which follows the same optical path as the main CPA laser beam, is imaged with an objective onto a CCD. This is done to mimic the introduction of perturbations from optics or other components experienced before reaching the target. Shown in Figure 3.4, is an image of the focal spot at the best possible focus position.

Figure 3.4 shows that the profile of the laser is not round, and along the long axis (see dashed line) that there is a distinct second region of intensity. This smaller spot adjacent to the primary spot accounts for a significant proportion of the laser energy. From the width of the main part of the pulse (the peak at approximately 350μm

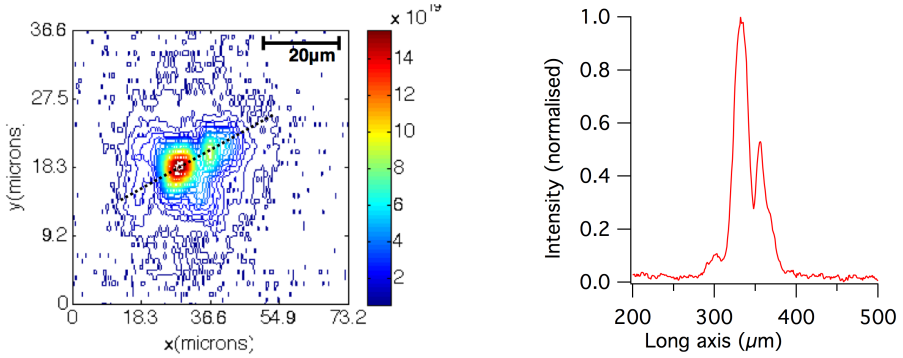

(a) Intensity map of laser spot (Wcm^{-2})

(b) Normalised intensity along long axis indicated in (a)

Figure 3.4: (a) Image taken with a CCD camera of the CW beam at best focus, showing significant asymmetry. (b) Plot along the long axis of the laser pulse

along the long axis) the focal spot is measured to be 7μm$\pm0.4\mu$m in diameter. The energy contained in the focal spot is assumed to follow the intensity distribution. A more quantitative description is presented in a radial energy plot in Figure 3.5. It is seen that around 25%±2% of the total laser energy is contained within the 7μm spot. Higher proportions of the laser energy are obtained as larger diameters are considered, e.g. a diameter of 14μm encompasses 30% of the laser energy.

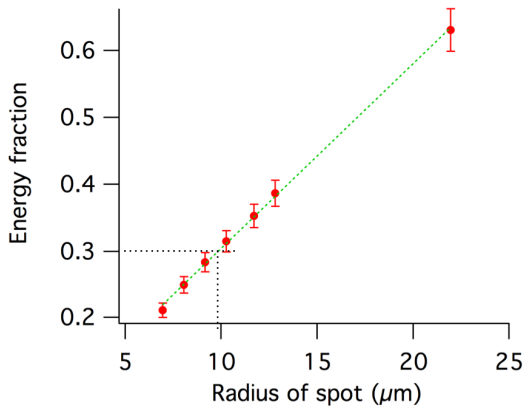

Figure 3.5: Image taken with a CCD camera of the CW beam at best focus, showing significant asymmetry in this case.

A tightly focussed, well characterised beam profile ensures that any anisotropy seen in x-ray emission, optical or particle diagnostics can be attributed to the physical phenomena taking place inside the target, and not simply due to asymmetry

of the original beam and experimental setup. It also has impact on the absorption of the laser light into the target through the introduction of perturbations to the critical density surface by hotspots in the beam as described in Section 2.6.1.1.

Figure 3.6 shows a shadowgraph taken at the same time as peak of the main beam strikes the target surface, showing that there is some expansion of the front surface due to the prepulse (or ASE). This probe beam is a pickoff from the main interaction beam that is frequency doubled ($\lambda = 532nm$), and used to illuminate the target in the transverse direction. In the image, the presence of expanding plasma causes refraction of probe light out of the aperture of the collecting lens. Therefore the dark regions outside of the bulk of the target are indicative of plasma formation. The image shows that expansion extends to distance of 5μm in the z

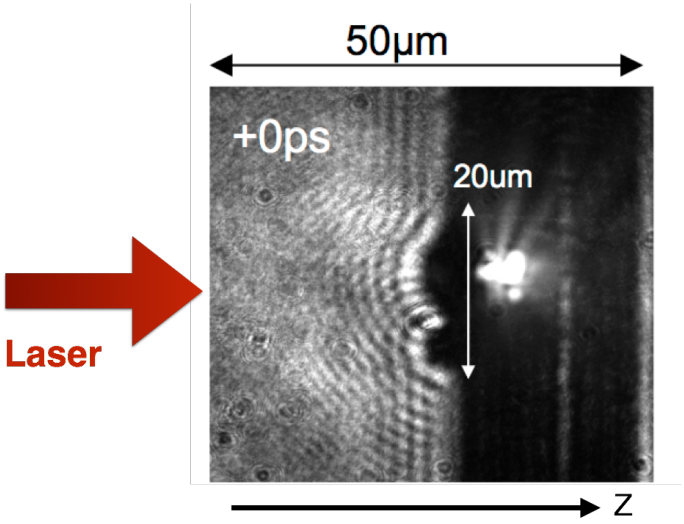

Figure 3.6: Frequency doubled optical probe showing that the shape of the expanding plasma is a close match to the laser focal spot profile.

direction at the peak of the laser pulse. It also shows a spatial profile (along the y-axis) similar to that in the long axis illustrated in Figure 3.4. The bright spot located at approximately the centre of the image is due to self emission.

3.3 X-ray Crystal Spectrometers

Measurement of x-ray emission has been used to diagnose fundamental plasma parameters such as temperature and density. Measurements of this type have been demonstrated as a powerful diagnostic tool, and are used frequently in hot dense plasma experiments [19, 49, 82–84].

The collection of x-rays from high intensity laser-solid experiments is challenging as spectrometer geometries need to be matched toe experimental constraints, and often low intensity x-ray signals need to be distinguished from a noisy environment. Focussing crystals allow combination of high luminosity spatially or spectrally resolved measurements to be made. In laser driven plasma experiments where analysis of a single spectral line is necessary, or the experimental environment is noisy, focussing crystals are advantageous.

3.3.1 Diffraction of x-rays from crystals

A regular crystal lattice performs the same task as a diffraction grating, x-rays are diffracted into several orders and dispersed according to their wavelength. Figure 3.7 shows dispersion of x-rays emitted from a point source plasma by a crystal surface. For a monochromatic x-ray beam of wavelength λ incident on the surface

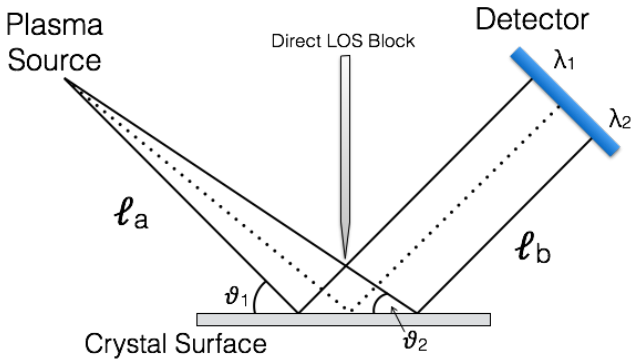

Figure 3.7: X-rays from a point source onto a Bragg crystal showing the variation of θ_B across crystal surface.

of a crystalline structure, the angle at which it will be diffracted is given by the well

known Bragg law,

$$n\lambda = 2dsin\theta_B \tag{3.1}$$

where n is an integer defining the order of diffraction from a crystal surface with lattice spacing $2d$ at the Bragg angle θ_B.

In the ideal case, a beam of x-rays is perfectly reflected from the crystal surface at the Bragg angle θ_B. In reality, there is a small distribution of angles about θ_B that is reflected. The angular variation is defined by the crystal rocking curve. Rocking curves are used to characterise the diffraction properties of each crystal for an incident photon wavelength λ. Usually they show a peak intensity about the Bragg angle θ_B. The full width half maximum gives the angular distribution of the reflection of a monochromatic light source as $\theta_B = \pm\Delta\theta_B$. The integrated reflectivity given by the integral of the rocking curve represents the efficiency with which radiation is reflected from the crystal surface.

Reflectivity of crystals is dependent on the wavelength of the incident radiation. For crystal materials, the absorption of x-rays is also dependent on the photon wavelength. In general, the absorption of x-rays falls as the photon energy increases, with the exception of absorption edges. This absorption is interrupted when the x-ray energy is equal to the binding energy of an electron shell, when the absorption abruptly rises [85]. In this case the K and L shells would be the most relevant, and these absorption edges would be seen at the energy corresponding to the ionisation potential for that shell. Crystals should be chosen such that absorption edges for their elemental composition are not present in, or near, the wavelength region of interest to avoid sudden variations in the reflectivity.

The spatial resolution, spectral resolution and the luminosity that can be achieved are dependent on the crystal lattice parameters, quality and geometry. It is crucial that crystals used in this way are as close to perfect as they can possibly be, to avoid any distortion of experimental data.

3.3.2 X-ray Dispersion

Differentiation of Bragg's law leads to the dispersion relation

$$n\frac{d\lambda}{d\theta} = 2dcos\theta \tag{3.2}$$

which can be written as

$$\frac{d\lambda}{\lambda} = cot\theta \; d\theta \tag{3.3}$$

Radiation at different Bragg angles is diffracted by the crystal to different points on the detector according to (3.1). Let be x the spatial coordinate of a detector placed perpendicular to the diffracted radiation. For an isotropically emitting point source, there is a variation in Bragg angle across the crystal surface due to the geometry of the spectrometer. Where $L = \ell_a + \ell_b$ is the source to detector distance, the variation across the crystal is $tan(d\theta) = \frac{dx}{L}$, and for small angles, $d\theta \approx \frac{dx}{L}$. By substituting into (3.2), the spectral dispersion of the crystal is defined as

$$\frac{d\lambda}{dx} = \frac{\lambda}{L} \; cot\theta = \frac{\lambda}{L \; tan\theta} \tag{3.4}$$

3.3.2.1 Spectral resolution

The ability of the spectrometer to resolve two wavelengths is determined by $d\theta$, which represents a range of angles and therefore a range in position at the detector dx by (3.4). For two wavelengths to be resolved by the spectrometer, the difference between their Bragg angles $d\theta_B = |\theta_{B,2} - \theta_{B,1}|$ must be greater than their angular width. The spectral resolution of the spectrometer is mainly determined by three main factors, namely the rocking curve, the source size and the detector element size.

Rocking Curve effects

Monochromatic x-rays from a point source are diffracted by the crystal surface over a small range of angles about the Bragg angle. This small angular width is denoted by $d\theta_{rc}$, and is given by the width of the rocking curve, given in radians. The spectral

resolution $d\theta_{rc}$ is substituted into (3.3) to give

$$\frac{d\lambda}{\lambda} = d\theta_{rc} cot\theta \tag{3.5}$$

Plasma source size

Laser driven plasma sources have a finite size, typically of the order of 100μm. This is defined here as distance S, measured in the direction perpendicular to the emitted radiation. Rays of different wavelengths emitted from two positions within the plasma, with two wavelengths can be diffracted to the same the same point on the detector. The difference in Bragg angle is estimated as $tan(d\theta_S) = S/L$, and for small angles, $d\theta_S \approx S/L$. By substitution into (3.3), we obtain

$$\frac{d\lambda}{\lambda} = cot\theta d\theta_S = \frac{S}{L}\, cot\theta \tag{3.6}$$

Detector element size

The detector in the plane of x perpendicular to the diffracted radiation is made up of a number of elements. For example, when using a CCD array as detector this will be the pixel size. To be resolved, wavelengths must be at least one element apart. The width of a single element is denoted as p. The change in angle subtended by p is $tan(d\theta_p) = \frac{p}{L} \approx \frac{p}{L}$, and by substituting into (3.3) we obtain,

$$\frac{\Delta\lambda}{\lambda} = \frac{p}{L} cot\theta \tag{3.7}$$

Combination of limitations

If the contribution to the spectral resolution from either the rocking curve $d\theta_{rc}$, or the plasma source size $d\theta_S$, is found to be very small when compared to the other, then it may be ignored. If they have an approximately equal contribution then they must both be taken into account. To do this they may be added in quadrature,

$$\frac{d\lambda}{\lambda} = \left(\frac{d\theta_{rc}^2 (S/L)^2}{tan^2\theta} \right)^{1/2} \tag{3.8}$$

This must also be compared to the limit of spectral resolution by the pixel size p (3.7). The limit on spectral resolution by the elements of the detector must be smaller than contributions from the rocking curve $d\theta_{rc}$ or plasma size $d\theta_S$.

3.3.3 Toroidal Crystal spectrometer

The toroidal geometry of the quartz (SiO_2) crystal allows focussing in one dimension to infer the size of the plasma source, alongside spectral dispersion of approximately 0.2Å. Over this range, the crystal spectral resolution $\frac{\Delta\lambda}{\lambda} \approx 7000$. The high dispersion toroidal spectrometer (HDTS) has a horizontal radius if curvature $R_h = 1404.5mm$, vertical radius of $R_h = 312.8mm$ and 2d=8.50979Å $(10\bar{1}0)$. The configuration of the HDTS is shown in Figure 3.8. Figure 3.8 shows the focussing of x-rays emitted from

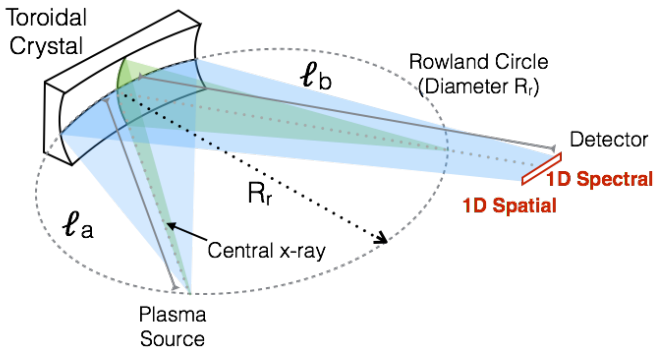

Figure 3.8: Schematic of the HDTS, showing emission from a plasma source placed on the Rowland circle, focussing in both the vertical and horizontal planes of the crystal.

a plasma source on the Rowland circle being focussed into a vertical and horizontal focus by the toroidal crystal. The Rowland Circle is described as a circle that passes through the centre of the crystal in both axes, and whose diameter is equal to the horizontal radius of the crystal surface. If a source is placed on this circle, the horizontal focus also lies on this circle. The distance from the crystal to the detector (ℓ_a) *must* be equal to the focal distance of the vertical axis, leading to a magnification $k = 1$. As $R_h \neq R_v$, the focal points of the two radii are not cospatial.

The focal length of the horizontal and vertical radii are [86].

$$f_h = \frac{R_h}{2} sin\theta_B \tag{3.9}$$

$$f_v = \frac{R_v}{2sin\theta_B} \tag{3.10}$$

By setting $f_h = f_v$, we obtain an expression which describes a condition for point to point focussing as

$$sin\theta_B = \sqrt{\frac{R_v}{R_h}} \tag{3.11}$$

This describes the Bragg angle at which both the source and detector can lie on the Rowland circle. Dispersion of an x-ray beam into a spectrum is achieved with the HDTS in the horizontal axis. For concurrent measurement of the x-ray emission spectrum and 1D imaging, the distance from the crystal to the detector (ℓ_b) *must* be equal to the focal distance of the vertical axis, leading to a magnification $k = 1$ if the source is placed on the Rowland circle.

The distance between the crystal and the detector ℓ_b is then the position of the detection plane on the Rowland circle, which for a given R_h is given by $\ell_b = R_h sin\theta_B$. To calculate the distance between the source and the crystal ℓ_a such that the focus of the vertical plane occurs on the Rowland circle, the distances are inserted into the thin lens equation. It can be shown [87] then that the distance between the plasma and the crystal is given by

$$d_{cd} = \frac{R_v R_h sin\theta_B}{2R_h sin^2\theta_B - R_v} \tag{3.12}$$

3.3.3.1 Dispersion Properties

In Chapter 4, the toroidal spectrometer was used to measure the Al He-β line to have a spectral linewidth of 6mÅ (min) to 12 mÅ (max). The contribution to spectral resolution of the spectral linewidths is calculated from this to give a range of $(\Delta\lambda/\lambda)_{min} = 9 \times 10^{-4}$ to $(\Delta\lambda/\lambda)_{max} = 1.8 \times 10^{-3}$.

The wavelength of the Al He-β line $\lambda = 6.635$Å, and for $n = 1$, $\theta_B = 51.2°$. For and x-ray film exposure where the Al He-β line is featured at x=1000 pixels chosen

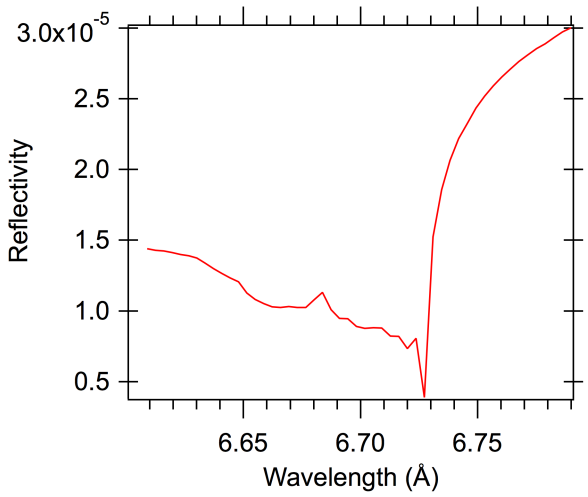

Figure 3.9: Reflectivity curve for the HDTS [88]

arbitrarily, (3.3) produces a linear dispersion for the wavelength at pixels on the detector x as $\lambda(x) = 5.789 - 4.6 \times 10^{-4}x$.

The reflectivity of the HDTS is measured experimentally, and is presented in Figure 3.9. This clearly shows the decrease in reflectivity approaching the K-edge for the Si element of the quartz crystal at 6.714Å, where the reflectivity dramatically drops. The Al He-β line at 6.635Å is in close proximity to this Si K-edge. The reflectivity value that is given at the position of the Al He-β is $1.4{\times}10^{-5}$. As the plasma is an extended source, implied by experimental data from the HDTS and the imager described in Section 3.3.4 to be approximately 100μm in size, (3.6) yields $(\Delta\lambda/\lambda) = 0.04 \times 10^{-3}$. The minimum resolvable wavelength for the detector corresponding to exposure of a single pixel of 80μm width in the dispersion direction is $(\Delta\lambda/\lambda) = 5.59 \times 10^{-5}$.

This crystal has a high dispersion and as such accurate alignment is required. The wavelength change over one pixel is seen to be 4.59×10^{-4}Å, and alignment to within 1/4000° is required to place the central wavelength onto the crystal surface. The dispersion over the whole range of the image is approximately 0.027 radians or 1.6°.

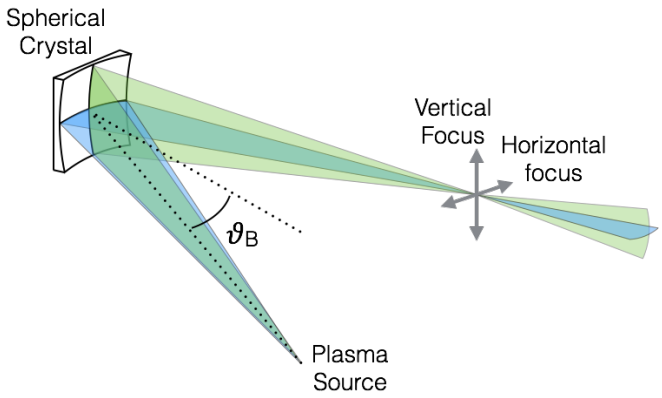

Figure 3.10: Schematic of the 2D imager for monochromatic imaging with a spherically bent quartz crystal. The focal point of the vertical (R_v) and horizontal (R_h) are coincident providing 2D imaging. The magnification of the system $k = \ell_b/\ell_a$.

3.3.4 Two-dimensional imaging crystal

The 2D imager is also uses a quartz crystal with $(10\bar{1}1)$ crystal planes, 2d=6.68647Å. To observe the Al He-β the Bragg angle $\theta_B = 82.668°$. The 2D imager is operated in a scheme where the source and the detection plane do not sit on the Rowland circle. It has a high magnification (k=33.7) to obtain the maximum possible resolution at the plasma. Figure 3.10 shows the configuration of the 2D imager, and the coincident focussing of the vertical and horizontal planes to form an imaging plane.

The spherical crystal used here has a horizontal bending radius $R_h = 145.4mm$, and vertical bending radius of $R_h = 143.2mm$. The distance between the crystal and the plasma, ℓ_a and the distance from the crystal to the detector, ℓ_b are given by 3.13 and 3.14.

$$\ell_a = \frac{k+1}{k}\frac{R_h}{2}sin\theta_B \tag{3.13}$$

$$\ell_b = (k+1)\frac{R_h}{2}sin\theta_B \tag{3.14}$$

where the magnification of the system $k = \frac{\ell_b}{\ell_a}$.

Experimentally, the physical constraints of the environment restrict the ideal location of the imager. Taking (3.14) and the magnification, ℓ_a can be shown in terms of a known ℓ_b given in (3.15).

$$\ell_a = \frac{\ell_b f}{\ell_b - f} \tag{3.15}$$

The relation (3.15), where $f = \frac{R_h}{2} sin\theta_B$, and for a fixed ℓ_b allows the crystal to source distance ℓ_a to be determined. Figure 3.11 shows a graphical representation of the change in ℓ_b as we change the values of ℓ_a. This shows that the distance given by f, represents the closest that we can place our 2D imaging crystal to the target for an image to form.

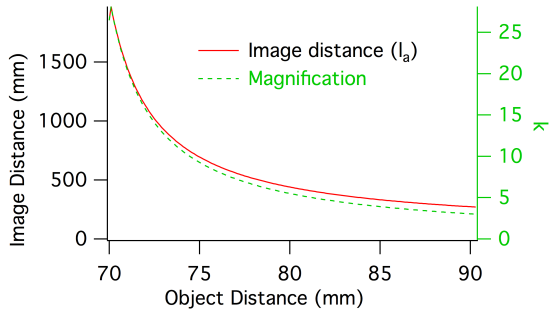

Figure 3.11: Change of image distance (ℓ_b) with object distance (ℓ_a) for the 2D imaging crystal. For $\ell_a \to 70mm$, $\ell_b \to \infty$. The magnification is shown on the right axis.

The plot of (3.15) in Figure 3.11 shows that for distances closer than ℓ_a of 71.9mm, the magnification of the system is effectively zero and the image forms at an infinite distance. Table 3.1 shows how the image and object distances vary with magnification, given in units of f.

k	ℓ_a(f)	ℓ_b(f)
1	2	2
3	1.3	4
5	1.2	6
10	1.1	11
15	1.06	16
30	1.03	31

Table 3.1: The magnification and image distance of the 2D imager is extremely sensitive to the distance it is placed from the plasma source.

Table 3.1 shows that for magnifications $k > 1$, that small changes in the value of ℓ_a causes large changes in the length ℓ_b. As magnification increases from 15 to 30, $\Delta\ell_a = 2.16mm$ or a $\Delta\ell_a = 1079mm$. This diagnostic is sensitive to the distance between the target and the crystal in this configuration.

3.3.5 Dispersion properties

The detection media used here is x-ray film, which has a grain size on the order of 1.5μm [89] and so the limit on the resolution is driven by the way in which the x-ray film is processed. The film was scanned using a densitometer, with a resolution of 32μm. This combined with the magnification of the system creates an imaging resolution of 0.95μm at the plasma source. An estimate of the source size made from the experimental data gives a source of approximately 30μm diameter. For a source of this size S, (3.6) yields $\Delta\lambda/\lambda = 2.49 \times 10^{-4}$. In comparison, the spectral line width is found by the use of the toroidal spectrometer (HDTS) detailed in Section 3.3.3.1, where $(\Delta\lambda/\lambda)_{min} = 9 \times 10^{-4}$ and $(\Delta\lambda/\lambda)_{max} = 1.8 \times 10^{-3}$.

The integrated reflectivity of the crystal here is assumed to be a constant value which is calculated here to be 157μrad [90]. The crystal reflects over 40% of the photons incident on its surface at the He-β wavelength of 6.635Å [90].

For the Al He-β at this magnification, the spectral window of the crystal is driven by the variation of the Bragg angle across the crystal surface and is [86].

$$\frac{\Delta\lambda}{\lambda} = \frac{(k-1)}{(k+1)} \frac{2r_{aperture}}{R_h tan\theta} \tag{3.16}$$

where $2r_{aperture}$ is the diameter of the aperture placed in front of the crystal.

For the extended image, the Bragg angle variation along the image position must be smaller than the spectral window. This variation would correspond to a shift of the spectral window along the image position. Scanned images are approximately 148μm in size, and the corresponding angular change θ the shift is

$$\frac{\Delta\lambda}{\lambda} = \frac{\Delta\Theta}{tan\theta_B} \tag{3.17}$$

The angular change across the image (3.17) is 16 times smaller than the angular change caused from position across the crystal (3.16), meaning that the variation along the image positions is much smaller than the spectral window.

The number of photons of the image captured is related to the number of photons

emitted from the plasma, given by [86].

$$\frac{N_{ref}}{N_{plasma}} = \frac{(2k)^2}{k^2 - 1} \frac{\Delta \mathrm{h}_{crystal} R_{int}}{sin\Theta_0 R_h} \tag{3.18}$$

Where R_{int} is the integrated reflectivity, $\Delta \mathrm{h}_{crystal}$ is the crystal aperture height vertically, k is the magnification and R_h is the vertical bending radius of the imager. The number of photons reflected by the crystal is also given in the same way such that $\frac{N_{ref}}{N_{plasma}} = \frac{E_{ref}}{E_{plasma}}$ [86]. By plotting N_{ref}/N_{plasma} for different values of k, we obtain the plot shown in Figure 3.12.

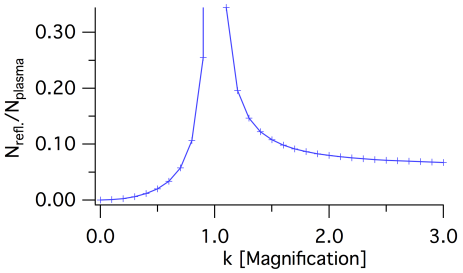

Figure 3.12: Ratio of reflected energy to energy emitted by the plasma as a function of magnification showing that the peak in reflected energy occurs at k=1. Here, $E_{ref}/E_{plasma} \rightarrow \infty$.

Figure 3.12 shows that the peak reflected energy and hence, the peak reflected photon numbers occurs for k=1. Extension of this plot out to k=30 which is more relevant to the magnification used by the 2D imaging crystal in practice, $E_{ref}/E_{plasma} \approx 0.06$.

3.3.6 Detection Threshold

The generation of a 2D monochromatic image resulting from a single spectral line is affected by several factors, and is largely dominated by the a strong dependence on material temperature. The observable temperature range of the Al He-β line is seen to be approximately 300-700eV (see Figure 2.3).

To estimate the detection threshold in addition to effects already discussed, it is pessimistically assumed that the x-ray film ceases to detect a flux of less than 0.1 photons/μm^{-2} (see 4.7). This corresponds to a He-β flux of approximately

$1 \times 10^7 \mathrm{Wcm}^{-2}$, which is required to observe any signal at all. This is far lower than the observable fluxes of the order of $10^{12}\mathrm{Wcm}^{-2}$ given for the temperature range (See Figure 2.10.2). Therefore, the limiting factor here is the temperature dependence of the atomic transitions. Therefore, in areas of low or no emission we can reasonably assume that this is a direct result of changing target temperature and not a feature of the instrument.

3.3.7 HOPG Spectrometer

Two ZYA grade, highly ordered pyrolytic graphite (HOPG) crystals were used to capture the σ and π polarised components of the Al Ly-α line. Whilst s- and p-polarisation is defined for the laser, polarised line spectra are referred to herein as σ- and π- polarised. The HOPG crystals are in the 002 orientation, have mosaicity of 0.4°, and 2d=6.708Å, Bragg diffraction of the S Ly-α line components occurs at 44.87° (Ly-α_1) and 44.81° (Ly-α_2). This also works well for Ni Ly-α in third order at 8.1keV which will not be discussed here.

Figure 3.13 shows the two flat highly-oriented pyrolytic graphite (HOPG) (002) crystals, aligned parallel and perpendicular to the target surface, each perpendicular to the quantisation axis which defined by the direction of fast electron propagation (z). This is the line defining the laser axis directly through the centre of the target along the target normal.

The crystal perpendicular to the target surface captures the σ-polarised emission and the crystal parallel with the target surface captures the π-polarised component. Both spectrometers are positioned at a Bragg angle $\theta_B = 45°$, and both components are recorded on a single shot.

Each image plate is protected from the effected noise and energetic particles as much as possible with beryllium filters, and the crystals protected from debris with mylar sheets. This experiment was carried out with the Vulcan laser facility, facility parameters are outlined in detail in Chapter 3.

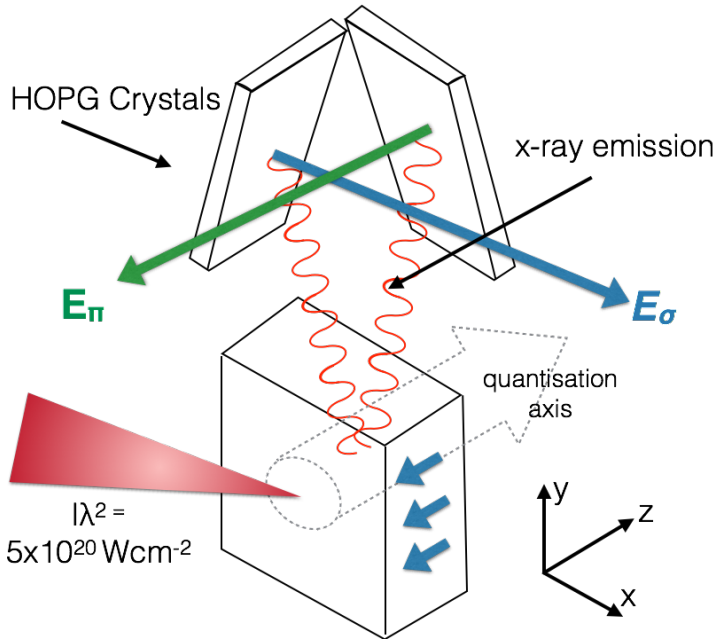

Figure 3.13: Experimental layout of the HOPG crystal spectrometers to isolate the σ and π polarised components to x-ray emission of the Ni Ly-α line.

3.3.7.1 Diffraction properties

The HOPG crystal is a highly reflective optical element in the keV range [86, 91, 92]. The mosaic structure of the crystal provides a larger angular spread of the reflection and a greater spectral resolution than can be achieved with perfect crystal structures. The reflectivity of these crystals is dependent on whether the electric field vector of the incoming radiation is parallel or perpendicular to the plane of incidence, i.e. polarisation. The diffraction curve calculated for both σ and π polarisation states is calculated by the x-ray optics package XOP [93], and is shown in Figure 3.14.

Figure 3.14 shows that for a Bragg angle of 45°, the π component of the reflection falls away almost completely, leaving the sigma component in isolation. High values of reflectivity > 0.9 are seen at the Bragg angle θ_B. The diffraction properties are determined by the crystal mosaicity, and the width of the Bragg reflection shown in Figure 3.14. The width of the Bragg reflection defines a limit on the energy resolution that can be achieved given by $\Delta E = cot\theta d\theta$. For S Ly-$\alpha$ line components (θ_B = 44.87$\circ$ for Ly-α_1, θ_B = 44.81$\circ$ for Ly-α_2) $\Delta E/E = 2.5113 \times 10^{-4}$ and 2.5166×10^{-4}

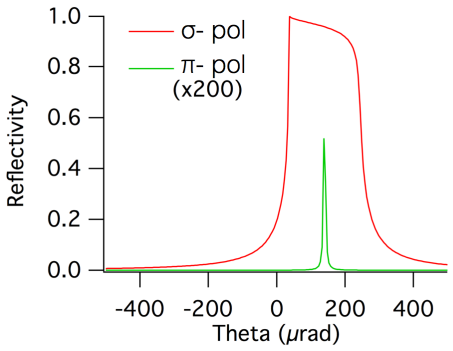

Figure 3.14: Rocking curve for the s and p polarised components of polarised line emission from the 002 plane of a HOPG crystal. For a Bragg angle here of 45° the p polarised component is vanishingly small in comparison to the s polarised.

respectively.

The mosaic crystal is composed of many randomly oriented crystallites and is not one single crystal structure. Each individual crystallite is at its own orientation within the crystal and the spread of their angles is described by the mosaicity of 0.4°. Each crystallite can be considered an ideal crystal, and the diffraction from the whole crystal considered to be the convolution of diffraction from a number of randomly oriented perfect crystals. Diffraction from the mosaic crystal structure then is not as simple as from single perfect crystal, and has some unique focusing effects shown in Figure 3.15.

Figure 3.15 shows the structure of the crystal. Rays emitted from a single point source with the same energy are diffracted by the crystallites within the mosaic crystal according to Bragg's law (as for perfect crystals). Therefore, the mosaic spread of the crystal determines the energy range and the peak reflectivity [94]. Due to the random structure, a ray must travel some distance into the crystal until it encounters a crystallite at the correct angle for Bragg reflection [95]. Rays of the same energy emitted from a point source are focussed into a single point in the image plane if the crystallites lie on the Rowland circle [94]. Therefore the crystal to source and crystal to detector distances must be equal, and this effect known as parafocusing or mosaic focusing occurs at k=1 [92, 94, 95]. Rays of different energies, will be focussed to different points in the image plane due to the change

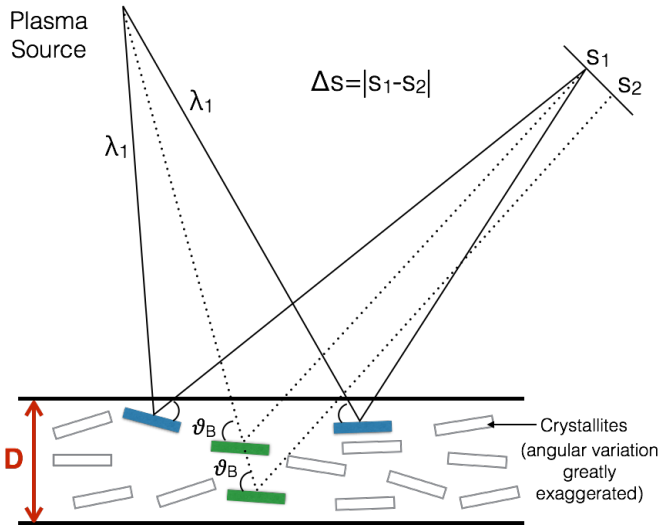

Figure 3.15: Parafocusing from mosaic crystal in a k=1 geometry. Two rays of incident wavelength λ_1 from two angles find two separate crystallites that are at the correct Bragg angle, focused to a single point at the detector. The origin of line smearing Δs is due to depth travelled by a single ray, and a slightly different point of focus. Two incoming rays of λ_2 would be focused at a different position on the detector.

in Bragg angle [95], providing energy dispersion at the detector. The mosaicity of the crystal makes it possible to obtain a spectrum of energies from a polychromatic beam for a fixed angle of incidence [92]. This makes it particularly suited then to measurements of large sources [96]. In this k=1 geometry, the best energy resolution is achieved [94], and the intensity at the image plane is enhanced [92].

As the ray has to travel into the solid to find a correctly aligned crystallite, a small broadening, s, due to the small change in focal point is caused, and shown in Figure 3.15. Therefore for HOPG and other mosaic crystals, the thickness D is important as it sets an upper limit on the depth photons can be diffracted from. The broadening in the dispersion direction due to target thickness at the detector plane is estimated from geometry to be $\Delta s = 2Dcos\theta$ [94]. As the thickness of the crystal rises, the likelihood of any one ray finding a crystallite at the Bragg angle increases, and a higher photon flux. However, this increases the smearing effect which has an increasingly detrimental effect on energy resolution. The inverse is also true and as such, design of these crystals is a trade off between intensity and

the energy resolution that can be achieved. For S Ly-α_1 and Ly-α_2 line components, $s = 3.132\mu$m and 3.126μm respectively for D=2mm.

3.3.8 Focussing spectrometer with spatial resolution (FSSR)

The focussing spectrometer with spatial resolution (FSSR) consists of a spherically bent mica crystal ($K_2O - 3Al_2O_3 - 6SiO_2 - 2H_2O$) with a crystal lattice spacing 2d=19.9376Å (004) and a radius of curvature R=150mm [97].

In this experiment the spectrometer was aligned such that spectra of 7.0Å−8.4Å was observed from the front surface of the target in the n=2 order [98].

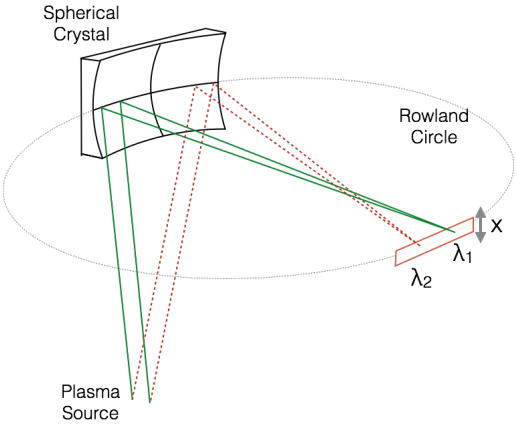

Figure 3.16: Schematic of FSSR with an extended plasma source emitting two wavelengths focussed onto the detector on the Rowland circle. The focussed FSSR provides spectral dispersion in the horizontal plane and imaging in the vertical direction. [98]

Figure 3.16 shows a schematic of the spherical crystal with two incident wavelengths. Fogging of the signal due to fast electrons was prevented by a pair of 0.5T magnets in front of the crystal. Spectra from this crystal were recorded on x-ray film, which was filtered from visible signal and stray light by 25μm of Be, or Al coated polypropylene. Mylar filtering was also used to reduce the noise level and prevent saturation of the film.

Figure 3.17 shows the reflectivity of the FSSR for the Al He-α, and shows that $d\theta = 245\mu$rad. The spectral resolving power of the instrument due to the reflectivity curve is thus $\lambda/\Delta\lambda = 5056.4$ (in agreement with [97]).

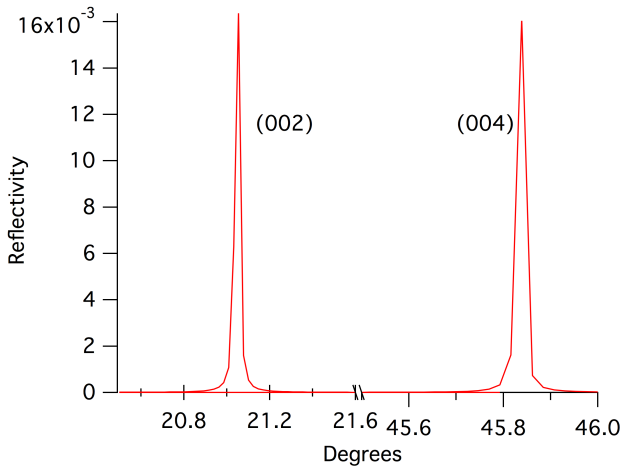

Figure 3.17: Reflectivity of the FSSR for n=1 and n=2 where $n\lambda = 2dsin\theta$ and $\theta = 45°$, Al He-α at 1598.2 eV. The reflectivity profile shows the sum of contributions from s and p polarisation and has a FWHM = 245 μrad.

3.4 Summary

In this chapter the key diagnostics have been summarised. Firstly a discussion of the basic function of the Vulcan laser system is given, followed by the key characteristics of the laser and the focal spot it produces in Section 3.2. The profile of the pulse spatially and temporally is shown in Section 3.2. This is important as it determines characteristics such as the scale length of the experiment. This was found in this case to be approximately 10μm. As described in Chapter 2 this has direct impact on the absorption of the laser pulse into the target.

The crystal spectrometers used in this these are also outlined. The 2D imager outlined in Section 3.3.4 is used extensively in Chapter 4 to capture 2D images of a single spectral line for measurements of the electron beam divergence, and of the plasma temperature. The toroidal crystal spectrometer in Section 3.3.3 is used to capture the spectral line profile, plasma source size and plasma density measurements in Chapter 4 to provide additional information for the 2D imagine measurements. The pair of HOPG crystal spectrometers outline in Section 3.3.7 is used in Chapter 6 to produce measurements of the two polarised components of spectral emission. Finally, the FSSR spectrometer detailed in Section 3.3.8 is used

in Chapter 5 for high spectral resolution measurements of hollow atom emissions. All of the experimental data presented in the remainder of this was a result of these spectrometers.

Chapter 4

Constraining Fast Electron Divergence in Solid Targets

4.1 Overview

Presented in this chapter are measurements of fast electron beam transport and target heating using x-ray imaging in one and two dimensions. The angular divergence of the electron beam inside a solid density target is topic of particular interest as it defines several parameters for applications in fast ignition [1], and more generally for isochoric heating of matter to high temperature and density regimes [99, 100]. There is also significant wider impact in the generation of laser driven ion and x-ray sources [7, 101, 102]. There have been many attempts to characterise the fast electron beam in terms of it's energy and divergence, and the experimental and modelling results available from this has yielded a wealth of data [19]. The consensus is that the beam is divergent. The next step is to provide data that can constrain the divergence to certain angles for a given set of input parameters.

The key aim is to obtain an estimation of fast electron beam divergence, and to use experimental data to constrain some of the user defined input parameters currently used in the simulation of high energy density experiments. In this approach, thermal spectral lines are used to spatially resolve the target temperature, which is directly related to spectral emission (see Chapter 2). In-situ measurement of intensely heated material in the target can be used to infer the location of the fast electron current. This combined with buried layer targetry allows the fast elec-

tron current to be tracked at several target depths to produce an estimate of it's divergence.

This chapter details how 2D monochromatic x-ray imaging can be used to give precise measurements of target heating. Absolute calibration of x-ray film allows calculation of photon numbers emitted form the plasma and the plasma temperature is deduced. Spatially resolved temperature data is compared to the results of plasma kinetic modelling to constrain the input parameters defined by the user. Also described here is the reverse process, whereby hybrid-PIC modelling is used to generate synthetic x-ray emission data from a target temperature profile.

4.2 Experimental method

The Vulcan PW laser facility as outlined in Section 3.2 was used with buried layer targetry to diagnose target heating by imaging the emission of the Al He-β line. The key diagnostics used in this chapter are a 2D imaging crystal, and a high dispersion toroidal spectrometer (HDTS) as described in Sections 3.3.4 and 3.3.3 respectively.

All targets used were of a buried layer configuration as shown in Figure 4.1(a). A plastic (CH) slab of variable thickness has a thin 0.1μm buried layer of aluminium placed at varying depths. The buried layers used in this experiment were positioned in the region close to the interaction, and emission was seen at depths of 1 -15μm where relatively little experimental data exists. Shots were also taken with deeper buried layers, and no emission was seen.

Previous experimental measurements and simulations have shown that the bulk target temperatures expected from this experiment vary from a few tens of eV, up to several hundreds of eV, which suits the emission of the Al He-β line.

Photons emitted from the target are diffracted from a Bragg crystal, and focussed to form an image. Making effective use of a monochromatic imager is dependent on the choice of spectral line. The chosen line must satisfy the Bragg condition for the crystal (see Section 3.3.4), and ideally exhibit intense emission from temperatures likely to be present in the experiment, be emitted within the spectral bandwidth of

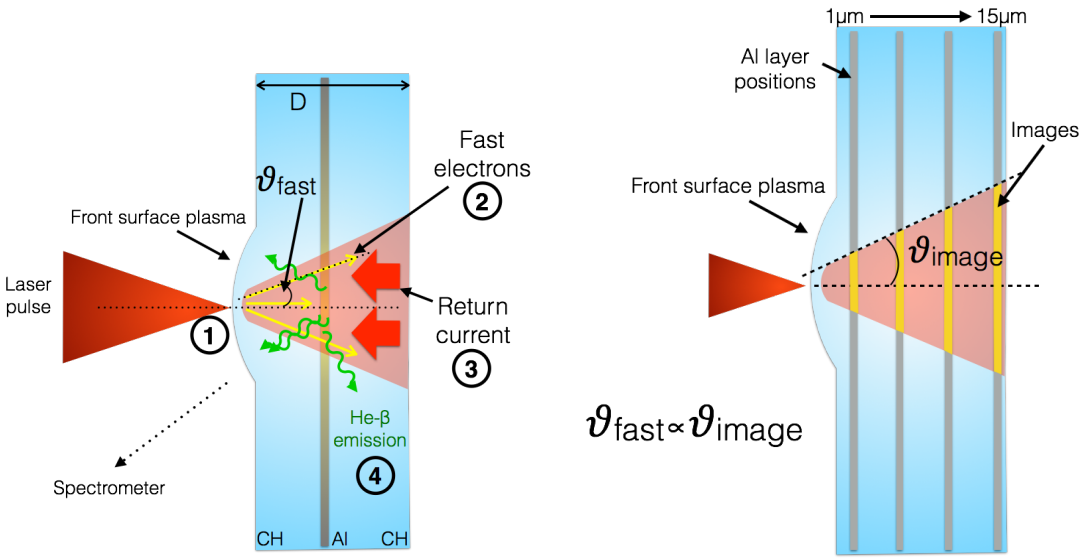

Figure 4.1: (a)Experimental schematic showing ① electrons are generated at the relativistic n_{crit} and ② stream through the target creating a charge imbalance balanced by ③ the propagation of a return current which ④ resistively heats the target, causing x-ray emission from the heated region. Also shown is total target thickness, D (b) Sketch of 4 slices into target depth, showing for a divergent fast electron beam that diameter of x-ray emission is expected to increase with depth (z)

the crystal, and be optically thin.

An intense laser source incident on the surface of a solid density target as shown in Figure 4.1 creates plasma on the surface of the target. At the relativistically corrected critical density, a beam of fast electrons is accelerated into the target, creating a large charge imbalance across the target. The current of the fast electron beam far exceeds the Alfvén limit (see Section 2.8.1), and a counter propagating return current is generated [103]. This beam is cooler, more collisional and resistively heats the target material as it propagates. The buried layer is heated in this way and causes x-rays to be emitted from intensely heated regions. The spatial and temporal profile of the laser pulse as it strikes the front surface of the target is important to understand as it is the fundamental drive of the whole process leading to x-ray emission. A sketch of how x-ray emission for a diverging fast electron beam could be expected to evolve is given in Figure 4.1(b). The figure shows four layers representing

buried layer for increasing depth into the target, showing the anticipated increase in diameter of the emission region. This is for the case of the diverging electron beam, as the fast electron current and return current are approximately cospatial, and the heated region is anticipated to reflect this [51].

For information on the focal spot of the laser, refer to Chapter 3.

4.3 2D Imaging Data and Results

A sample of the images captured by the 2D imaging crystal as described in Section 3.3.4 are shown for depths of 1μm and 5μm beneath the front surface of the target in Figure 4.2.

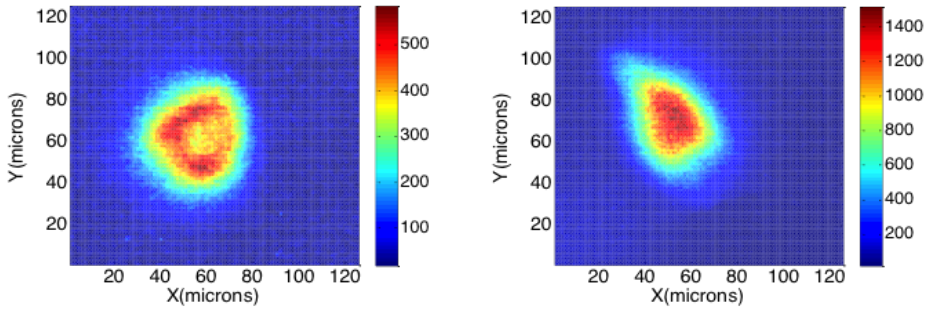

(a) (b)

Figure 4.2: Two-dimensional images of the Al He-β line emitted from a buried Al tracer layer in a CH target at depths of (a) 1μm and (b) 5μm. Colour bars for each image represent the image intensity in arbitrary units.

The images presented in Figure 4.2 are monochromatic images of a single spectral line with 2D spatial resolution, at a known depth within the target. As outlined in Section 2.10.2 the emission of thermal spectral lines emission is strongly dependant on material temperature, and each photon in the image represents the presence of material with a limited range of material temperatures.

Here the Al He-β spectral line is used and each of the images represents material at a temperature between 300 and 700eV. As the ionisation distribution in Figure 2.3 is peaked around 400eV, it has been further assumed that the material temperature where there is photon emission is at, or close to this value as emission is dominated

by material at this temperature.

The image shown in Figure 4.2(a) is approximately circular, and has a central region approximately 16μm in diameter that shows a reduced emission intensity compared to the region surrounding it, producing a ring like appearance. This shows the effect on emission of material $> 400\ eV$ and $< 400eV$ simultaneously. The outer edge of the image is due to material dropping to temperatures below the threshold for emission, around 20μm from the centre of the target. The centre of the image is coincident with the location of the laser spot on the front surface of the target, and material temperatures here are expected to be high. Figure 4.3 shows that for high temperatures, the population of helium like ions drops. Therefore emission in this region drops, producing the hollow structure in the centre of the image seen in Figure 4.2(a).

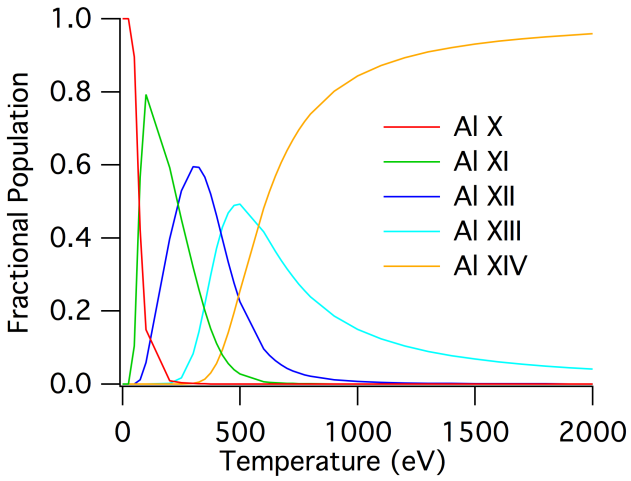

Figure 4.3: Fractional population of hydrogen to boron like ions with increasing temperature for solid aluminium. At temperatures of approximately 500 eV, there is a peak in the population of helium like ions.

The image shown in Figure 4.2(b) has an asymmetric shape. It is also brightest in the centre revealing that temperatures are not likely to have far exceeded 400eV. This peaked emission profile implies that the outer limit of the image represents the presence of cold material below the temperature threshold for significant populations of He-like ions.

The accuracy of extracting a single value for the diameter of these images depends on their asymmetry. Figure 4.2(b) illustrates the difficulty in defining a single radius for asymmetrical images. This was done by taking several diameters across each image and obtaining an average. As a result, those with a roughly circular shape have far smaller errors than those that are non-circular.

Figure 4.4 shows the diameter of all images as a function of target depth, revealing that their diameter decreases with increasing depth into the target. In the literature, a diverging electron beam has been consistently shown [19, 49, 104]. This indicates that a direct correlation of the image diameter to fast electron beam diameter does not provide an adequate explanation for the emission images evolution with depth.

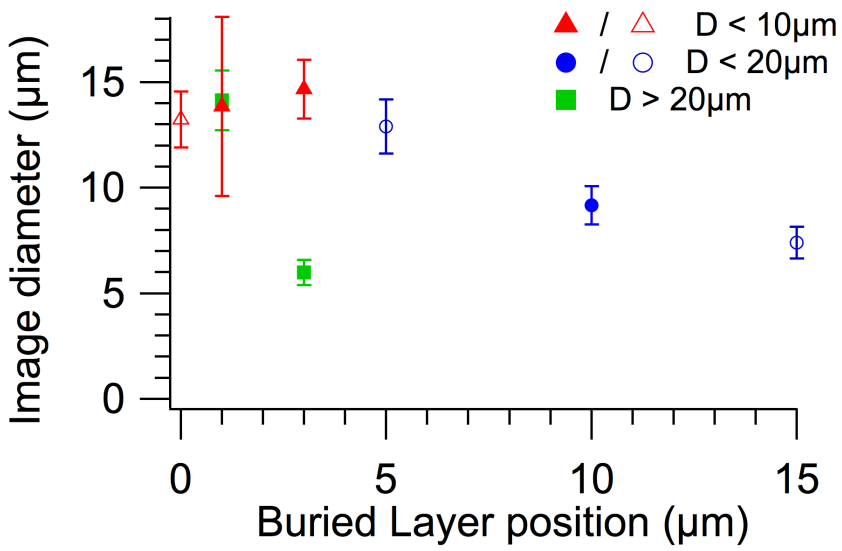

Figure 4.4: Diameter of the images inferred from the 2D imager data with increasing depth of a thin Al buried layer into a CH target. Symbols are representative of overall target thickness, and the presence of the long pulse beam of Vulcan to preheat the target for up to 1.5ns before the peak of the short pulse (more detail in text).

At depths greater than 5μm a steady decrease in the image diameter is observed. The shape and colour of the points on Figure 4.4 indicate the target thickness. Triangular, square and circular points represent target thicknesses of $< 10\mu$m, $< 20\mu$m and $> 20\mu$m respectively. The effects of refluxing electrons is greater for

thinner targets, and although it has been shown that this cannot be completely eradicated at thicknesses of around 20μm in dielectric materials, targets with much thicker rear surface layers of approximately 100μm were used to help minimise it [4, 105, 106]. Front surface plasma is created 1ns prior to the arrival of the short pulse beam by using long pulse beam. Images where the long pulse beam was used are indicated by hollow points on Figure 4.4. The level of preplasma produced by the long pulse beam changes the scalelength of the experiment in comparison to the short pulse beam only. In this data set, no correlation with either target thickness or an increased level of prepulse is seen.

There is no dependence of emission diameter with scalelength, despite the fact that additional expanding plasma may change the critical surface position, and perhaps also the profile of the source. The impact of the overall target thickness is also not seen. If refluxing electrons were playing a significant role here then image diameter should be affected by target thickness, and larger image diameters could be seen for thinner targets. There is no clear relationship between total target thickness and image diameter. The diameter of the images also does not change with increased laser energy on target. All shots in this experiment were carried out at best focus and so the opportunity to explore the effects of laser focal spot size remains for future work.

Figure 4.5 shows an anomalous image recorded during the experiment. For a laser intensity of $1 \times 10^{20} W cm^{-2}$ shot at best focus and a depth of 1μm into the target, this image was observed.

The image in Figure 4.5 is seen to be much larger than the rest of those obtained from the imager. It is twice as tall, but maintains a similar width to the other images. The cause of this distortion is not clear. The brightness of the image is consistent with that of other images, and it also shows a structure similar to that shown in Figure 4.2(a).

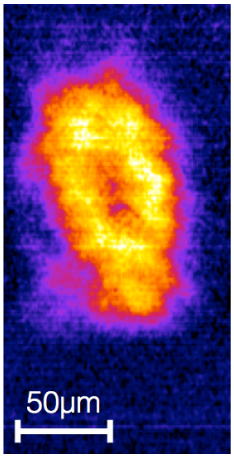

Figure 4.5: 2D imager data for shot 031504, laser intensity of $1 \times 10^{20} W cm^{-2}$ shot at a depth of 1μm into a CH/Al/CH buried layer target.

4.3.1 Calculating Plasma Temperature

Imaging data was taken on AGFA Structerix D7 x-ray film, and analysed by a high resolution densitometer to measure the optical density (OD) as a quantitative measure of the film exposure. The optical density obtained for each pixel is used to arrive at a measurement of line flux and therefore plasma temperature using the following method. Transmission of the film (T) is given by 4.1.

$$T = \frac{J_T}{J_0} = \frac{(J^n_{curr} - J^0_{curr})}{(J^{max}_{curr} - J^0_{curr})} \tag{4.1}$$

Where J^n_{curr} is the current in the n^{th} pixel analysed, J^0_{curr} is the dark current or minimum current seen through the film, and J^{max}_{curr} is the maximum current seen through the film. The optical density of the exposed x-ray film is expressed as a logarithmic ratio between the incident and transmitted radiation in 4.2.

$$OD(\lambda) = -\log_{10}\left(\frac{1}{T}\right) \tag{4.2}$$

Experimental factors such as the filter transmission, magnification, crystal reflectivity and bandwidth have all been taken into account in 4.3 [86].

$$N_{ref} = N_L \frac{(2k)^2}{k^2 - 1} \frac{\Delta \mathrm{h} R_{int}}{\sin\theta_0 R_h} \tag{4.3}$$

Where N_{ref} is the number of photons reflected from the crystal surface and N_L is the number of photons emitted by the plasma, k is the magnification, Δh is the

crystal height in the vertical direction, R_{int} is the integrated reflectivity, θ_B is the Bragg angle and R_h is the radius of curvature of the crystal. Rearranging (4.3) for the total number of photons in the spectral line gives N_L. Corrections are needed for the detector filters and solid angle subtended by the crystal.

The solid angle subtended by the crystal is accounted for by assuming that the plasma emits isotropically, and that the crystal area forms a small fraction of a sphere surrounding the target of radius ℓ_a=74mm (the distance between the crystal surface and the target front surface).

Figure 4.6 compares the bandwidth of the crystal with the spectrum collected by the high dispersion toroidal spectrometer (Section 3.3.3). This bandwidth encompasses the entire spectral line and thus the spectral lineshape is not expected to be important. Backgrounds are subtracted from the data by extrapolating from

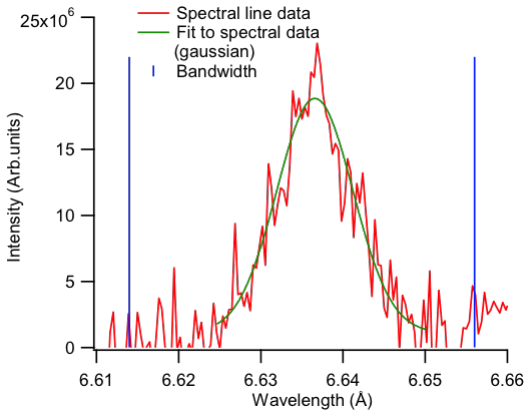

Figure 4.6: Bandwidth of the 2D imager compared to experimental measurement of the He-β spectral line with a toroidal crystal spectrometer.

regions around the image across the image.

This specific film type has been absolutely calibrated experimentally and compared with previous data [107] by Uschmann et al. [88]. This data has been used to produce a calibration curve showing photons per micron present on the x-ray film as shown in Figure 4.7. A linear interpolation routine between each of the points on the calibration curve graph is applied to the image pixels above the threshold value, and they are converted from optical density (the output of densitometry) to

photons/μm^2.

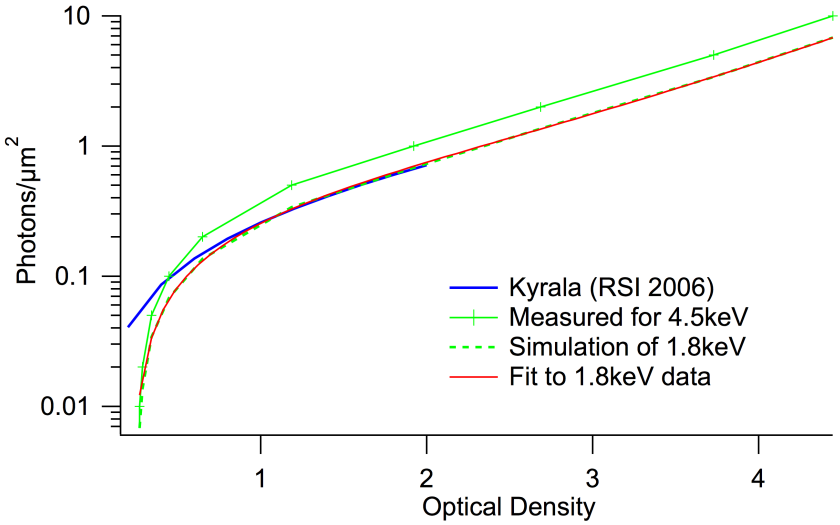

Figure 4.7: Calibration of AGFA D7 Structerix film. Previous work of Kyrala et al. [107] shows a good fit to simulation of 1.8keV photons for optical density > 0.5 . Fit to 1.8keV data (red) also shows a good fit to previous work, and measured film density for 4.5keV photons [88] (green) also shown.

Using this procedure, each of the images shown in Figure 4.4 is converted into a photon flux at the detector. Figure 4.8 shows the result for the two images shown in Figure 4.2. Figure 4.8 shows that the maximum flux for Figure 4.8(a) is higher than

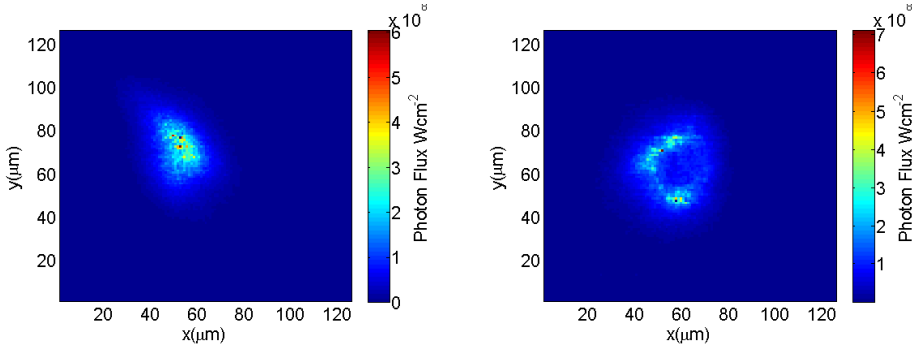

Figure 4.8: Photon flux (Wcm^{-2}) calculated from 2D imager data shown in Figure 4.2

that in Figure 4.8(b). From this, the plasma temperature can be calculated for each point on the film. By using (4.3) and having knowledge of how x-ray emission varies with temperature, a single value for temperature from each image is derived. This

is done by taking an average over the pixels that have contributed to the estimate. Temperatures calculated in this way for each of the data points shown in Figure 4.4 is shown in Figure 4.9.

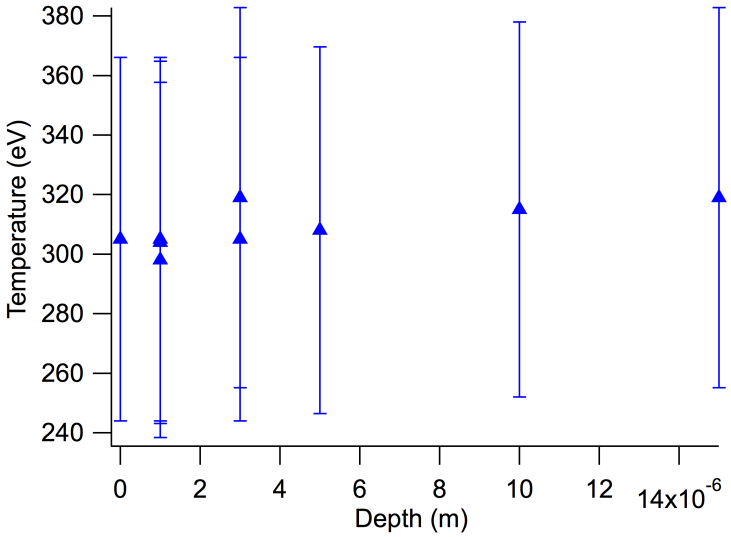

Figure 4.9: Plasma temperatures (eV) derived directly from experimental data recorded on absolutely calibrated x-ray film. These imply that the plasma temperature is approximately 300eV, and that little variation is seen with increasing target depth.

Figure 4.9 shows that the target temperature derived from the x-ray data is approximately 300eV. A small variation in temperature ($> 20eV$) over the target depth is seen although this is not significant given the size of the errors. Literature indicates temperatures fall up to 20% over the same target depth [15, 17, 108, 109]. The errors shown for the temperature estimates is given by the standard deviation, showing around 20% uncertainty. In addition to the data presented in Figure 4.4, the data in Figure 4.5 has been included, as the estimate of a temperature is not dependent on the shape or diameter of the image. These measurements do not show the variation in temperature with increasing target depth as the errors are too large. The average of these estimates places the plasma temperature at 308eV$\pm$53eV.

4.4 Simulation

As shown in Figure 2.3, Al He-β emission is peaked, and as a first approximation it is assumed that the overall emitted flux of this line is dominated by emission from material at 400eV. It follows therefore that the diameter of the emission area follows the diameter of the region of material at this temperature. Therefore for a given target temperature profile, the region of 400eV material and hence an anticipated emission region can be found.

The THOR model [69] was used to examine target heating from the interaction of a PW laser pulse and solid target. The key input variables are identified as the electron divergence angle set initially to 50°, the absorption fraction $\eta = 0.3$ and the source size set to the laser focal spot size of 7μm. The simulated laser intensity is 5×10^{20}Wcm^{-2} in a 1ps pulse onto a 30μm CH target. The buried layer was not included in this simulation. Comparison of the temperatures calculated from the images in Figure 4.9 are compared with the THOR temperature estimation in Figure 4.10.

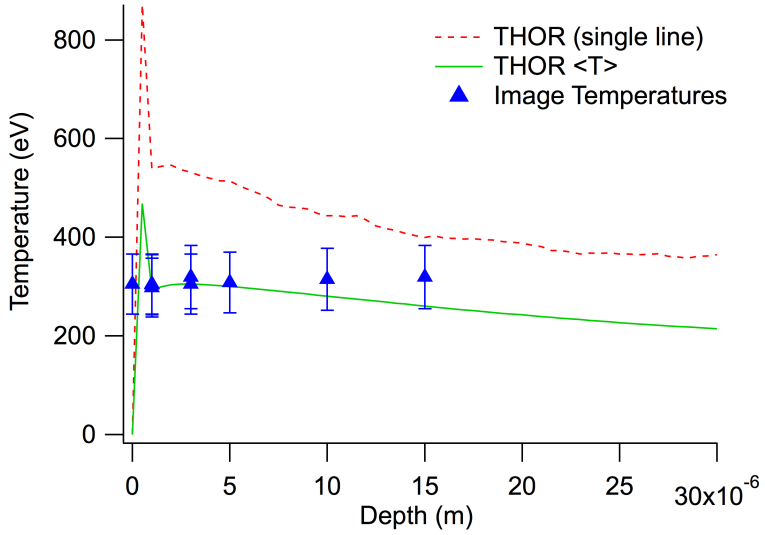

Figure 4.10: Temperature calculated by THOR for lineouts of a single pixel along the laser axis, and for an average over a radius of 15μm, with target depth, at t=3ps (laser incident at x=0). This is compared to temperatures derived from experimental data.

Figure 4.10 shows lineouts taken through the centre of the simulated target along the laser direction (z-axis), coincident with effective laser position compared to temperatures shown in Figure 4.9. The THOR simulation shows target temperatures fall by 31% between depths of 2μm and 30μm, in broad agreement with published data [15, 17, 108, 109]. The green trace labelled $< T >$, is the temperature averaged over 30μm at the centre of the simulated target for comparison to temperatures derived from imager data which has an average diameter of approximately 30μm. The calculated temperatures shows reasonable agreement with the averaged simulation. For depths of 5μm or less, temperatures calculated from experimental data agree with the THOR temperatures. For depths of 10μm and 15μm, the experimental data implies that temperatures are higher than indicated by simulation.

4.5 Estimation of image diameter from simulation

Figure 4.11(a) shows a THOR simulation of temperature inside a 30μm thick CH target with an initial electron divergence angle of 50°, absorption fraction $\eta = 0.3$, and a source of 7μm diameter to emulate experimental conditions as closely as possible. It shows that temperatures of up to 1.2keV are reached near the laser-target interaction, and that the highest temperatures are seen along the z-axis. The incident laser intensity is $5 \times 10^{20}\mathrm{Wcm}^{-2}$ in a 7μm spot diameter, with duration of 1ps, striking centrally on the left hand boundary. The simulation box is extended to a total thickness of 30μm despite measurements existing up to 15μm. This allows high energy electrons to propagate away from the region of interest, reducing the potential effects of refluxing.

Lineouts taken across the simulation vertically (indicated by dashed lines on Figure 4.11(a)) at 5μm intervals from 1μm to 30μm depth are shown in Figure 4.11(b). These plots show that with increasing depth the peak temperature drops and the temperature profile broadens.

Figure 4.11 shows that for regions close to the interaction the profile is much steeper and narrower, than for greater depths where it's maximum drops and the

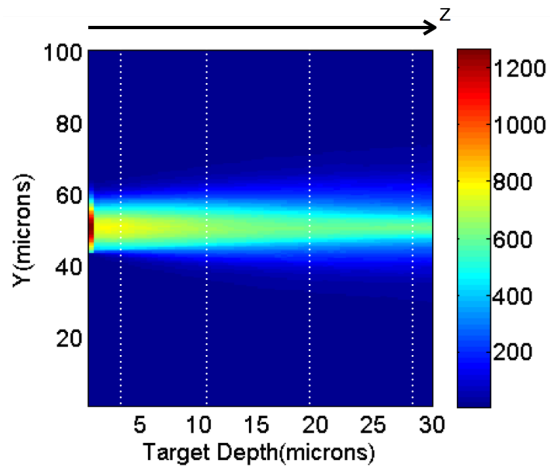

(a)

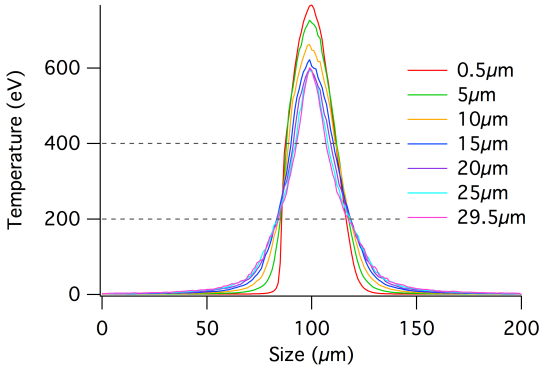

(b)

Figure 4.11: (a) Simulation of background temperature (eV) in a CH slab of 30μm thickness. Incident laser intensity 5×10^{20}Wcm^{-2} in a 7μm spot in 1ps, striking centrally on the left hand boundary (b) Lineouts taken across simulations (shown by vertical lines in (a)) illustrate that the peak of the temperature profile decreases and the temperature profile broadens with increasing depth into the target.

profile broadens.

Considering the beam profile at 400eV (shown by horizontal line), it can be seen that the width of the temperature profile is expected to be 10μm for a depth of 1μm, and 4.5μm for a depth of 15μm. The diameter of the 400eV region of material becomes smaller for increasing depth.

The rate at which this region becomes smaller or larger with depth is defined as an angle of convergence or indeed, divergence θ_{image}. All angles described here are half angles as illustrated in Figure 4.1(b).

The emission of the He-β line occurs over a range of temperatures and so it is worth assessing the impact of a range of temperatures to track x-ray emission.

Figure 4.12 shows the diameter of other temperature profiles with increasing target depth. In general the angle of convergence θ_{image} of the contours decreases with material temperature. For example, the 500eV contour is seen to fall away to zero much faster than the 200eV contour. As in Figure 4.11, material at 200eV shows little change in diameter up to depths of 15μm. Temperatures below 200eV show a profile that increases in diameter with target depth.

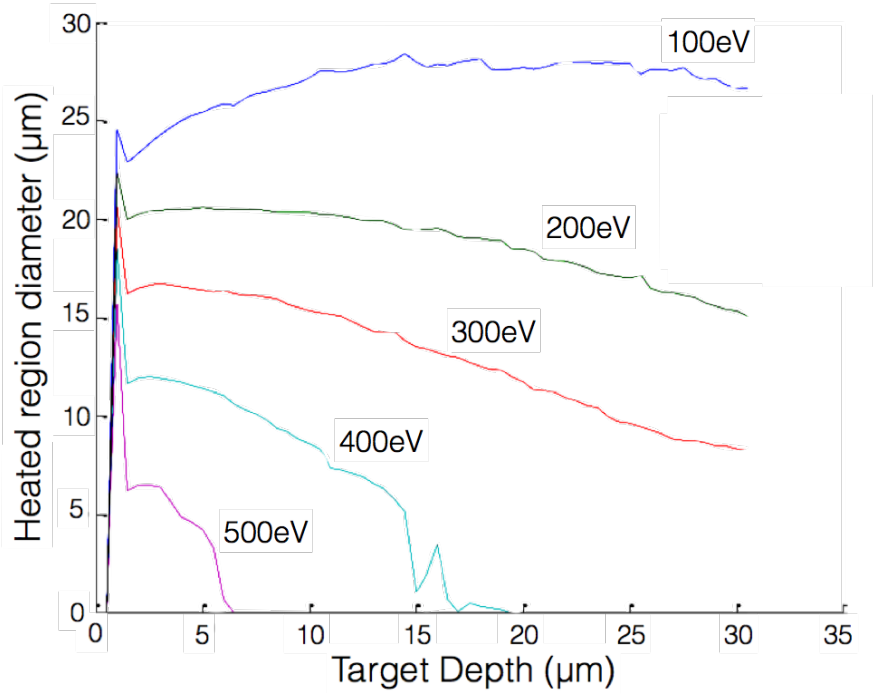

Figure 4.12: Tracking of temperature contours with increasing depth into solid density CH. This simulation emulates a pulse of 5×10^{20}Wcm^2, and an absorption fraction of $\eta = 0.3$ and a spot diameter of 7um. Each point represents the full diameter of the material contour at the specified temperature.

The temperature chosen to represent the emission of the Al He-β line is 400eV. The diameter of material at 400eV is close to zero at around 15μm depth. Regions of 200eV and 300eV material are seen to extend to the full length of the target.

To increase the accuracy of this estimate, the relative contribution of each temperature could be incorporated by using a weighting function. In the following,

simulation of the x-ray image diameter is carried out by tracking of 400eV material.

4.6 Constraining Fast Electron Parameters

THOR injects a fast electron population over a gaussian profile, with a fast electron temperature of 3.2MeV in agreement with the temperature measured by an electron spectrometer on this experiment [110].

As part of the input for THOR simulations, a fast electron divergence angle is specified by the user, and determines the angular distribution of the fast electrons are injected into the target. The transport of electrons into the target and the heating profile is directly affected by the divergence chosen. A generally accepted range for the fast electron beam divergence is between $50° - 80°$ half angle [19]. THOR simulations were done for divergence half angles of 20°, 50° and 80°, and used to observe changes in the diameter of material at 400eV. For a description of THOR, refer to Section 2.12

The diameter over which electrons are injected into the target, and the fraction of energy absorbed by the laser into the target are specified by the user. The source size is commonly estimated from the diameter of the laser spot for the experiment being modelled (in this case 7μm diameter) and the absorption fraction is generally thought to be $\eta = 0.3$.

This kind of judgement for initial code setup is typical for detailed modelling of intense laser interaction physics. The divergence angle of the injected electrons, the source size and absorbed fraction of laser energy each have high impact on the target heating profile. Each of these parameters is considered to obtain a set of conditions closest to reproducing the data by tracking material at 400eV. The rate at which the areas of heated material become smaller (or larger) will be described as an angle of convergence (or divergence). In this way, values for these key parameters are inferred by comparison with detailed experimental results. A short summary of the resulting configuration that best fits the experimental data in shown in Section 4.6.4.

4.6.1 Effects of code injection angle

For the three chosen divergence angles 20°, 50° and 80°, the temperature profile is visibly modified, as is shown in Figure 4.13. Figure 4.13 shows simulations of

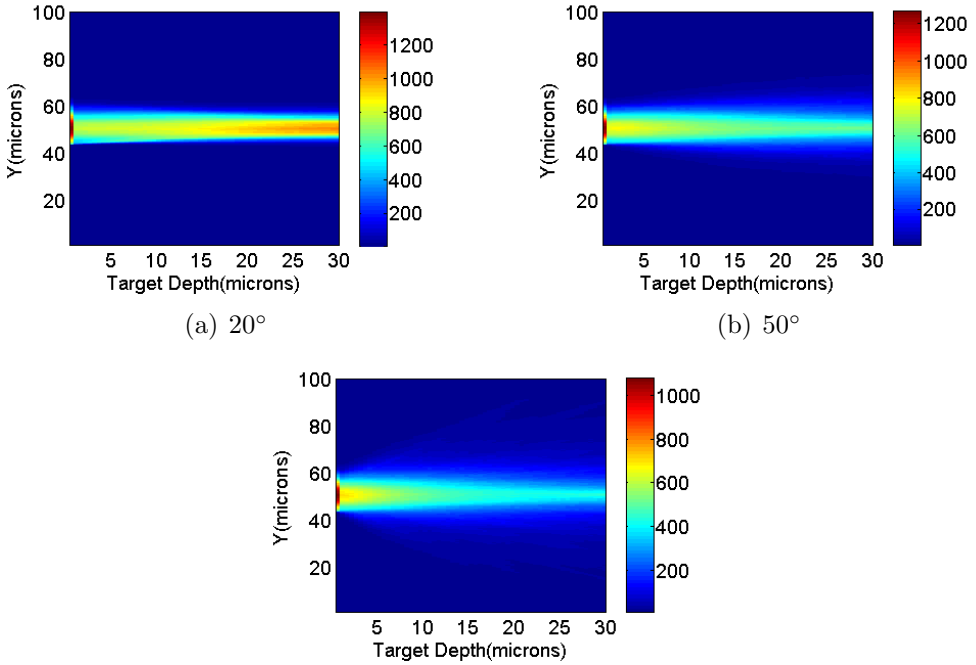

(a) 20° (b) 50°

(c) 80°

Figure 4.13: THOR simulation of target temperature profile for three available injected divergence angles, source diameter 7μm, and absorption fraction, $\eta = 0.3$.

target temperature profiles due to changing injected divergence angle. The simulated laser source is incident from the left hand side of each. Maximum temperatures of 1400eV, 1200eV and 1000eV close to the interaction are seen in each of the 20°, 50° and 80° cases respectively. The maximum temperature drops with increasing divergence angle. For an input half angle of 20°, relatively little change in heated region diameter is seen within the target. It also shows that the target is hotter at the rear than at the front (left) surface. The 50° and 80° cases show a narrowing of heated material for increasing target depth.

Figure 4.14 shows how material at 400eV changes with increasing depth into the target. For an injection angle of 20°, the angle of convergence is 15°. This convergence increases to 30° for the 80° simulation for the same material temperature

of 400eV. Material at 400eV is seen to converge more rapidly for higher injection angles.

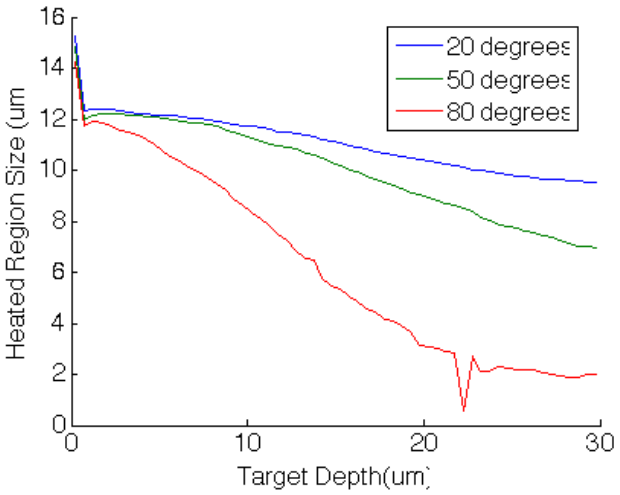

Figure 4.14: Diameter of 400eV material with target depth for injected fast electron divergence half angles of 20°, 50° and 80°.

Figure 4.15 shows a plot of the angle of convergence for different injected divergence angles and temperatures. Simulated points are fitted with a power law to compare how material heating is affected.

Figure 4.15 shows that the heated region converges more rapidly with increasing fast electron injection angle. An attempt is made to match the convergence angle seen in experimental data, to the convergence angle of 400eV material in simulation. Experimental data shows a convergence of 25°. To match this with simulation of 400eV material, a fit is applied to the convergence angles in Figure 4.15. This shows that for the diameter of material to converge as the data does, an input electron divergence angles of 70°±10° is needed. If the 300eV and 500eV contours in Figure 4.15 are considered the required electron injection angle to achieve a convergence angle of 25° is modified to >80° and 55° respectively.

For the 20° case of Figure 4.13(a), the temperature of the target along the central axis increases towards the rear surface at around 30μm. The cause of this is uncertain, however if the injection angle of the electrons is low, the self-generated magnetic field can be strong enough to pinch the electron beam deeper into the

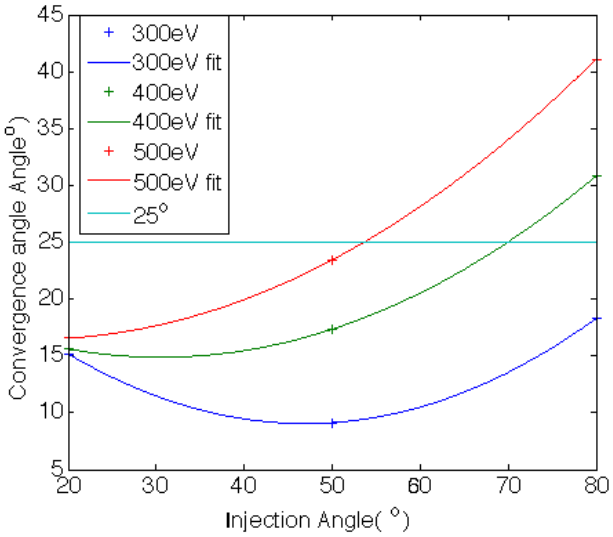

Figure 4.15: Relationship between convergence and divergence angle for temperatures of 300eV, 400eV and 500eV.

target.

4.6.1.1 Magnetic field and divergence angle

To gain an overview of the magnetic fields inside the solid density CH, additional simulations were done using Zephyros to supplement the THOR work. For a description of Zephyros, refer to Section 2.11. Figure 4.16 shows the magnetic fields present a Zephyros simulation equivalent to that of Figure 4.13(a) and 4.13(b). For a CH slab of 30μm thickness, with an input divergence angle 20° and 50°, and a laser of 5×10^{20}Wcm^{-2} in a 7μm spot in 1ps, the magnetic field ($|\mathbf{B}|$) and temperature (T_b) is shown in Figure 4.16.

Figure 4.16(a) shows that magnetic field peaks at approximately 900T around the edges of the heated region of the target. The existence of this azimuthal magnetic field extends to the depth of the target simulation. Figure 4.16(c) shows that the temperature follows a similar pattern and regions of hot material extend to 30μm. Figure 4.16(b) shows that a different magnetic field profile exists when the divergence angle is increased to 50°. In the region where the beam radius remains at it's smallest, until depths of approximately 12μm, the magnetic field is seen to

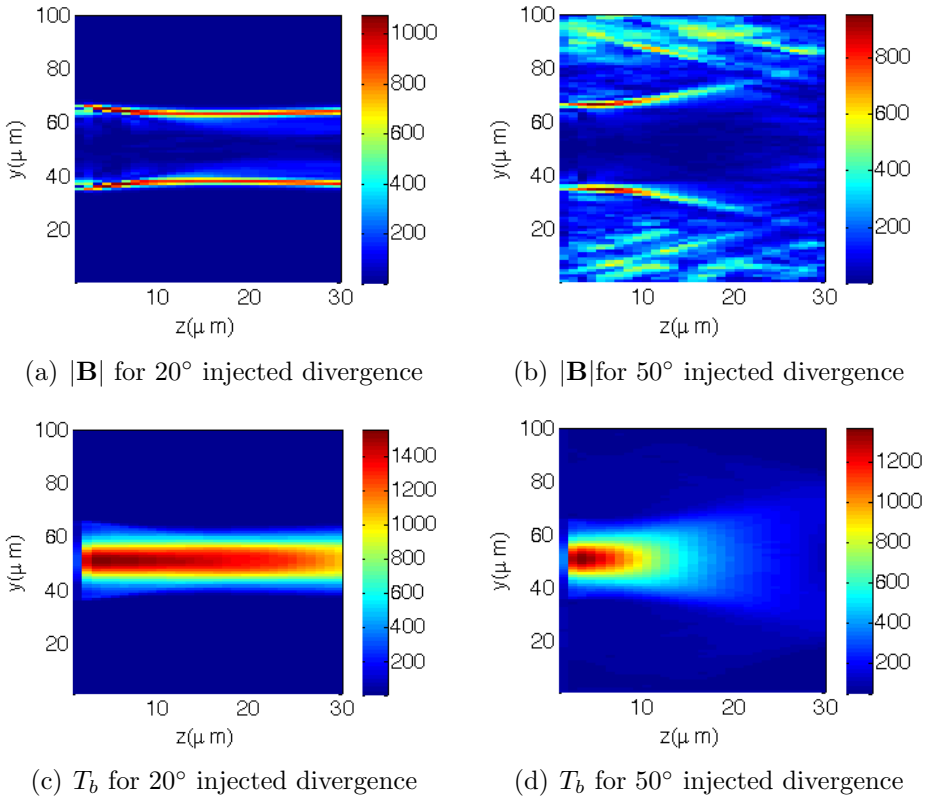

(a) $|\mathbf{B}|$ for 20° injected divergence

(b) $|\mathbf{B}|$for 50° injected divergence

(c) T_b for 20° injected divergence

(d) T_b for 50° injected divergence

Figure 4.16: Simulation of magnetic field $|\mathbf{B}|$ by Zephyros, viewed (a) with the laser incident from the left at $y = 50$, $z = 0$, and (b) with the laser incident into the page, and (c) material temperature as calculated by Zephyros for a $5{\times}10^{20} Wcm^{-2}$ laser in a 7μm spot in 1ps, incident on a 30μm CH slab target with an input electron angular divergence of 20°.

be strongest around the edge of the beam. At this depth the temperature profile shown in Figure 4.16(d) is seen to rapidly spread, and the magnetic field intensity rapidly diminishes, producing no collimating effect at all.

The generation of an azimuthal magnetic field due to the propagation of an electron beam is well documented in laser-solid interactions, and is discussed further in Section 4.8 [54, 55, 111]. A similar field will be present in the THOR simulation of Figure 4.13, this will act to pinch the fast electron beam, preventing the divergence of the electrons causing intense heating at greater depths into the target.

4.6.1.2 Summary

In the simulations shown, it has been shown that a divergence angle of 70°±10° is needed to match the angular convergence of experimental data. For small injected divergence half angles, the target heating is seen to extend further into the target. Supplementary simulations imply that the self-generated magnetic fields of a narrow electron beam propagating through the target may be a contributing factor. Although the converging characteristic of the experimental data has been reproduced, the diameter of the images does not agree with the experimental result. Simulated sources seen here are smaller than is seen in measurements, implying that an input source broader than the initial diameter of 7μm is needed.

4.6.2 Effect of source size

For depths of the order of 1μm into the target, experimental data shows that the He-β line is emitted from a region approximately 25μm in diameter. This region of hot plasma close to the front surface is much larger than the initial laser spot of 7μm. Refraction of the laser beam in the front surface plasma has been shown for long scalelength experiments [21]. This is a possible candidate for cause of energy deposition and heating over an area much larger than the laser spot [21]. Further the laser absorption region is some distance from the solid target. THOR and Zephyros simulations in Figure 4.17 show that for a range of input source sizes, the area over which the target is heated at depths close to the front surface is consistently larger than the diameter of the source. THOR simulations model only the target, and do not model the front surface plasma that exists outside of the simulation boundary which produces refraction effects.

Extending the diameter of the simulated source from 7μm to 15μm reduces the energy density at the source region and lower temperatures result. The maximum target temperature decreases from around 1.5keV (average 900eV) for a 7μm source diameter to around 400eV (average 240eV) for a 15μm diameter. The maximum temperatures in the 15μm source case are much more consistent with tempera-

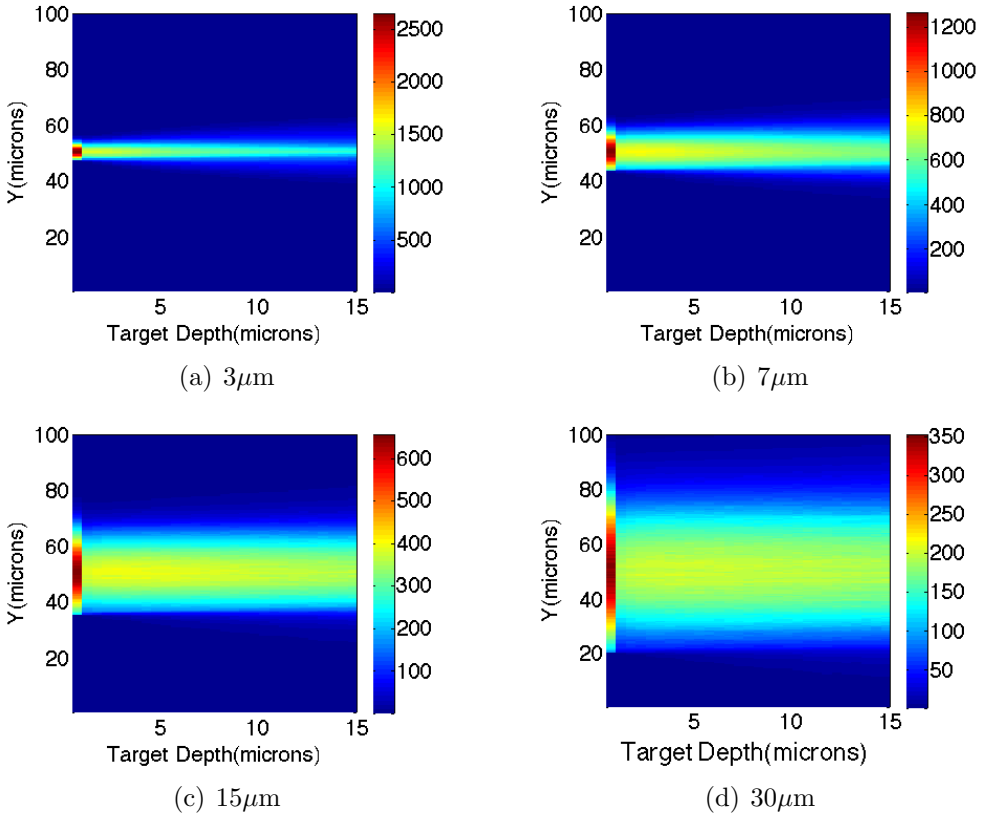

(a) 3μm (b) 7μm

(c) 15μm (d) 30μm

Figure 4.17: THOR simulation of target temperature profile for a range of source sizes. Regions of 400eV are indicated as (a) 7μm, (b) 14μm, (c) 30μm and (d) shows no 400 eV material at all. Experimental data indicates sources of approximately 25μm, which is best replicated by (c) where a source approaching 30μm is indicated.

tures seen by experiment. However, the region of material at 400eV extends a few micrometres into the target. In comparison, data suggests that it extends to approximately 15μm. With the divergence angle now estimated to be $\approx 65°$, and the image diameter of 25μm, the remaining parameter is the laser absorption fraction. The fraction of laser light absorbed is thought to vary between 0.1 and 0.3, and the latter has been applied so far.

4.6.3 Effect of absorption fraction

The way that energy is injected into the simulation is through an assumed laser-target coupling efficiency, η. The absorption fraction used was increased from $\eta = 0.3$ to $\eta = 0.5$, and the result is presented in Figure 4.18.

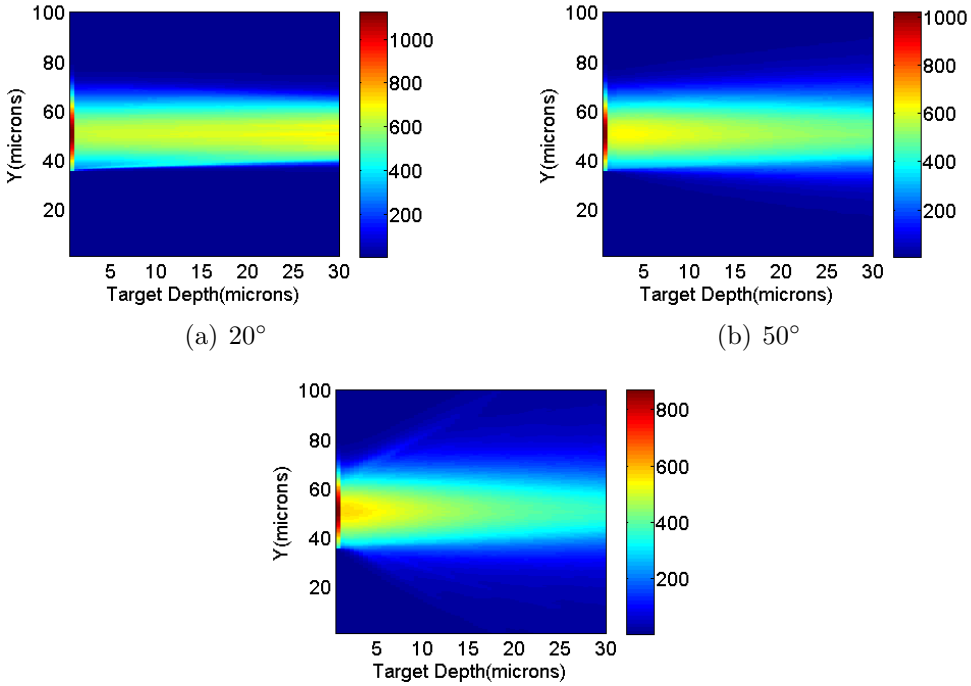

(a) 20°

(b) 50°

(c) 80°

Figure 4.18: THOR simulation of target temperature profile for injected divergence angles of 20°, 50° and 80° with an increased absorption fraction, $\eta = 0.5$.

Figure 4.18 shows the target temperature resulting from the change of absorption fraction from 0.3 to 0.5 for injected divergence angles of 20°, 50° and 80°. The increase in absorption fraction for these simulations results in an increase in target temperature, such that extended regions of 400eV are seen in Figure 4.18(c) for a 15μm source and an 80° injected divergence angle, which now shows the best match to the experimental data. The 80° was used here as it represents as it is the closest to the previously inferred estimate of fast electron divergence angle.

This simulation shows maximum temperatures of 800eV. This is beyond the upper temperature threshold for the emission of Al He-β. The most intensely heated material is in general on the target surface normal axis, and at the same position as the laser strikes the target front surface. For maximum temperatures around 800eV in this region, emission would be seen to drop giving an explanation for data with a ring like appearance as in Figure 4.2(a).

4.6.4 Summary

If the extent of material at 400eV is taken to be representative of the image diameter, then the source must have a diameter around 15μm, with an electron injection angle 70°±10° to reproduce the convergence angle of the data. However, using a simulated source of 7μm, diameter did not replicate the diameter of the emission. Extension of the simulated source from 7μm to a 15μm diameter, gave a good match to experimental data. This resulted in cooler target temperatures and regions of 400eV extended less than 7μm into the target. Experimental data suggests that this temperature extends to 15μm. Increasing the absorption fraction from 0.3 to 0.5 achieved a better match to experimental data. A simulated source diameter of 15μm produces an x-ray image diameters approaching 30μm, and a divergence angle of 80° replicates the converging characteristics of the x-ray data. The increased absorption fraction η=0.5 ensures that temperatures needed for intense emission extend to depths of emission implied experimentally.

Under these conditions, the maximum temperature of the target is around 800eV. This extends beyond the upper threshold for He-β emission meaning that observation of structure in the data is caused by regions of material >700eV, is plausible or even expected. The magnetic field generated in the target appear to have a much greater collimating effect for low divergence angles. For an injected divergence angle of 20°, an intense magnetic field is seen to surround the heated region to the extent of the simulation at a depth of 30μm. For a beam of 50° this is shown to have a much lesser effect, and the collimating effect disappears at approximately 12μm. The target temperature also becomes much broader and cooler at this point.

In this investigation the electron temperature of 3.2MeV has been kept constant, although it is accepted that this will also have an impact on the target heating profile results produced by the THOR code. The limitation imposed by the use of a single temperature to represent x-ray emission from a distribution of temperatures is also noted. However, this describes a method by which detailed spectroscopic measurements can be used to constrain input parameters. Investigation of the effects

of effect of the resistivity model used remains for further work. Although not all collisional radiative models as have been used here will agree, good agreement in this case has been seen between the PrismSPECT and FLYCHK models with regards to spectral line positions [61, 112].

4.7 Simulation of spectroscopic emission

Simulation of the laser-solid interaction using the hybrid-PIC code Zephyros [67] produces 3D target temperature data. By taking 2D slices through this data at different target depths, 2D maps of how the temperature is distributed spatially at varying depth into the target are produced. The change in spectral line emission with temperature has been calculated using the collisional radiative model PrismSPECT and is discussed in Section 2.10.2. Knowledge of how the emission of a spectral line changes with temperature, allows simulated 2D temperature maps from Zephyros to be converted into 2D maps of Al He-β line emission. This analysis takes the 2D temperatures profiles at known depths into the target, and calculates the material ionisation balance. The flux of Al He-β emitted is calculated for each point to create synthetic images of line emission. The use of PrismSPECT indicates that the use of the optically thin approximation is valid under these conditions.

The target setup used in this case is a 30μm thick slab of homogeneous cold CH which is 100μm $\times$ 100μm, and each cell has 1μm dimensions. Simulations are performed with an input fast electron divergence angle of 50°. The output timestep of the code is 100fs, and for all simulations shown here the maximum time of 3ps is used in line with simulations in previous sections.

The geometry of the simulation is shown in Figure 4.19. By taking an x-y slice (horizontal and vertical axes) through the target at specific z positions (laser direction), it is possible to create 2D images of the target for a specified depth with a resolution of 0.5μm. Each slice represents a specific position in the simulated target.

Figure 4.20 shows 2D slices taken from a Zephyros simulation showing temperatures from a slice at 5μm depth (4.20(a)) and through the centre of the target

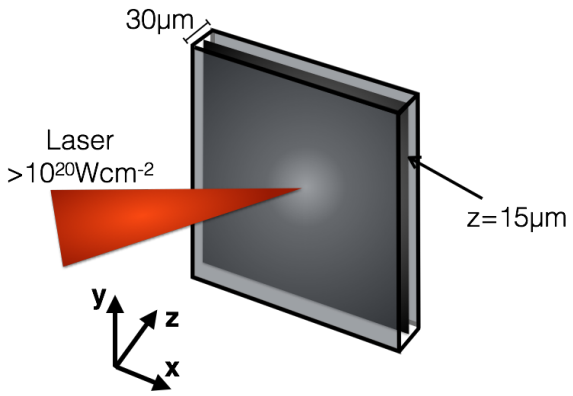

Figure 4.19: Sketch of the Zephyros simulation setup showing laser incident on target, highlighting a layer placed at 15μm within a total slab thickness of 30μm.

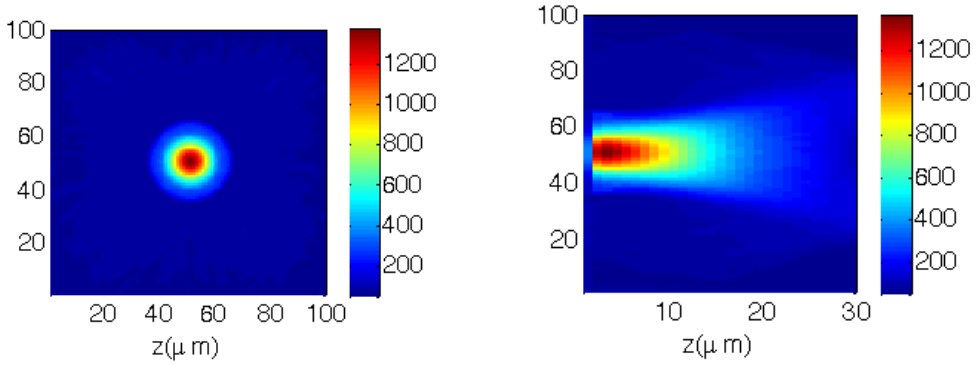

(a) Slice taken at 5μm depth in z, showing target temperature in eV.

(b) Slice taken at x = 50μm showing temperature in eV.

Figure 4.20: 2D temperature plots from Zephyros simulation of $5\times10^{20}Wcm^{-2}$ laser pulse in 10μm aluminium.

at x=50μm showing the temperature change with depth into the target (4.20(b)). Images shown in Figure 4.20 represent the background electron temperature in the target. The 2D temperature profiles shown in Figure 4.20 are used to produce the anticipated emission of the Al He-β and Ly-β shown in Figure 4.21. The dependence of line emission on material temperature for the Al He-β and Ly-β spectral lines is shown in Section 2.10.2.

Images in Figure 4.21 are a simulated equivalent to images of the He-β recorded by the 2D imaging spectrometer. The simulated emission of the He-β line is shown in Figures 4.21(a)−4.21(d), and the Ly-β emission shown in Figures 4.21(e)−4.21(h). For images in Figure 4.21(a) and 4.21(b), an annular emission profile results from

the temperature sensitivity of the Al ionisation state. If the target temperature is high, the ionisation stage of the Al is too high and a weak emission is seen. In this case, peak temperatures and weak emission occur at the image centres. In contrast, if the target is cool the ionisation stage of Al is too low and emission of He-β is weak. This occurs here at the edges. In regions where the population of the Al^{11+} is maximised, the He-β emission is strongest, and the result is an annular image structure. As the target cools with increasing depth into the target, the central region of the image cools and becomes filled with He-β emission and the annular structure fades. By the time depths of 15μm are reached, simulations predict a peaked emission profile.

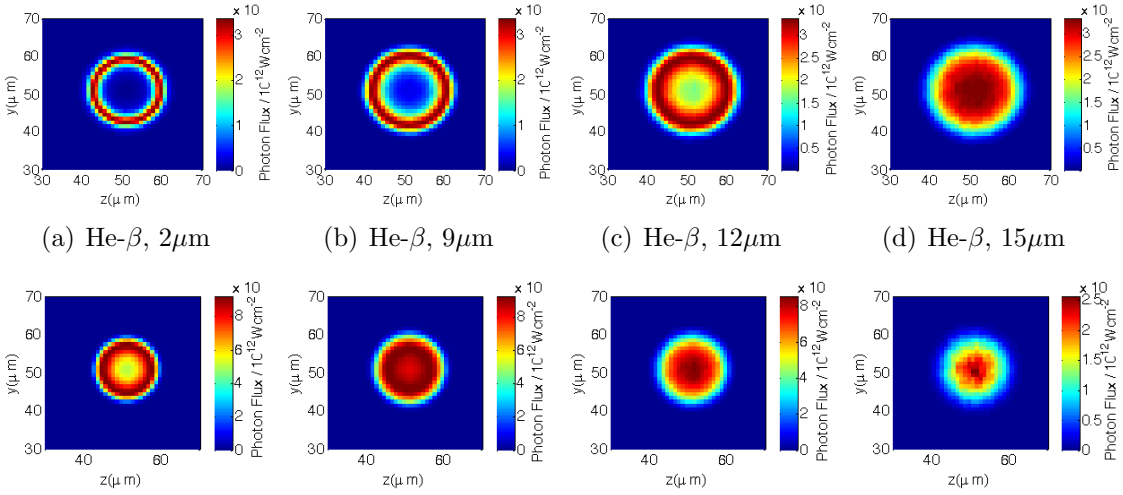

(a) He-β, 2μm (b) He-β, 9μm (c) He-β, 12μm (d) He-β, 15μm

(e) Ly-β, 2μm (f) Ly-β, 9μm (g) Ly-β, 12μm (h) Ly-β, 15μm

Figure 4.21: The simulated images represent Figure 4.20 as a spatially resolved x-ray emission flux.

The images in Figure 4.21(e)−4.21(h) represent the emission from the target temperature profile in Figure 4.20, for the emission of the Ly-β spectral line. For this transition, higher temperatures are needed to provide significant populations of the Al^{12+} ion. The peak emission of Ly-β is a maximum for a higher temperature than for the He-β, and higher levels of emission is seen closer to the centre of the image. In the first Ly-β image, a region of lower emission is seen in the centre due to the over ionisation of Al, but not so much that no emission is seen at all. As the

temperature of the target cools with target depth, the Ly-β emission in the target centre is seen to rise and the annular structure becomes less apparent. The drop in emission due to material being cool around the edges of the target occurs at a higher temperature for Ly-β than the He-β emission. Therefore the overall diameter of the Ly-β images in Figures 4.21(e)−4.21(h) is smaller than for the He-β images. Therefore the Ly-β can be used to observe higher material temperatures.

In the case of the He-β, the region of maximum emission moves from the edges of the images to the centre as the target cools. For depths of 2μm, there is maximum emission in the ring structure as the temperature is optimum and as the target cools, the emission from the ring becomes diffuse. Eventually, at depths of 15μm the emission becomes peaked in the centre as that is now the location of the optimum emission temperature. For the Ly-β, the emission is seen to follow similar trends, except that they occur for higher temperatures and therefore at shallower depths than the He-β. The Ly-β line is slightly heightened around the edges of the image to begin with at depths $< 9\mu m$, and beyond this becomes peaked around the laser axis. As the temperature cools further this peak becomes more pronounced as the region of material at optimum temperature decreases in diameter.

4.8 Effect of the buried layer on fast electron transport

The presence of the buried layer in the experiment is widely regarded to have impact on the fast electron transport, by the introduction of a step change in Z and n_e at the interface [113–115]. The resistive generation of magnetic fields due to the flow of a beam of fast electrons is described in Section 2.8.2 by (2.16) [53, 56, 116]. The $(\nabla\eta) \times \mathbf{j_f}$ term of (2.16), generates a magnetic field that pushes electrons towards regions of high resistivity η. Gradients in resistivity have been used to produce magnetic fields that can collimate fast electrons [54]. The remaining term $\eta\nabla \times \mathbf{j_f}$, generates a magnetic field that pushes electrons towards regions of high $\mathbf{j_f}$ [55]. Both mechanisms depend upon the resistivity η. The Spitzer model for material

resistivity, η_s [54, 117, 118] (not to be confused with the absorption efficiency as used in the previous section η) is,

$$\eta_s = \frac{Ze^2 m_e^{1/2} \ell n\Lambda}{2\pi\epsilon_0 (k_b T_e)^{3/2}} \tag{4.4}$$

It can be seen that $\eta_s \propto Z$ and also $\eta_s \propto T_e^{-3/2}$. Ohm's law also states that $\mathbf{E} = \eta_s ne\mathbf{v}$, and $\mathbf{E} \propto \eta_s \propto Z$. The origin of the magnetic field is the step change in the electric field at the interface between the target material and the layer given by $\Delta\mathbf{E} = (\eta_{s,1} - \eta_{s,2})\mathbf{j_f} sin\theta$, where θ is the divergence angle of the fast electrons. Magnetic fields generated on the front surface of a Cu layer in CH target has been observed to decrease with buried layer depth and with laser intensity [113]. The electric field expressed in Ohm's law has a dependence on $\mathbf{j_f}$. Thus for regions of intense $\mathbf{j_f}$ the electric field will be highest, and the relationship between $\mathbf{E}$ and $\mathbf{B}$ implies that these will be the region of strong magnetic field generation.

The aluminium spectroscopic layer in the buried layer experiments presented is 0.1μm thick. The layer thickness was kept to a minimum compromising between the material needed for bright emission, accurate representation of target thickness, and the impact on electron transport. As the layer is thin, it has been assumed in previous sections that the temperature profile in the CH immediately prior to the layer represents temperatures that present in the layer itself. However it is known that the introduction of a layer of an increased Z will affect the transport of fast electrons and consequently the target heating.

To quantify the effects of the buried layer, two simulations were completed using Zephyros. In the following simulations, a 1μm buried layer has been inserted into a CH target at depths of 2μm and 10μm. Due to the computational expense of simulating a 0.1μm layer as was used in the experiment, a 1μm was used here. The magnetic fields and target heating profiles resulting from a laser intensity of $5 \times 10^{20} Wcm^{-2}$ incident on a buried layer target are shown in Figure 4.22.

Figure 4.22 shows that the magnetic fields generated at 2.5μm in Figure 4.22(a) are more intense than for 10μm in Figure 4.22(c), and in both cases, the field only

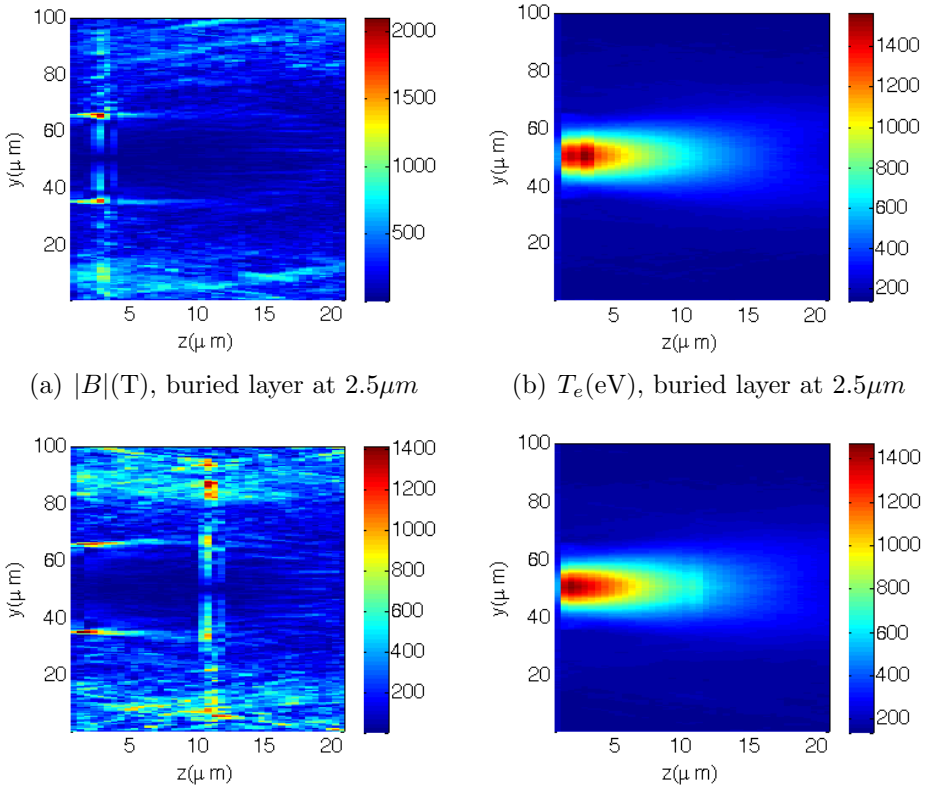

(a) $|B|$(T), buried layer at $2.5\mu m$ (b) T_e(eV), buried layer at $2.5\mu m$

(c) $|B|$(T), buried layer at $10\mu m$ (d) T_e(eV), buried layer at $10\mu m$

Figure 4.22: The temperature and magnetic fields for simulations of a 0.1μm buried Al layer at 2μm and 10μm depths into the target. These simulations represent a snapshot taken at 3ps after the peak of the laser pulse.

extends as far as the buried layer itself. The magnetic field also appears to be at it's most intense at the interface. The temperature profiles shown in Figures 4.22(b) and 4.22(d) show the effect of these layers on the temperature profile.

To assess the effect of the buried layer on the temperature of the target at the buried layer interface, cross sections are taken along the y axis inside the buried layer and in the material immediately before it by $0.5\mu m$. For example, Figure 4.23(a) shows cross sections taken at 1.5μm and 2.5μm, where the buried layer itself extends from $2-3\mu$m. The same method is applied to Figure 4.23(b), where the buried layer is positioned at 10μm.

In Figure 4.23(a), the buried layer increases the maximum temperature by approximately 110eV (1451 to 1561 eV), and no significant change in profile diameter is seen. Figure 4.23(b) shows that there is a change in maximum temperature of ap-

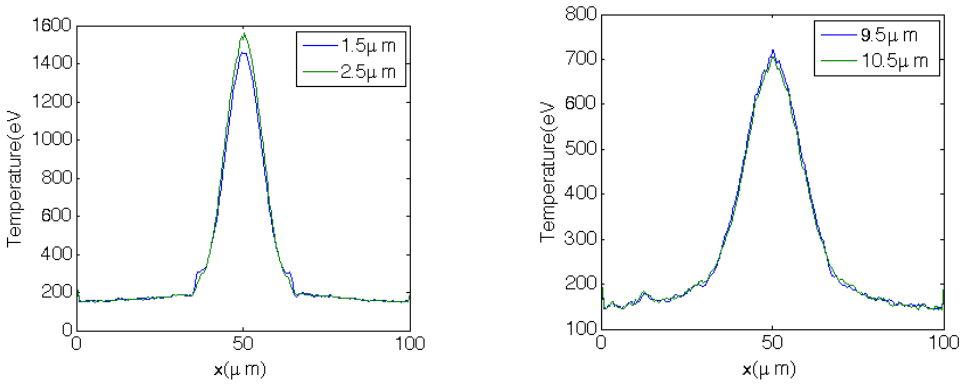

(a) Buried layer at 2μm depth (b) Buried layer at 10μm depth

Figure 4.23: Temperature profile at a time of 3ps, of material just before and inside the buried layer for (a) 2μm depth and (b) 10μm depth.

proximately 14eV (705 to 719eV), and that there is no visible change in the diameter of the temperature profile.

In Figure 4.23(a) the buried layer is close to the interaction and a much larger change in maximum temperature between the layer and the preceding CH is seen. This indicates that the closer to the front surface that the buried layer is placed, the greater the effect on the resulting thermal transport. A change of this size could have an impact on the spectral emission due to the change in ionisation that this causes. For Figure 4.23(b), a smaller change is seen which has less of an impact on the population distribution of the ions. The overall diameter of the temperature profile is not seen to change significantly.

The magnetic field and temperature profile evolve with time, and therefore the effects of the buried layer on temperature profile and magnetic field is time dependent. For the buried layer positioned at 2μm, the change in the magnetic field (T) and target temperature (eV) with the simulation time is shown in Figure 4.24. Figure 4.24 shows the magnetic field and temperature for times of 100fs (Figure 4.24(a) and 4.24(d)), at the end of the laser pulse at 600fs (Figures 4.24(b) and 4.24(e)), and finally at 3ps in Figures 4.24(c) and 4.24(f). Time development is presented from left to right for 100fs, 600fs and 3ps, and the laser is always incident on the centre of the left hand boundary. Axes and colour scales are normalised to

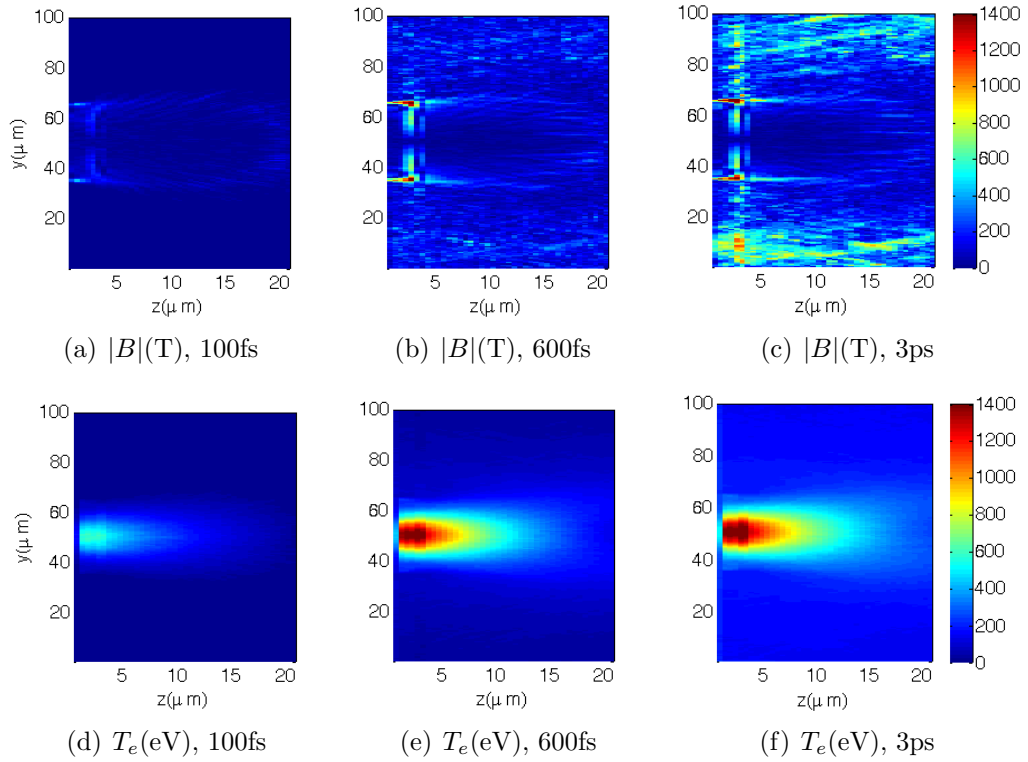

(a) $|B|$(T), 100fs (b) $|B|$(T), 600fs (c) $|B|$(T), 3ps

(d) T_e(eV), 100fs (e) T_e(eV), 600fs (f) T_e(eV), 3ps

Figure 4.24: The evolution of magnetic field $|B|$ and temperature T_e for simulation times of 100fs, 600fs (pulse end) and 3ps.

1400eV for all temperatures and 1400T all magnetic fields. This shows that the magnetic field and temperature grows with time, reaching their maxima of 1400T and 1400eV respectively at 3ps. Although the emission of a He-β photon is rapid and the number of fast electrons is seen to tail off quickly after the laser is turned off, the magnetic fields and temperatures are sustained at least until 3ps. The THOR simulations of target temperature in previous sections are also run to 3ps. The simulations presented are to assess the effect of the buried layer to the energy transport in the target. The effect is smaller than the experimental error for buried layer placed at 10μm, but the change in temperature seen for the layer placed at 2μm is double the error value, at 100eV.

4.9 Toroidal Crystal Spectrometer

The high dispersion toroidal spectrometer (HDTS) as outlined in Section 3.3.3 has been used here to spectrally resolve the emission from the buried layer. The role of the HDTS in this work is to provide supplementary data, specifically the shape and width of the He-β emission line. In conjunction with PrismSPECT [60] the spectral linewidth is used to provide an estimate of plasma density, and simultaneously provide additional imaging in 1D. It is used to give accurate linewidth data to compare with the spectral window of the crystal, and to determine the effect of the spectral lineshape on measurements. The lineshape can also give insight into the atomic processes in the plasma. Typical data collected from the toroidal crystal spectrometer is given in Figure 4.25.

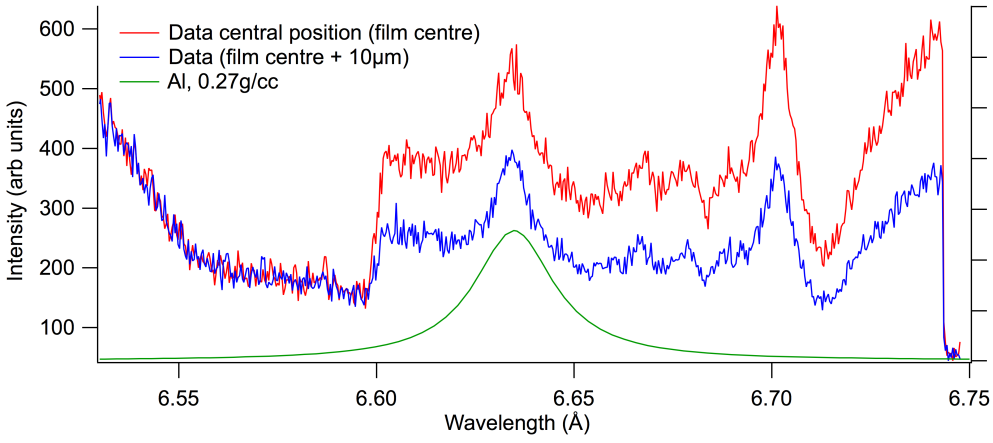

(a)

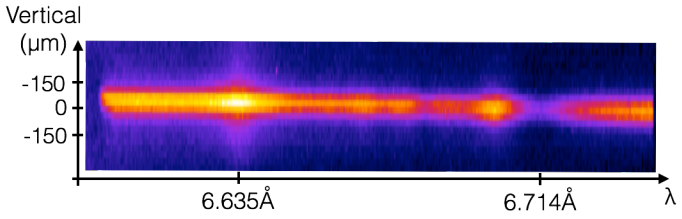

(b)

Figure 4.25: (a) Spectrum obtained by the toroidal spectrometer for a laser intensity of $3\times10^{20}Wcm^{-2}$ incident onto a 10μm aluminium foil. Two spectrum shown are for the centre of the plasma (red) and 10μm above this (blue). The Al He-β spectral line is seen at 6.635Å. Also note the K-edge for silicon at 6.714Å in close proximity to the He-β (b) X-ray film.

Figure 4.25(a) shows the spectrum with the aluminium He-β spectral line at 6.635Å. Also shown is the K-edge for the Si component of the quartz crystal. Shown in green is a simulated spectrum produced by PrismSPECT for the emission from aluminium. All Al spectra show the He-β resonance line features as in the data. The steep edge seen at 6.59Å appears to be the crystal edge.

Figure 4.25(b) shows an image of the x-ray data as it appears on the x-ray film, from a 20μm Al foil. The vertical direction is defined as the focussing axis of the crystal and defines the 1D imaging direction. If the crystal is in focus, then the width of the spectrum in this direction represents the source size of the plasma with a magnification of approximately 5. The direction denoted λ, is the dispersion direction of the crystal. The x-ray spectrum presented in Figure 4.25(a) (red) was taken along this axis, in the centre of the image. The other blue trace, is the spectrum taken at approximately 10μm, which represents the emission from a separate part of the plasma source. The blue spectrum is less intense overall and shows a slightly narrower profile of the Al He-β line. The x-ray film resolution and magnification results in a spatial resolution of $\approx 5\mu$m at the plasma.

The plasma density is calculated from the spectral linewidth in conjunction with collisional radiative spectral modelling with PrismSPECT. By modelling the spectral linewidth over a range of densities, the relationship between the spectral linewidth and the plasma density is defined, given in Figure 4.26.

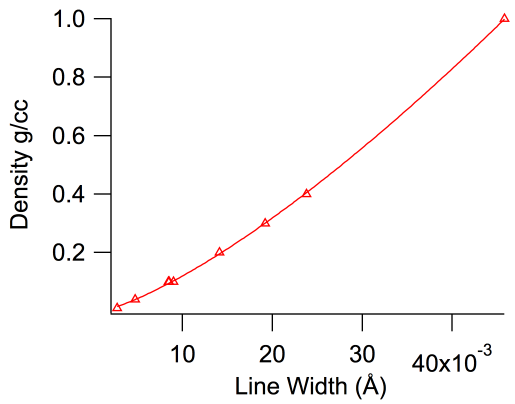

Figure 4.26: Relationship between plasma density and He-β spectral linewidth for a solid density Al foil of 20μm thickness.

Sampling of the spectral linewidth at different vertical positions across the target, and fitting to the spectral data to obtain the width of the line allows the calculation of plasma density. For the spectrum such as that presented in Figure 4.25(a) where the linewidth is 14mÅ , the plasma electron density is seen to be approximately $5 \times 10^{22}\text{cm}^{-3}$. The variation in calculated plasma density across the plasma is shown in Figure 4.27.

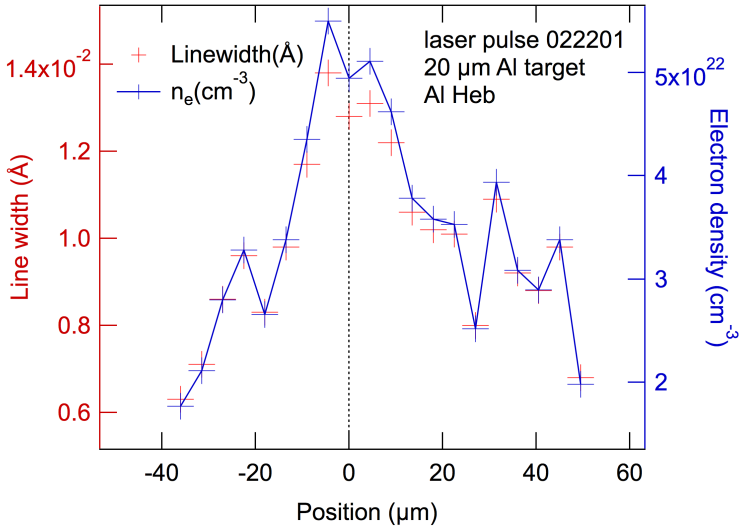

Figure 4.27: Plasma density calculated from the spectral linewidth for a single shot. The density profile over the plasma indicates that the highest density material is in the centre of the plasma, and with a maximum value of $5 \times 10^{22}\text{cm}^{-3}$ that the plasma from which this spectral line was emitted was less than solid density.

Figure 4.27 implies that there is significant variation in the electron density at different spatial positions, with a higher density region at the centre of the plasma. The maximum electron density seen is $5 \times 10^{22}\text{cm}^{-3}$, which is lower than that of solid aluminium. For this shot the laser intensity is $5 \times 10^{20}\text{Wcm}^{-2}$.

Due to the imaging properties of the crystal, cross sections can also be taken in the vertical direction (spatially) across the data to estimate the plasma size. By taking the FWHM of this cross section, the extent of the plasma can be estimated at different wavelength positions. At the position of the aluminium He-β line, the toroidal spectrometer infers a source size of $\approx 70\mu$m. This is larger than the sizes predicted by the 2D imager. The diameter of the source inferred by the 1D imaging

of the toroidal spectrometer is sensitive to the focussing of the crystal. Analysis of the data suggests that the source sizes are greater than double of those extracted from the 2D imager data.

4.10 Discussion

The converging characteristics, material temperatures, and heated region sizes captured within the data have been modelled by simulation of the interaction with the THOR code [69]. The results from this simulation are shown in Figure 4.28, and compared to experimental data.

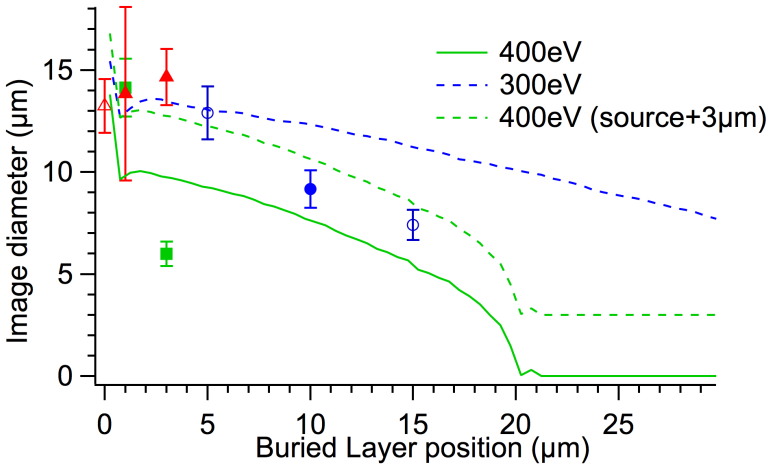

Figure 4.28: For a source diameter of 15μm, an absorption fraction of 0.5 and input divergence angle around 80° the temperature heating profile shows a good fit to experimental data.

Figure 4.28 the 400eV contour shown in solid green, provides the closest fit to the data characteristics and was obtained for an input divergence angle of 80°, a source diameter of 15μm and an absorption fraction of $\eta = 0.5$. The 300eV contour is shown as the initial diameter matches that of the experimental data, but the angle of convergence does not follow the trend of the data beyond depths of 5μm. The green dashed line on Figure 4.28 is identical to the solid green line, except an offset of 3μm has been applied. With this offset, the fit to experimental data is improved. This implies that for a source diameter of 18μm, a better comparison to

experimental data could be achieved.

The relation of the diameter of the x-ray emission images to the diameter of the fast electron beam via $\mathbf{j_f} + \mathbf{j_r} \approx 0$ needs extending to include the effect on x-ray emission by the material temperature inside the target. The target temperature is modelled using THOR, and the diameter of the resulting He-β emission image is inferred by using a separate model of x-ray emission with temperature. The results of this work are sensitive to choices made when using both of these models.

It is known that the x-ray emission recorded by the 2D imager results from material with a distribution of temperatures. In this work, a single temperature has been assumed to represent the location of emission to allow tracking through the target. However, this was necessary to infer key parameters such as electron divergence, absorption fraction and source size. In the future, the distribution of temperatures should be taken into account. Experimental data shows the heated region diameter gets smaller for increasing depth into the target. It was found here that this is the effect of the return current heating of the material inside the target.

4.11 Summary

An investigation of fast electron transport by high precision spectroscopic measurements of target heating has been presented in this chapter. An in-situ spatially resolved measurement of the Al He-β spectral line has been used to gain insight into the detailed target heating profile resulting from an intense laser-solid interaction. By absolute calibration and spectral modelling, the experimental data is used to produce estimates of the plasma temperature and how this correlated with depth into the target.

Tracking of hot material in the target has enabled an estimate of the diameter of a monochromatic x-ray image at given depth into the target to be made. This has been used to constrain the input parameters required to emulate the data characteristics, providing some insight into the quantitative values for electron beam divergence, source diameter and laser absorption fraction.

Temperature profiles of targets produced by hybrid-PIC modelling have been used to create synthetic emission data. For a given target temperature, the emission of the Al He-β line has been calculated and spatially resolved. The impact of the buried layer on the measurement has been found to be greatest for locations closest to the interaction. The effect seems to be within experimental error for buried layer depths around 10μm or more.

The experimental layout is presented in Section 4.2, and for details of the focal spot spatially and temporally we refer to Chapter 3 Section 3.2. The 2D imager and toroidal crystal spectrometer data is presented in Section 4.3. The 2D imaging data shows that the emission of the He-β line gets smaller with increasing depth into the target. This data is matched to simulation to obtain an estimate of the electron beam divergence of 70°±10°. It is further implied that the initial source of the electron beam is approximately 15μm in diameter to match the temperatures seen in the target to the diameter of the data images captured by the 2D imager, and that an absorption fraction of $\eta = 0.5$ improve this matching. The diameter of the images is compared with simulations with the derived input criteria, and a reasonable match is found, which improves with the introduction of 3μm offset. This offset suggests that further simulation with a slightly increased source size may show another improvement in the matching, further constraining the input parameters.

Simulations were also used to look at the change in magnetic field for injected electron divergence angles of 20° and 50°. For the 20° simulation, a collimating magnetic field is seen around the edge of the heated region to the extend of the simulated target depth. For the 50°, the magnetic field is shown to break up at approximate 15μm, as the temperature of the target drops and the temperature profile broadens.

The plasma temperature is also calculated from each of the images by absolute calibration of the x-ray film to reveal that the plasma temperature is approximately 300eV±50eV. There are larger errors on individual values largely due to the spread of temperatures in the image. Comparison of the temperatures derived for differ-

ent images, i.e. different buried layer depths is compared to simulation and good agreement is seen for depths up to 5μm. For depths of 10μm and 15μm, the derived temperature begins to diverge, with simulation predicting slightly lower temperatures.

The variation of spectral emission with temperature is given in Chapter 2, and is used here to calculate the emission of the He-β or Ly-β spectral lines from 3D temperature data from simulation. This is split into several 2D images over the depth of the target to provide a comparison of how each line develops with target depth and temperature. The emission of the Ly-β line is shown to peak at shallower depth than the He-β, which is due to the Ly-β being emitted from a hydrogenic and the population of Al XII peaks at higher temperature than Al XI for the He-β line. This synthetic data also replicates well the ring like structure seen in the emission as a feature of target temperature and implies that structure such as this seen in experimental data is not indicative of an electron beam being structured in this way. Similar structures extend to depths of several μm into the target.

A preliminary study on the effect of the buried layer itself on the transport of fast electrons and temperature in the target is also presented. By inserting a buried layer into simulation, plots of the magnetic field and temperature infer that the impact of the buried layer is greatest in the region closest to the interaction. It is also shown that the buried layer appears to have the highest impact on the magnetic field structure. For buried layer depths of 2μm the temperature is also shown to increase by 100eV inside the layer compared to material immediately preceding it.

Chapter 5

Hollow Atom Spectroscopy

5.1 Overview

This chapter presents spectroscopic measurement of hollow atom emission from the interaction of a high contrast, high intensity laser with a sold density target. High resolution spectroscopy is used to diagnose the presence of hollow ions.

Hollow atom spectra are x-ray spectra displaying emission from ions that are singly or multiply ionised in their inner shells whilst their outer shells are partially intact. There have been observations of hollow ion spectra for micron wavelength laser pulses of 0.5ps duration, and intensities of $1\times10^{19}\mathrm{Wcm}^{-2}$ and $1\times10^{20}\mathrm{Wcm}^{-2}$ [98, 109], but are more commonly seen in x-ray laser experiments [119, 120].

A conventional x-ray spectrum is one in which resonance lines lie on top of a continuum background. These spectra alongside appropriate simulations have been used for several decades to diagnose temperatures and densities of laser generated plasma. Hollow ion spectra are distinct in that they display broad regions of quasi-continuous emission due to exotic ionisation states in which resonance lines are embedded. They are distinct from K-shell spectrum, and are only adequately simulated by inclusion of a radiation field [97, 121, 122]. They are not described well by the standard collisional radiative model which is usual for analysing spectra from laser-solid interactions [121].

Experiments on long (micron) wavelength laser systems, do not generally yield hollow ion spectra. However, their appearance is becoming more important as opti-

cal laser systems move to high intensity shorter pulse lengths and higher contrast. Measurements presented here were recently published in references [97, 122, 123]. This is the first time an optical wavelength system has been used at intensities $> 10^{20} W cm^{-2}$ and high contrast to produce significant hollow ion emission.

This chapter firstly defines the hollow ion and illustrates its use as a diagnostic tool for high fluxes of fast electrons. The experimental layout is briefly discussed before moving on to experimental data. Simulation of the spectral line position of the two variants of the hollow ion is explained and compared with experimental data. The unique spectral data is recreated with the ATOMIC code. These calculations show that the ionisation in the plasma in this instance is dominated by photoionisation due to an intense radiation field. A study of atomic kinetics calculations and extension to relativistic energies has been done using the fully relativistic atomic physics code ATOMIC [72].

5.2 Hollow Ions

Hollow atoms or ions can be defined as those which have been ionised from the inside out [122], with multiple inner K- or L- shell electrons being ejected preferentially over outer shell or valence electrons. Removal of only the K- or L- shell electrons renders the ion hollow. A description of the two hollow ion variants and the $n = 2 \rightarrow 1$, and the K-α transition are shown in Figure 5.1(a). In Figure 5.1(b) the KK hollow ion is one in which there are two simultaneous K- shell vacancies, and the KL (Figure 5.1(c)) is a single vacancy in each of the K- and L- shells. In this Chapter, all spectra represented are for aluminium.

To form a KK hollow ion it is necessary to remove a second bound inner electron within the lifetime of a single K-shell vacancy. The single K-shell vacancy state has a lifetime of about 2 fs [124]. Consequently, a sufficiently intense flux of exciting photons or electrons is needed to create the second ionisation within this short lifetime, as the cross section of this transition is very small.

Intense beams of energetic electrons (either as fast forward beam or the neutral-

izing, return current [3]) are characteristic of ultra-intense laser-solid interactions, and can have sufficient flux to ionise multiple inner-shell electrons. The observation of a KK-α implies a radiative transition by an Lshell electron moving into a K-shell with two simultaneous vacancies.

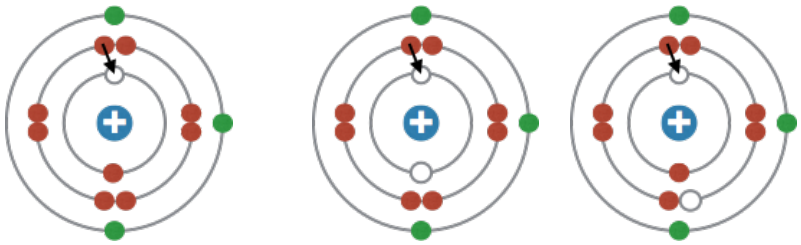

(a) K-α (b) KK-α (c) KL-α

Figure 5.1: (a) Schematic of the aluminium K-α photon emission. Recombination of an L-shell electron into a single K-shell vacancy ($1s^1 2s^2 2p^6 3s^2 3p^1 - 1s^2 2s^2 2p^5 3s^2 3p^1$) (b) Schematic of the aluminium KK hollow ion double K-shell (n=1) vacancy and the radiative decay on an L-shell electron with the remainder of the L-shell wholly or partially intact ($1s^0 2s^2 2p^6 3s^2 3p^1 - 1s^1 2s^2 2p^5 3s^2 3p^1$) (c) Schematic of the aluminium KL hollow ion radiative decay of an L-shell electron in an Al ion with simultaneous K-shell (n=1) and L-shell (n=2) vacancies ($1s^1 2s^2 2p^5 3s^2 3p^1 - 1s^2 2s^2 2p^4 3s^2 3p^1$)

A K-shell vacancy can decay either though the radiationless Auger process or via the radiative process. In the Auger process a bound electron decays into the inner shell vacancy resulting in the ejection of a second electron, and the radiative process is an equivalent decay resulting in emission of a photon. The familiar K-α emission results from the radiative recombination of an L-shell (n = 2) electron into a single K-shell (n = 1) vacancy with the remainder of the atom intact (see Chapter 1). For cold aluminium this transition has a wavelength of 8.36 Å[125]. The fluorescence yield for Al, i.e. the ratio of ions decaying by radiative processes and those that do so by non-radiative Auger processes, is approximately 4% [126].

In intense laser-solid interactions, the main mechanism for production of K-α radiation is the collision of an energetic electron with an inner K-shell bound electron in a cold ion [22, 103, 127]. The emission of K-α has been used extensively for the study of fast electron transport properties such as fast electron beam divergence or

beam spatial profile [19, 20, 128].

For experiments at high densities, the rate of recombination is high and ions recombine very quickly, on femtosecond timescales. Under these conditions, three-body recombination becomes the dominant recombination process, counteracting the rate of ionisation. This means that for high densities, emission from the L- and K- shells can still be seen, making it appropriate to solid density experiments.

In recent publications [97, 122, 123] measurements of unique atomic spectra as a petawatt laser strikes an aluminium target have been presented. The spectra illustrate the presence of an intense hollow ion signal from an ultra-intense laser-solid interaction. The spectra are unusual as emission from ions with double K-shell vacancies is seen to dominate emission.

5.3 Experimental Details

The experiment was carried out at the Vulcan Petawatt facility, with peak intensities of $3\times10^{20}\mathrm{Wcm}^{-2}$ as outlined in Section 3.2. The focussing spectrometer with spatial resolution (FSSR) used to capture the x-ray spectra, and the experimental layout is shown in Section 3.3.8. The spherical crystal used was placed 558mm from the target and 116mm from the film providing a demagnification factor of 0.2, at 45° from the target normal axis. Magnets were placed at the aperture to the crystal to prevent fogging by electrons and other energetic particles. The film cassettes were also protected by aluminium coated films and beryllium filters to exclude any other scattered signal inside the target chamber. A frequency doubled optical probe was used to observe the profile of the target front surface as the high intensity beam strikes the target, to allow the level of front surface plasma to be assessed. The electron spectrum was also measured by an electron spectrometer.

5.4 Experimental Data

Figure 5.2 shows a sample of the experimental data captured by the FSSR for Al foil targets. Figure 5.2 shows a sample of the spectroscopic data, alongside a

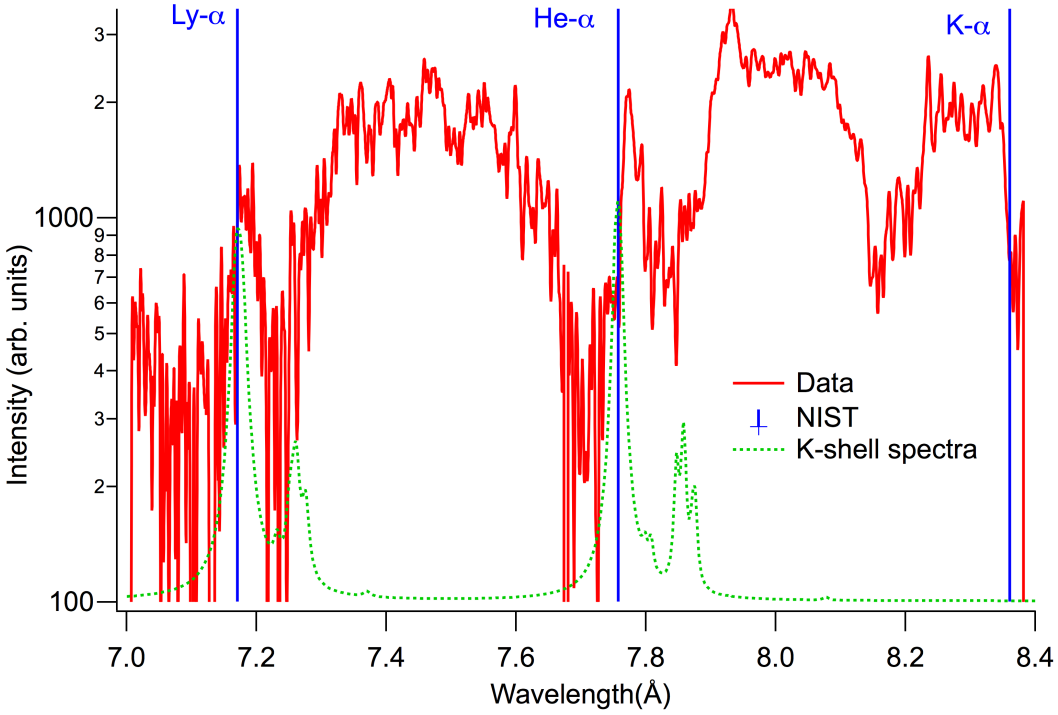

Figure 5.2: FSSR 1D data showing a strong emission in two regions. The solid red trace shows experimental data for a 1.5μm Al foil, which exhibits broad regions of emission between 7.2Å and 7.7Å, and 7.9Å−8.1Å. The dashed line is a Al K-shell spectra for 400eV and solid density, and the three resonance lines that occur over this range are also shown [125].

calculated Al K-shell spectrum at 400eV to highlight the key differences. Note the logarithmic scale of the y-axis for all figures containing this data. By comparing data to the calculated spectrum it is clear that the large regions of broad emission between 7.2Å−7.7Å, and 7.9Å−8.1Å are unusual. These regions of emission occur between the resonance lines (marked by vertical lines) and dominate emission at these wavelengths. This emission is due to the transitions from material dominated by hollow ions. This experimental data is the spectrum obtained for a 1.5μm Al foil target and a laser intensity of $3 \times 10^{20}\text{Wcm}^{-2}$. The results are also discussed in detail in [97], where it is observed that these regions of emission between the

spectral lines are not present when using thick Al foils.

5.5 Simulation

The Los Alamos National Laboratory atomic structure codes CATS and GIPPER [70, 129] have been used to calculate the spectral position and ionisation cross sections for the KK-α and KL-α.

The wavelength of hollow ion emission for each electronic configuration, the mechanism for generation of hollow ions, and their reaction cross sections are each simulated and discussed in the following sections.

5.5.1 Effect of ionisation on KK-α and KL-α emission

A neutral isolated aluminium ion in a KK or KL hollow ion state as defined in Figure 5.1 has 11 remaining bound electrons. The outermost electron is denoted as L8M3, which implies a filled L-shell with 8 electrons (n=2), and 3 remaining electrons in the M-shell (n=3). The hydrogenic case is denoted as L1, where one electron remains in the L-shell, as the K- shell has a double vacancy. If the electrons are removed from the ion in sequence, i.e. from the outside inwards from L8M3 to L1, then it is said to be sequentially ionised.

The wavelength of the KK-α and KL-α in an isolated and sequentially ionised Al ion is calculated using the Los Alamos suite of atomic codes [70]. The full sequence beginning with the ionisation of the outermost L8M3 electron and ending with the innermost L1 electron as calculated for both KK and KL hollow ion, is given in Figure 5.3. As the degree of ionisation increases, both transitions are seen to occur at shorter wavelengths until a single bound electron remains. This corresponds to the Ly-α transition for a hydrogenic ion. Starting with ionisation of only the outermost L8M3 electron ($3p^1$), the Al KK-α ($1s^0 2s^2 2p^6 - 1s^1 2s^2 2p^5$) hollow ion emission occurs at shorter wavelengths, approaching the Ly-α spectral line at 7.19 Å. Figure 5.3 shows the wavelength of the Al KL-α ($1s^1 2p^5 - 1s^2 2p^4$) emission starts at 8.27Å by approximately 50-90 mÅ for each electron beyond the L8 electron, with

the final observable line at 7.87 Å.

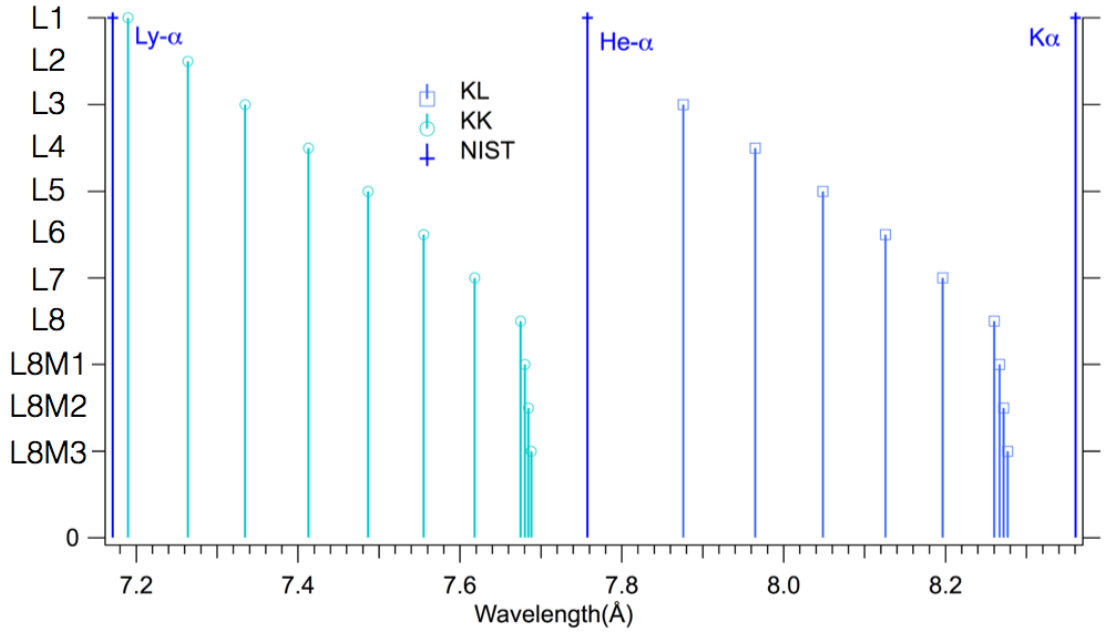

Figure 5.3: Notation and wavelength of each of the KK and KL hollow ion emission with the sequential ionisation of an Al ion, calculated using the COWAN code. The notation shows the shell and the number of electrons in that shell remaining, i.e. L8M3 denotes that 8 L-shell, and 3 M-shell electrons remain. This represents the outermost 3p electron and first to be ionised, and L1 corresponds to the final electron left in the L shell.

Figure 5.3 shows that for electrons in the M-shell, the spectral line position is altered a small amount for each sequential ionisation, approximately 3−5mÅ compared to L-shell ionisation. This increases by an order of magnitude for the L-shell where the average change in wavelength per election ionised is approximately 70mÅ. For the K-shell the wavelength change with each ionisation is between 0.28 Å and 0.4 Å. Figure 5.4 shows a comparison of this calculation with experimental data.

Figures 5.3 and 5.4 show that the change in spectral position resulting from the ionisation of the first four electrons is small, which is reflected in the figure. Figure 5.4 shows that for KK hollow ions, 8 separate peaks are seen in spectroscopic data, compared to the 11 peaks listed in Figure 5.3. The change in wavelength due to the ionisation of each M-shell electron is too small to be resolved. For the KL transitions, this is also true. When electrons from the M-shell are removed, there

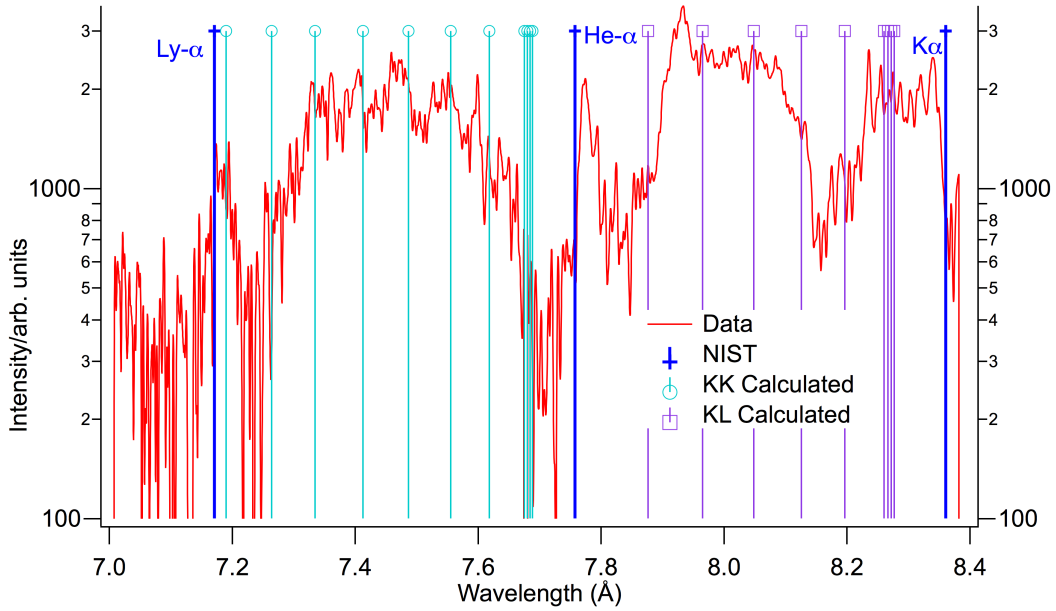

Figure 5.4: Simulated spectral line positions in comparison to experimental hollow ion data. The peaks largely coincide with the calculated KK-α positions implying that emission from individual charge states are resolved.

is little change in the wavelength, and for a complete series of 9 peaks, 5 peaks are observed.

Overall, a reasonable agreement is achieved between line position calculations and experimental data. The positions of the individual K-α components coincide with the visible peaks seen in x-ray emission, within a range of $\pm 50 m\mathring{A}$. This implies that the individual peaks on top of the broad emission between 7.2Å and 7.7Å is emission from individual charge states of the KK atomic configurations. The calculation shows less similarity to data in the KL range, however, later on in Section 5.5 it will be shown that full spectral simulation also shows peaked emission in this range and a reasonable agreement is achieved.

5.5.2 Simulation of hollow ion spectra

Simulation of spectroscopic data [97, 122] was performed using the ATOMIC code [71, 72]. This is an atomic kinetics model capable of solving the rate equations for both time dependent and steady state conditions. The calculation includes

collisional ionisation, photoionisation, collisional and radiative excitation and de-excitation, autoionisation and all recombination processes [130]. The simulations shown are performed with a bulk electron temperature of 55eV, an electron density of $\approx 3 \times 10^{23} cm^{-3}$ and an ion density of $6 \times 10^{22} cm^{-3}$, close to solid density for aluminium. These parameters are found to result in the best comparison to spectral data in the KK and KL emission regions [97, 122].

In Figure 5.5, the ATOMIC spectral calculation is compared to experimental measurement. Resonance line wavelengths are shown for reference.

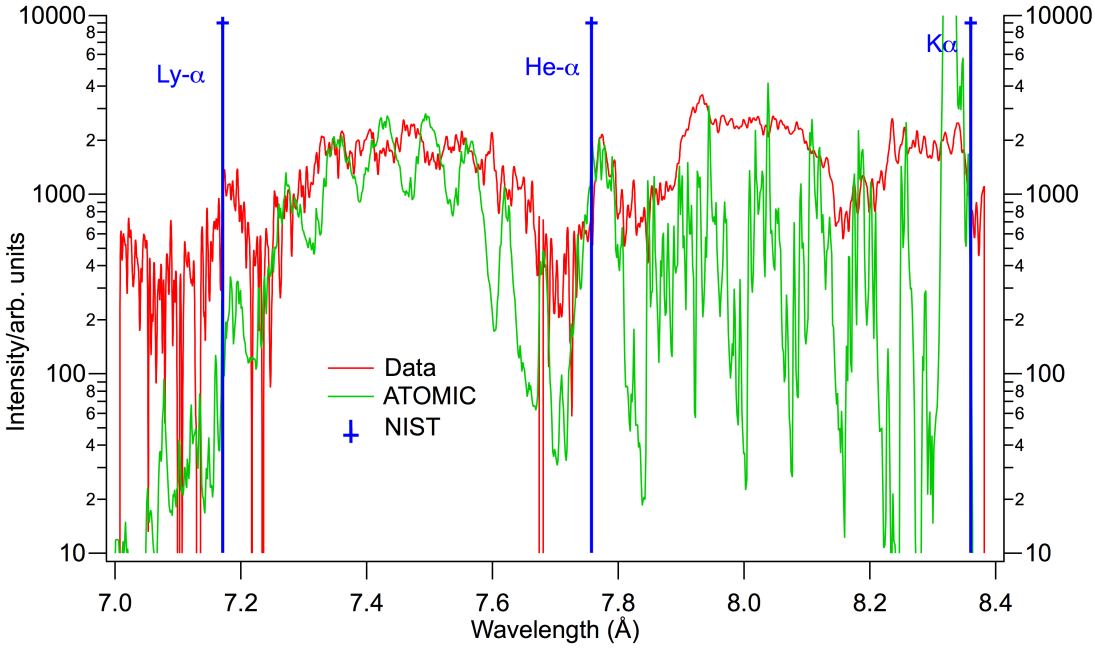

Figure 5.5: Simulated spectrum by ATOMIC in comparison to experimental hollow ion data shows broad regions of hollow ion emission in both experimental data and simulation.

Figure 5.5 shows that both calculated and measured spectra show distinguishable peaks from individual Al hollow ion charge states in the KK and KL wavelength ranges. These peaks are less clear and much broader in the KL range. The grouping of the first four (unresolved) electron configurations is also included in the detailed ATOMIC simulation.

The collision-radiative atomic calculations as reported by Colgan et al. [122] and Pikuz et al. [97] show that KK-α emission arises from intense x-ray radiation field.

The de-excitation rates for KK hollow ions indicates that the radiation intensity must exceed $10^{18}\mathrm{Wcm}^{-2}$. This radiation is thought to originate from relativistic electrons interacting with the target-surface sheath fields and non-linear Thomson scattering in the laser field [97]. Electrons are reflected, or reflux, between these sheath fields, losing energy by Bremsstrahlung and Thomson scattering with each pass of the target. This provides a plausible source for an intense radiation field. Only those photons or electrons that possess energy equal to or greater than the binding energy of a bound electron can cause its ionisation or excitation. The results imply that the laser interaction creates a large population of ions with completely empty innermost (principal quantum number, n = 1) atomic shells or K-shell with a double vacancy.

5.5.2.1 Radiation field

The presence of a fast electron tail on the electron distribution and a radiation field are essential for the simulation of hollow ion spectra.

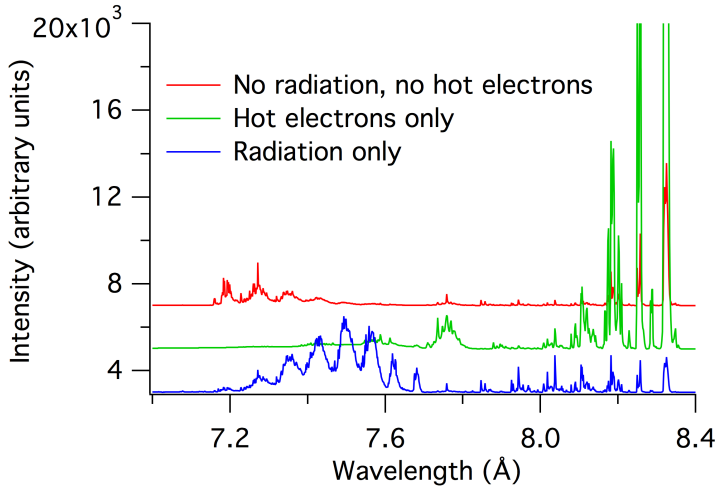

Figure 5.6: ATOMIC simulations showing the relative contributions to the overall spectra from the fast electron tail, and the radiation field [122]. Spectra are displaced vertically for clarity of comparison.

Figure 5.6 shows calculations performed with no radiation field and no fast electrons. In this case, very little emission is seen in the region of either type of hollow ion. The presence of an intense Planckian radiation field ($T_R = 3keV$) shows strong,

multiple peak emission in the region of the anticipated KK hollow ion emission, but does not well represent the experimental data for the KL hollow ion. The presence of the radiation field in isolation only provides good agreement with the KK portion of the spectrum. The intense emission in the KL range is not replicated. By introducing a hot tail to the electron energy distribution ($T_e = 5keV$) of 5% of the total electrons, emission resulting from the presence of KL hollow ions is reproduced [122]. This implies therefore that there are at least two important mechanisms, each contributing to the spectrum and dominating in difference spectral regions. The mechanisms of collisional and photoionisation and their individual contributions are considered in the next section.

5.5.3 Cross section

The semi-relativistic Cowan code [70] was used to generate the ionisation cross section for K-shell and L-shell electrons, by photoionisation or by electron impact ionisation. Semi relativistic calculations were performed for neutral aluminium and the results are shown in Figure 5.7.

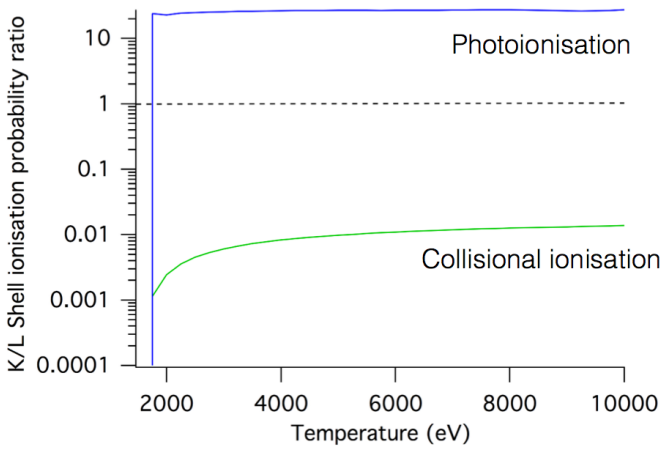

Figure 5.7: Ionisation probability ratio for an electron from the K- and L- shells by either photoionisation or by electron collision. At energies >1keV the probability of photoionisation is much greater than that of ionisation by hot electrons

Figure 5.7 shows he ratio of the K-shell and L-shell ionisation probability for collisional ionisation and for photoionisation. Note the logarithmic scale of the y-

axis. This indicates that for the K-shell, the cross section for ionisation by photons is greater than that of electron collisional ionisation. Therefore inferring that K-shell ionisation, is far more likely to be driven by x-ray photons than by electron collisions. For energies of 1 keV and above, KK hollow atoms are more efficiently created by x-ray photons. Conversely, it also shows that ionisation of an L-shell electron is far more likely to be caused by an electron collision than the absorption of a photon. This illustrates two distinct mechanisms driving these electronic states, as shown in Figure 5.6. The relative efficacy of K/L shell ionisation by photoionisation and collisional ionisation is approximately constant in this temperature range.

Measurement of hot electron beam currents have been made by photonuclear reactions in the past [131–133], and beam energies of several MeV are observed.

The KK hollow atom transition is used to infer the intensity of the radiation field. The KL hollow atom spectra could equally be used to calculate the electron flux required to generate the observed intensity in this region (7.8Å to 8.2Å). This calculation requires the calibration of the x-ray film used in this experiment such that a photon number can be calculated. If the film is calibrated, then modelling of the atomic cross sections as already described would allow calculation of the electron flux required to reproduce the intensity of measured spectra. This remains for further work.

It is known that electron beams generated in intense laser-solid interactions relativistic and that large currents can be generated [15, 25, 56, 131, 134]. The work of Evans et al. reports that fast electron fluxes of $3 \times 10^{31}\text{cm}^{-3}$ are needed for the creation of hollow atoms [109]. For electron beam currents ranging from 1kA to 10MA [131], electron fluxes range from 10^{30}cm^{-3} to 10^{34}cm^{-3}, indicating that the hot electron currents are expected to be very large. For fast electron temperature ranges relevant to laser-solid experiments of 1-10MeV, the cross section for collisional ionisation can be estimated to be 10^{-20}cm^{-3} [70]. For this experiment, the fast electron temperature estimated from the electron spectrum is found to be 6.2MeV [110]. Order of magnitude estimates of the KK-α photon flux from these

produce photon numbers of 10^5 to 10^{13} for KK-α [124, 126] over this this range. For fast electron current measurements to be from spectroscopic data, numbers of photons need to be estimated from the x-ray film exposure, to obtain the fast electron current.

The potential for hollow atom spectroscopy as a diagnostic of high electron beam currents, is dependent on the atomic cross section for electrons at the relevant speeds. The relativistic effects on the atomic cross sections must be considered.

5.5.3.1 Relativistic effects

The suitability of hollow atom spectroscopy as diagnostic for large (MA) fast electron beam currents is evaluated by the calculation of the atomic cross section for photoionisation (PI) and collisional ionisation (CI) at relativistic energies.

Fast electron temperatures are usually described with a Maxwellian distribution with a peak temperature of several MeV which is strongly relativistic, and a semi relativistic treatment of these electrons is no longer reliable. The peak temperature of the electron distribution as calculated by the ponderomotive scaling described in previous chapters, is approximately 6 MeV (see Section 2.7). Electrons of this temperature cannot be accurately described without taking into account relativistic effects.

To calculate the relativistically corrected cross sections for both CI and PI, the fully relativistic version of the Cowan code RATS [71, 72] has been used for K-shell and L-shell electrons for energies up to 10MeV [72]. For the 1s and 2s electrons, the result is shown in 5.8.

Figure 5.8 shows that data is well matched to the semi-relativistic case until energies of approximately 0.1 MeV where the two begin to diverge. All three of the marked points (a)−(c) highlight this deviation from the semi-relativistic case, as electrons become relativistic.

The relativistic code used here attempts to represent continuum functions for high energies on a radial mesh that may not be adequately resolved, so results for

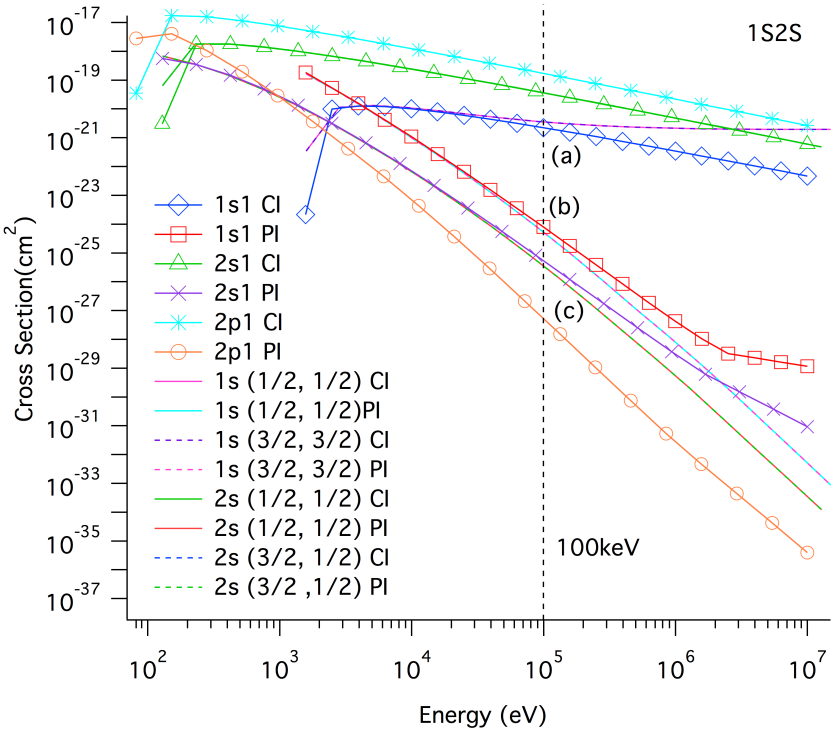

Figure 5.8: Fully relativistic [72] cross section calculation for collisional ionisation and photoionisation from the 1s and 2s subshells for neutral Al. Individual J states shown as $n\ell(J_i, J_f)$ in the legend are resolved for the 1s and 2s electron. Traces with markers on are semi-relativistic results for comparison. Points (a), (b) and (c) mark notable deviation. [73]

energies greater than 1 MeV have large errors and caution should be exercised [73].

Cross sections for the 1s and 2s electrons shown in Figure 5.8, and 2p electrons (not shown) for PI and CI are calculated and used to obtain the ionisation probability ratio for the K- and L- shell for CI and PI for relativistic energies. This is compared to Figure 5.7 calculated with a semi-relativistic code for energies $\leqslant$10keV. The result is shown in Figure 5.9, where preliminary calculations imply that ionisation by an intense radiation field remains the most likely mechanism for the K-shell up to energies of 8 MeV. This calculation shows a similar trend as in Figure 5.7, where the PI outweighs the CI, and its use as a diagnostic for high energy beams seems promising. The photoionisation cross section shows signs of steady decline at energies greater than 4 MeV but there is still a significant difference between these two. Due to the large difference between the CI and PI at these higher energies,

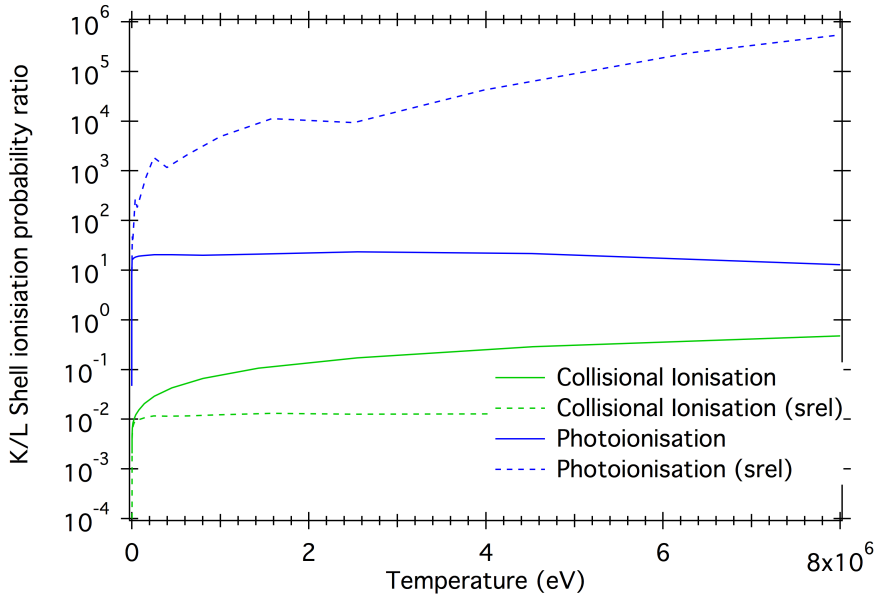

Figure 5.9: Ionisation probability ratio for an electron from the K- and L- shells by either photoionisation or by electron collision. At energies up to 8 MeV the probability of photoionisation of the K-shell is much greater than that of ionisation by hot electrons.

it is also implied that the ability to calculate fast electron flux as described in the preceding section also remains possible.

5.6 Summary

The hollow ion state has been described, and it is shown that KK and KL transitions result in unusual broad spectral features between the typical spectral lines Ly-α and He-α. These features are identified as emission of KK-α, resulting from the radiative transition into an empty K-shell with different degrees of ionization. Atomic kinetics calculations suggest that intense KK-α emission can occurs in solid density aluminium when driven by keV radiation fields. The fields are assumed to be Planckian. Analysis suggests the radiation field is driven by Bremsstrahlung and Thomson scattering as relativistic electrons reflux in thin targets. In these extreme conditions, the high recombination rates at solid density continually repopulate bound atomic states. The strong KK-α emission observed in Vulcan petawatt

experiments is reported in References [97, 122].

In this chapter, measurements of significant hollow ion emission have been presented. The intense emission of hollow ion transitions shows that the fast electron beam current must be large. The hollow ion spectra are modelled using an atomic physics code, and it is inferred that the ionisation into this exotic short lived state is by photoionisation. The probability of ionisation from each of the K- and L- shells for neutral aluminium is used in semi-relativistic calculations to show that the ionisation from the K- shell is many times more likely to be a result of photoionisation that collisional ionisation. Fully relativistic calculations have also been carried out that show for temperature ranges up to 1MeV and beyond that this continues to be the case.

Chapter 6

Polarisation Emission Spectroscopy

6.1 Overview

In this chapter, a methodology for the diagnosis of the velocity distribution function (VDF) of a laser generated beam of fast electrons is explored. Fast electron beam properties such as angular divergence and beam current have been the subject of a number of studies due to their impact on a number of important applications, and they indeed, constitute a large part of this thesis (Chapters 4 and 5). Despite all of this effort, relatively little is currently known about the distribution of velocities within this relativistic beam. The velocity distribution function (VDF) is a vital parameter as the degree of anisotropy that it possesses is related to the mechanism by which fast electrons are generated [135].

Early measurements of polarised line emission in the non-relativistic regime ($< 10^{18} W cm^{-2}$) show polarisation spectroscopy to be an effective tool for examination of the VDF. By comparison of the σ and π components of the Al He-α resonance line and satellite line emission, the electron velocity distribution in the overdense and underdense regions were seen to take on different forms [136, 137].

For sub-picosecond laser pulses approaching relativistic intensities, electron kinetics simulations predict non-Maxwellian and anisotropic electron distribution functions [138]. It has also been shown that the degree of polarisation seen from spectral line emission in buried layer targets is dependent on the depth at which the buried

layer is placed, and that from the degree of polarisation the angular spread of the VDF was be found to be 22.4° [82, 135]. These studies illustrate the sensitivity of spectral line polarisation to the anisotropy of the electron distribution function by modelling and experimentation, to be a powerful diagnostic of electron VDF.

As has been discussed in previous chapters (see Chapters 2 and 4), the interaction of an ultra-intense laser with a solid density target results in the production of a forward moving relativistic electron current, and a cooler counter propagating return current. The velocity distribution of the return current is widely considered to be isotropic, and collisional excitation of a 1s electron by an isotropic beam results in the statistical population of magnetic sublevels of the 2p subshell. The introduction of any perturbation (or anisotropy) to the distribution causes the preferential population of certain magnetic sublevels, resulting in a polarised x-ray emission. Polarised emission is present in both components of the Ly-α line. The two polarisation states σ and π can be isolated using spectroscopy, and the relative intensity of the polarised spectral line components from σ and π polarised spectra be compared to gain insight into the relative population of the magnetic sublevels.

This chapter outlines the theoretical basis for the experimental measurements presented, experimental approach, and provides an overview of the experimental data captured. Focus is also given to the modelling and simulation carried out to explore the origin of the polarised emission in terms of electron populations generated in the laser plasma interactions, and explains how this measurement can provide detailed understanding of the VDF. Using the hybrid-PIC code Zephyros, the electron kinetics are also investigated by spatially resolving the electron momentum in 2D and observing its development with time.

6.1.1 Theory

The Ly-α line is a 2p-1s transition in a hydrogen- like ion, where all other electrons have been ionised into continuum. The line has two components labelled herein as Ly-α_1 and Ly-α_2, arising from the total angular momentum quantum number

$j = \ell \pm \mathrm{s} = \frac{1}{2}, \frac{3}{2}$ quantum states.

The electron in the upper state n=2 exists either in the 2s (ℓ=0) or 2p (ℓ=1) electron subshells, with a spin s=$\frac{1}{2}$. Electrons from the 2p subshell can interact with the 1s subshell as transitions between 2s and 1s states are not dipole allowed (i.e. $\Delta\ell \neq \pm 1$) and as such, are not discussed further or shown in the schematic, Figure 6.1. Transitions from the 2p electron are split into three groups defined by $\Delta \mathrm{m}_j = 0, \pm 1$.

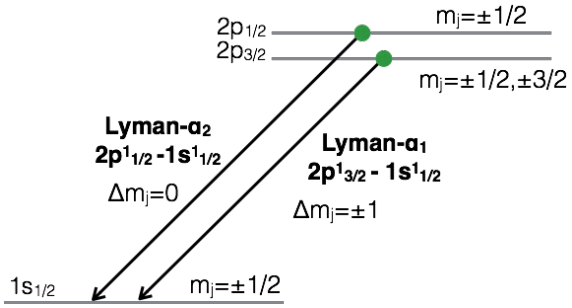

Figure 6.1: Dipole transitions allowed from the 2p to 1s electron states where $\Delta \mathrm{m}_j = 0, \pm 1$

For a given n and j, the magnetic sub levels defined by the values taken by m_j are degenerate. Photons that are emitted from each of these three levels are not distinguishable from one another. If an external magnetic or electric field is applied then energy of the levels changes, and the level is split by the Zeeman or Stark effects. Due to the change in energy level, the photon energy in transitions from each of these levels is altered, and the difference in their energy can be distinguished. This allows the use of spectral lines to diagnose such fields.

However, photons that are emitted from these three states are polarised with respect to the field lifting the degeneracy. The polarisation direction is dependent on which magnetic sub level forms the upper state of the 2p-1s transition. Consider a beam of exciting electrons. The velocity distribution function (VDF) for an isotropic beam will average to zero as it contains in equal proportions of electrons travelling in all directions. In this case, each of the magnetic sub levels is statistically populated and there is no net polarisation of the emitted spectral line. For a beam of exciting

electrons that is anisotropic, where there is a bias to one direction in the velocity distribution. This causes selective excitation of electrons into specific m_j states and a net polarisation of the emitted spectral line results.

Electrons in this hydrogenic system are excited from the 1s to 2p shell by electron impact excitation. The magnetic sublevel that the 1s electron is excited into is dependent on the angle of incidence of the incoming electron with respect to the quantisation axis. Consequently, if the beam is biased to one direction as in the anisotropic case, there is a bias on which level is populated and a net polarisation of the emitted photons. This results in preferential population of magnetic sub levels and a net polarisation of the spectral line. Measurement of the degree of polarisation of the spectral line provides a way to scrutinise electron beam anisotropy. Detailed knowledge of the atomic processes populating individual magnetic sub levels resulting in polarised emission, allows examination of the electron distribution function [139].

In the interaction of intense laser beams and solid targets, a mega-ampere beam of relativistic electrons is generated and propagates through the target, generating a large electric field setting the quantisation axis across the target, along the target surface normal axis or z direction. The propagation of a beam of electrons, defining this axis is shown in Figure 6.2.

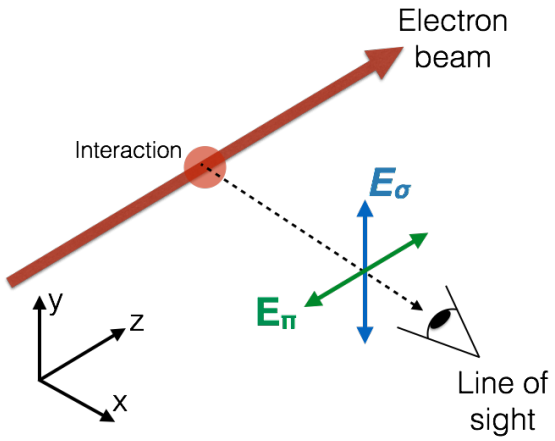

Figure 6.2: Experimental layout of the HOPG crystal spectrometers to isolate the σ- and π- polarised components to x-ray emission of the Ni Ly-α line.

Radiation with $\pi-$polarisation has its electric field component perpendicular to the quantisation direction (the direction of the incoming beam) and perpendicular in this case to the target surface normal. The σ-polarised light has its electric field components aligned parallel with the quantisation direction and parallel to the target surface normal. Both of these components are shown in Figure 6.2. The intensity of the two components are defined as I_π and I_σ.The degree of polarisation P present in the spectral line is given by the relative intensity of the two components,

$$P = \frac{I_\pi - I_\sigma}{I_\pi + I_\sigma} \tag{6.1}$$

Each component of the Lyman-α spectral line, denoted by Ly-α_1 and Ly-α_2, are associated with the transitions between the $2p_{3/2}$ and $2p_{1/2}$ quantum states respectively to the ground state $1s_{1/2}$. Each of these components contains both $\sigma-$ and $\pi-$ polarised light.

The shape and orientation of the electron orbital, is determined by its specific set of quantum numbers and is spatially quantised with respect to the quantisation axis. Due to the electric field present along this axis in this experiment, the electron orbitals align themselves with the quantisation axis.

Wavefunctions for with $m_j = \pm 1$ are dumbbell shaped and with no electric field present, point in a random distribution of directions. When there is an electric field the degeneracy is lifted the wavefunctions align with it and there is a change in their orientation. This results in a change of collisional cross section for electrons incident along the same direction as the electric field, or in this case, the quantisation axis.

For electrons in the $m_j = 0$, the electron orbital is spherical in shape and as such, whether there is an electric field applied or not, the cross section is angle independent. In contrast to a dumbbell shaped distribution which has an angle dependent cross section. The $m_j = \pm 1$ state is therefore dependent on the angle of the incoming electron.

Therefore the population, and ultimately emitted flux, from the $m_j = \pm 1$ states is dependent on the angle of incidence of the incoming electron and the $m_j = 0$ is

not. As the photons from the $m_j = \pm 1$ states are polarised and the $m_j = 0$ are not, the relative intensity of polarised and unpolarised light can reveal the degree of directionality in the incoming electron beam.

6.2 Experimental Approach

In Chapter 3, Section 3.3.7 (Figure 3.13) the layout of two flat highly-oriented pyrolytic graphite (HOPG) (002) crystals is shown. They are arranged perpendicular and parallel to the quantisation axis defined by the direction of fast electron propagation (z) (see Figure 6.2). This is the line defining the axis directly through the centre of the target along the target normal. The crystal arranged perpendicular to the quantisation axis captures the σ-polarised emission. The other crystal arranged orthogonally to the first, is parallel to the quantisation axis and captures the π-polarised component. Both spectrometers are positioned at a Bragg angle $\theta_B = 45°$, and the emission from both components is recorded on a single shot.

Classical x-ray scattering and Bragg diffraction are combined so that the intensity of the diffracted π-polarised x-rays depends on the Bragg angle such that $I_p \propto \cos^2 2\theta_{\mathrm{B}}$, where π-polarisation is defined with respect to the crystallographic planes. For Bragg angles of 45°, the π-polarised component is eliminated and the σ-polarised component can be observed in isolation. This is shown in Figure 3.14, in Chapter 3 by the rocking curve for the HOPG crystals.

Bragg diffraction of the Sulphur Ly-α_1 and α_2 lines occurs at Bragg angles of 44.81° and 44.87° respectively, and each of the polarised components can be measured in isolation on two separate crystals.

All of this combined produces two spectra, one populated by emission aligned to the quantisation axis and the other aligned perpendicular to the quantisation axis. The polarisation of the Ly-α_2 component where $j = 1/2$ remains constant at all angles due to its spherical electron orbital, resulting in the same intensity on both crystals. The Ly-α_1 where $j = 3/2$, the polarisation changes with increasing incoming beam energy as shown in Figure 6.3 [139].

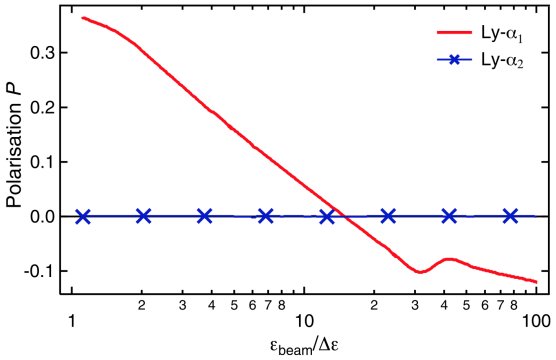

Figure 6.3: Flexible Atomic Code (FAC) calculations show that the polarisation of the Ly-α_1 component changes with electron beam impact energy whereas the Ly-α_2 does not, assuming collisional excitation only of the 1s electron [139].

In Figure 6.3, ϵ_{beam} is the energy of electron impact and $\Delta\epsilon$ is the excitation potential energy. Therefore the intensity of the Ly-α_2 line from each of the two crystals yields the polarisation according to 6.1.

6.2.1 Targetry

There are two types of foil targets used in this experiment. The first is 10μm $\times$ 100μm $\times$ 100μm square foils of Ni (8.9g/cc) mounted on sub-10μm copper wire stalks. The second target type are 25μm thick foils of polysulphone (PS) ($C_{27}H_{26}O_6S$), also in 100μm$\times$100μm squares with a density of 1.24g/cc. The PS targets also have coatings of 1μm Al on the front and 2μm on the rear surfaces to maintain consistency of the absorption physics in both targets. The targets are designed to be mass limited such that sufficient return current heating occurs to reach the K-shell.

6.3 Data and Results

Data obtained from the HOPG crystal spectrometer pair is shown in Figure 6.4. The data shows clear emission lines from the Ly-α and He-α transitions at 2622.6 eV and 2460.5 eV respectively. Due to the orientation of the image plate detectors, the π polarised data shows a higher background level than the σ polarised data, and

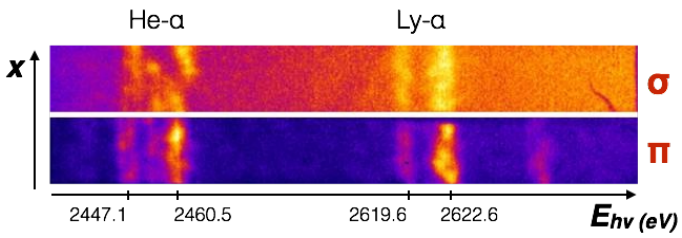

Figure 6.4: Typical data from HOPG spectrometers for a polysulphone target, 1μm Al/25μm PS/2μm Al. Top image: σ-polarised component and bottom image:π-polarised. The laser intensity in this shot was $2 \times 10^{20} W cm^{-2}$.

also is brighter at one end. The Ly-α spectrum in Figure 6.5 has been corrected for the background emission, beryllium filtering, mylar shielding, and for the nonlinear response of the image plate using a published model [140].

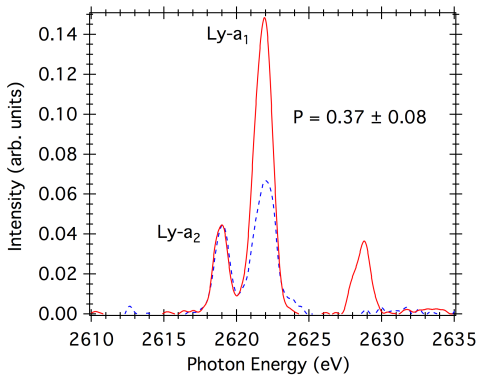

Figure 6.5: Spectra recorded from both the σ and π components of the S Ly-α emission. The π-polarised component is represented by the red and the σ-polarised by the blue. Both traces have been smoothed. The target is 1μm Al/ 25μm PS/ 2μm Al with a laser intensity $3{\times}10^{20} W cm^{-2}$.

Figure 6.5 shows the Ly-α spectral line for both polarised components. The two spectra have been calibrated by the area under the Ly-α_2 component. The area under the Ly-α_1 component for the normalised spectra is compared, and using (6.1), the degree of polarisation for the data shown in Figure 6.4 and 6.5 is P=0.37$\pm$0.08, which is a high value.

6.4 Simulation

Using Zephyros, the target heating profile resulting from a laser intensity of $5\times10^{20}Wcm^{-2}$ has been modelled. Temperature and current densities are shown in Figure 6.6 for a y-z slice taken through the centre of the target. Nickel has been used for modelling here as opposed to PS due to the difficulty in generating material properties of the complex molecule ($C_{27}H_{26}O_6S$).

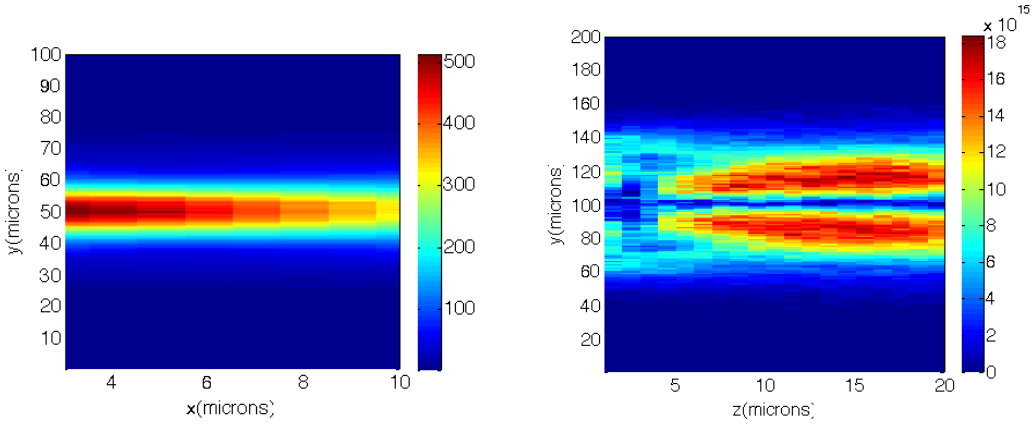

(a) Temperature (eV) at 100fs

(b) Current density of fast electrons (Am^{-2}) at 100fs

Figure 6.6: Zephyros simulations showing for a laser beam incident at the centre of the left boundary in both (a) background temperature and (b) current density, both at 100fs for laser intensity $5\times10^{20}Wcm^{-2}$ incident on a 10μm slab of Ni.

Figure 6.6(a) shows the temperature of the bulk target as a result of the return current heating. The initial injection of fast electron is at the centre of the left axis of Figure 6.6. Peak temperatures of 500eV are observed in the region close to the interaction and regions of 200eV-350eV extend to the rear surface of the 10μm target. The current density plot in Figure 6.6(b) shows a peak current densities of just over $10^{16}Am^{-2}$. Figure 6.6(b) suggests that in the laser direction there is structure seen current density, symmetrical about the laser axis.

6.5 Fast Electrons

The polarisation of x-ray emission is driven by the collision of return current electrons into bound electrons. The magnetic sublevel that an electron is promoted into,

is dependent on the velocity of the incoming electron. From Ohm's Law, the current density of the fast electron beam can be written as $\mathbf{j_{fast}} = n_e e \nu_{\mathbf{fast}}$ [51]. Current neutrality also requires that $\mathbf{j_{fast}} \approx -\mathbf{j_{rc}}$. Therefore we can write,

$$-\frac{n_{e(fast)}}{n_{e(rc)}} \approx \frac{\mathbf{v_{rc}}}{\mathbf{v_{fast}}} \tag{6.2}$$

where $\mathbf{v_{fast}}$ is the fast electron velocity, $n_{e(fast)}$ the fast electron density, and subscript 'rc' indicates the equivalent quantities for the return current. The negative sign is indicative of the opposite direction of the fast and return currents. The positive direction is along the target normal axis, away from the interaction. The absorption of the laser energy into the target can be expressed as $\eta(I\lambda^2)$ is a constant amount, and $\eta \approx 0.3$.

The fast electron current density n_{fast} is extracted from Zephyros, and the solid density for nickel is $n_{solid} \approx 10^{23}\text{cm}^{-3}$. By making an assumption that the number density of the return current $n_{rc} \approx n_{solid}$ [141], the ratio of the number density of the fast electron current and the return current from (6.2) is denoted as $f = 0.12\%$, where f is the fraction of hot electrons. If this is known then we can also write $\mathbf{v_{rc}} = f\mathbf{v_{fast}}$ [142].

In this way, the velocity of the fast electrons velocity can be used to estimate the velocity of the return current electrons, propagating in the opposite direction. How the velocity is distributed within the fast electron current therefore could provide information about the distribution of the return current beam. The following is an interrogation of the fast electron kinetics produced by Zephyros for a Ni slab of 10μm thickness to attempt to identify how the velocity is distributed among the particles.

Within a simulated 10μm Ni slab, the electron population in a layer of 1μm thickness, positioned at 4μm depth into the target is used to calculate the distribution of particle velocities. The details of how Zephyros generates and injects particles into the simulation is detailed in Section 2.11. The simulations shown here are the result of a laser intensity of $5 \times 10^{20}\text{Wcm}^{-2}$, in a spot diameter of 7μm centrally

positioned on the target surface.

Zephyros outputs the three components of momentum and the location of each macroparticle. Each represents a number of fast electrons, and these can be resolved spatially to infer the location of the fast electrons in the target. This can show how fast electron velocity is distributed within the slice.

6.5.1 Fast Electron Velocity

The three components of momentum generated for each fast electron macroparticle, are converted into velocity by using the relativistically corrected $\mathbf{p} = \gamma m_0 \mathbf{v}$ where $\gamma = \sqrt{1 - \frac{v^2}{c^2}}$ into velocity $\mathbf{v}$. Figure 6.7 (a) - (c) shows the three velocity components v_x, v_y and v_z.

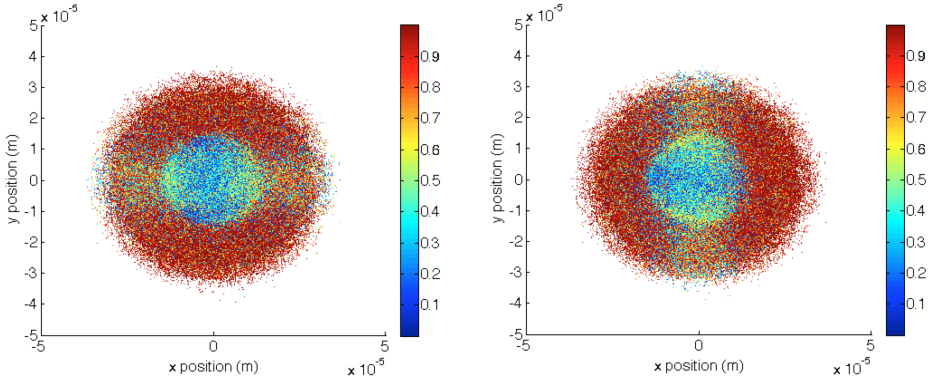

(a) v_x

(b) v_y

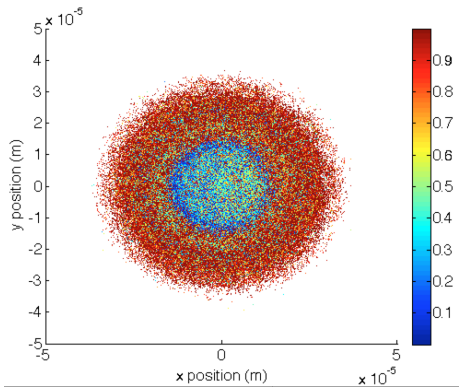

(c) v_z

Figure 6.7: Spatially resolved velocity components v_x, v_y, v_x derived from momentum components p_x, p_y and p_z at t=100fs. All velocities are in units of c.

In each of the components of velocity shown in Figure 6.7, there is a clear ring

structure in terms of speed. The laser axis is at $x = y = 0$ on all plots. There is a central region where electron macroparticles are less energetic than in the ring surrounding. Figure 6.7 shows that the fast electrons occupy a diameter of approximately 60μm at a depth of 4μm. By assuming that the macroparticles diverge at the input divergence angle of 50°, this equates to a diameter of approximately 10μm at the front surface. Figure 6.6 shows the region of the target that is heated is approximately 15μm in diameter, implying that near the front surface of the target, the two radii are similar.

Heated material in Figure 6.6 continues to have a radius of approximately 15μm at a depth of 4μm, which is far smaller than the indicated diameter over which fast electrons are seen at the same depth.

As is described by (2.22) in Chapter 2, the number of real particles represented by each macroparticle in Zephyros simulations is related to the local laser intensity where it was generated. By assuming that the Gaussian form of the laser profile has not been significantly modified the number of particles in every macroparticle can be calculated. Using (2.22), it is found that for an assumed Gaussian laser intensity of $5 \times 10^{20}\mathrm{Wcm}^{-2}$, there are up to 5.7×10^5 particles in a macroparticle at the peak of the laser intensity and 3×10^4 particles per macroparticle around the edges of the pulse. The peak of the laser profile is at x=y=0. There are greater numbers of less energetic particles at the centre of the image

This allows the total number of electrons represented in the slice to be calculated for each timestep of the simulation. The number of fast electrons in a 1μm thick slice placed at 4μm from the front surface is shown in Figure 6.8.

Figure 6.8 shows that during the laser pulse (between 0 and 600fs) the fast electron population increases. The number of macroparticles in the simulation is plotted on the right axis of Figure 6.8. During the laser pulse, the number of electrons in the simulation increases peaking at $3{\times}10^{12}$, which is the equivalent of an electron density of $3{\times}10^{12}\mathrm{cm}^{-3}$. After the pulse ends at 600fs there is a steep drop in fast electron number where $5{\times}10^{24}s^{-1}$ are lost. However, as this analysis

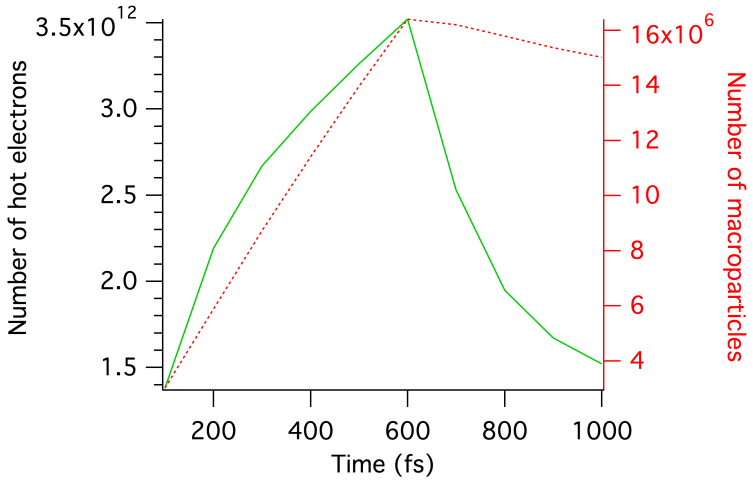

Figure 6.8: Number of macroparticles (dashed curve, right axis) and fast electrons (solid curve left axis) in a $4-5\mu$m slice midway into a 10μm solid nickel target evolving over 1ps. (to obtain fast electron density, multiply by factor $10^8 cm^{-3}$).

represents the electron population in a small slice of the target for specific times, the electron population is not 'static'. Fast electron macroparticles are free to enter and leave the slice as they travel through the target. Here we have a thin target, and its width can be propagated by a fast electron in 30fs, which is far smaller than the timesteps used here. Therefore electrons that are refluxing will contribute to the total number and the distribution of velocities. To isolate the electrons on their first pass through the target, a reduction in timestep is needed such that the time taken is less than the target thickness divided by the speed of light.

6.5.2 Distribution of particle velocities

The distribution of the electron velocity components added in quadrature over in the sampling slice has been calculated. Figure 6.9 shows how velocity is distributed within the hot electrons in the simulation.

Figure 6.9 shows the calculated speed distribution in the simulation of a 10μm nickel target subject to a simulated laser intensity of $5 \times 10^{20}\mathrm{Wcm}^{-2}$. Due to the large number of particles in the simulation, data in Figure 6.9 has been binned, at regular intervals of $1\times10^6\mathrm{ms}^{-1}$. Between the timesteps the profile has broadened, and the number of electrons with energies $> 0.5c$ has increased. The total number

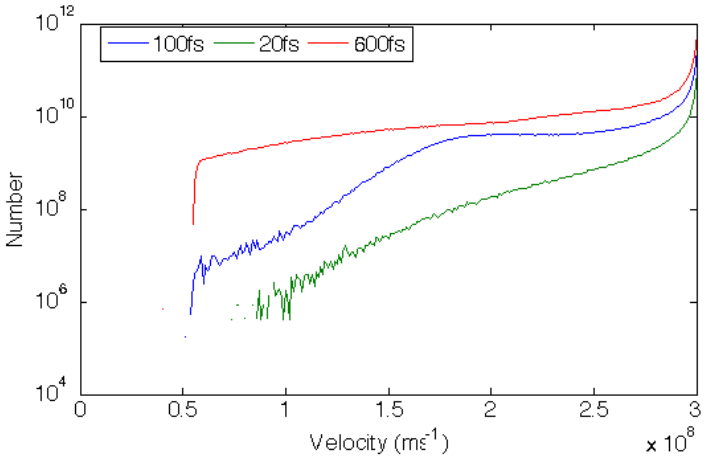

Figure 6.9: The velocity distribution function calculated for timesteps of 20fs, 100fs and 600fs for a 1μm thick slice of a 10μm nickel target subject to a simulated laser intensity of $5 \times 10^{20} Wcm^{-2}$

of electrons has also increased from $1{\times}10^{12}$ to $3{\times}10^{12}$ between 100fs and 600fs.

Figure 6.10 shows that beyond the end of the laser pulse, the structure that is seen in simulations thus far is short lived. The laser pulse ends at 600fs and by 700fs, the early time structure of the current density seen in Figure 6.6 most clearly, has broken up. The distribution of electron velocity has spread considerably, filling the entire simulation box of 100μm dimensions, and the recognisable spot in Figure 6.7 has become diffuse.

A particle travelling at the speed of light takes around 30fs to travel the target thickness of 10μm, which is far shorter than the timesteps of 100fs. Therefore the particle can traverse the target over 3 times between timesteps, and the fast electron population becomes diffuse. At 100fs, the fast electrons are confined to a radius of approximately 30 μm, and by 600fs the entire of the simulation box is filled.

Due to the increased structure seen at early times, the electron kinetics simulation implies that polarised emission is likely to arise from early times.

Polarised x-rays are emitted from the target as a result of an anisotropic velocity distribution, as has been discussed. Figure 6.7 shows that there are no significantly sized beam components or filaments in electron temperature or current density, but there are regions where an increased number of electrons are travelling in one

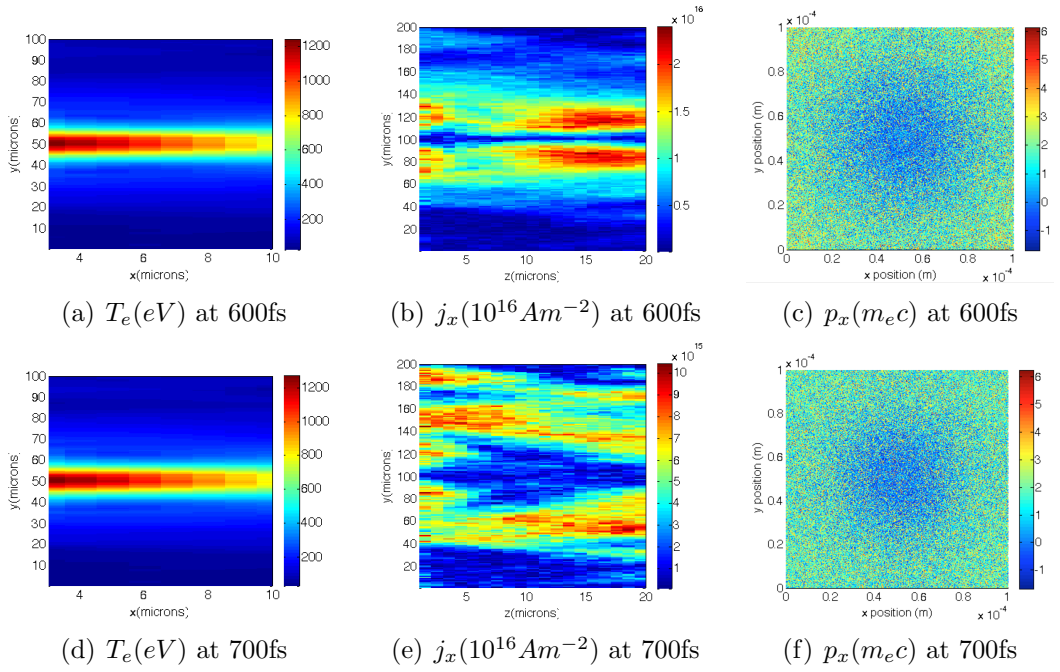

(a) $T_e(eV)$ at 600fs (b) $j_x(10^{16}Am^{-2})$ at 600fs (c) $p_x(m_ec)$ at 600fs

(d) $T_e(eV)$ at 700fs (e) $j_x(10^{16}Am^{-2})$ at 700fs (f) $p_x(m_ec)$ at 700fs

Figure 6.10: Time dependent dynamics. All structure in electron momentum and current density has dissipated by 700fs, 100fs after the end of the driving pulse.

direction.

6.6 Summary

Measurement of polarised x-ray emission arising from a sulphur target is presented. The polarisation calculated for the shot detailed in Section 6.3 shows a high, positive polarisation of 0.37±0.08. This implies that the return current has a highly anisotropic velocity distribution function.

Simulations are able to provide the momentum of each macroparticle and the equivalent velocity is found. These simulations show that there are large numbers of fast electrons within the target, centred around the laser axis. The radius over which fast electrons are seen is approximately 30μm for a time of 100fs.

Knowledge of the laser spatial profile and modelling allows the velocity of each of the fast electrons passing through a 2D slice of the target to be calculated and spatially resolved. From this the distribution of fast electrons with velocity is described in Section 6.5.2.

The time dependence of fast electron temperature, current density and electron velocity is also briefly investigated, and infers that the polarised emission results from early time dynamics of a few hundred fs. At later times, structure that is generated in the current density and electron kinetics is seen to become less clear and the system begins to equilibrate, particularly once the laser pulse has ended.

Chapter 7

Conclusions

The primary focus of this thesis has been to investigate the properties of relativistic electron beams that are generated in the interaction of a high intensity laser with a solid target. A combination of experimental data and modelling has been employed to constrain key electron beam parameters such as the electron beam divergence and to explore the electron velocity distribution. This has included the use of a variety of novel spectroscopic techniques, the results of which will be briefly summarised here.

To address the electron beam divergence, a single spectral line was imaged in two dimensions to track the emission with depth into the target using a buried layer. As the buried layer was placed at greater depth into the target, the emission of the Al He-β line was seen to decrease in diameter. The relationship between the size of the emission and the diameter of the return current beam is complicated by the relationship between x-ray emission and plasma temperature. Collisional radiative modelling was used to gain knowledge of how the spectral line flux is related to plasma temperature for the He-β spectral line. Modelling of this spectral emission shows that for an expanding target temperature profile, the image produced in 2D is expected to decrease in diameter with greater depth, and is not indicative of the return current beam becoming smaller in size.

This allows the matching of simulations to experimental data, and the derivation of a set of conditions that best fit the experimental data. The matching of the

converging characteristics of the data with temperature contours in the simulation, has allowed an estimate of the electron beam divergence of 70°±10° half angle in Section 4.6. This simulation also implies that an input source size of approximately 15μm and an absorption fraction of $\eta = 0.5$ is needed. Comparison of all of the experimental data to a simulation with these parameters as inputs shows reasonable agreement for depths up to 10μm depth. A small offset of 3μm is applied to the simulation improves this agreement, implying that additional simulations increasing the source size to 18μm would provide a better comparison to the data.

The input divergence angle is seen to have an impact on the collimating effect of the self generated magnetic field. The magnetic field and temperature in simulations of CH slabs with an input electron beam divergence angle of 20° and 50° were compared in Section 4.6. For an injected divergence angle of 20° the magnetic field has a collimating effect to the full depth of the simulation (30μm). For an injected divergence angle of 50°, the magnetic field loses its collimating effects at depths of approximately 10μm, at the same point where the temperature profile of the target becomes very broad and diffuse. This implies that the beam of electrons could be initially collimated by the magnetic field before it begins to diverge at approximately 10μm.

The temperature of the plasma has been estimated by the use of absolutely calibrated x-ray film to be approximately 310eV±50eV. Over the target depths explored in this experiment, little change in the target temperature is seen, which is not in agreement with literature that shows a decrease of around 10% to 20% over the same range of depths.

The relationship defined previously between the x-ray emission flux and the target temperature allows the x-ray emission from the target to be modelled. In simulations of a 30μm slab of CH designed to emulate the transport of energy up until a buried layer, the emission of the Al He-β and Ly-β spectral line has been modelled in a predictive fashion. The modelling shows that the Ly-β spectral line flux peaks closer to the interaction region than the He-β line. This is attributed

to the fact that more energy is required to reach the hydrogen like state of the ion than the helium like. The He-β modelling is seen to replicate the ring like structure seen in the experimental data up until depths of approximately 10μm. Beyond this depth the profile becomes peaked. The Ly-β does not exhibit such a distinct ring like structure as the centre of the target is not hot enough to fully strip the ion and cause the drop in emission that allows ring like structures to form.

The effect of the buried layer on the fast electron transport is discussed in Section 4.8. The buried layer is seen to have a greater impact on the magnetic field than the target temperature. The effect of the change in resistivity between the CH and the layer causes the generation of magnetic fields at the buried layer interface. For a depth of 2μm, the temperature inside the buried layer is increased by 100eV in comparison to the material immediately preceding it. For buried layer depths of 10μm the temperature change is only 20eV. A change of 100eV is significant enough to cause a change in the average ionisation state of the plasma and alter the image seen on the diagnostic.

Intense hollow atom emission is observed using high resolution spectroscopy measurements from aluminium targets. Modelling of these spectra indicates that the ionisation of the atom in to the KK hollow atom state is driven primarily by an intense radiation field, whilst the ionisation of the ion into the KL hollow atom state is by collisional electrons. The ionisation probability of K and L shell electrons by photons and by collision with electrons is used in semi-relativistic and relativistic calculations to show that for the K shell, photoionisation is around ten times more likely than collisional ionisation. Fully relativistic modelling of the same quantities produces the same conclusion, and for energies up to 1MeV, it is shown that photoionisation remains the dominant ionisation mechanism for the K shell electron.

The emission of the two components of polarised x-ray emission are measured on two independent HOPG crystal spectrometers. Due to the sulphur Ly-α_2 line remaining unpolarised, the two films are normalised and the relative intensity of the Ly-α_1 component can be compared for each to calculated the degree of polarisation.

For a shot analysed here, the polarisation found is approximately P=+0.4. This large and positive value for the degree of polarisation indicates that the return current beam is responsible for the biased population of magnetic sublevels and that almost the entire return current beam has an anisotropic velocity distribution function. The polarisation of x-ray emission is driven by the return current, which is generated as a result of the propagation of the fast electrons. The velocity of the incoming electron, is related to which of the magnetic sub levels it promotes bound electrons to, and therefore a large number of electrons with a single velocity will cause biased population of the related magnetic sublevel. This results in the polarised emission. The kinetics of the fast electrons in an isolated slice of a solid nickel target are investigated and the velocity distribution is calculated. No significant filamentary structures were seen in the spatially resolved distribution of electrons.

7.1 Further Work

This section highlights aspects of the work presented that can either be extended or used as the basis of further research. It is split into two categories, dependent on the nature of the work.

7.1.1 Further Experimental Work

Chapter 4 has shown the use of a 2D imager and toroidal spectrometer to provide a way of estimating electron beam divergence and target heating characteristics for an intensity of $5\times10^{20}\mathrm{Wcm}^{-2}$. Green et al. [19] showed that electron beam divergence increases with the laser intensity. The target heating can be accurately estimated using the diagnostics shown in Chapter 4. Selection of an appropriate spectral line visible over a wide range of temperatures such as the Ly-β line, would facilitate a scan of target heating over the intensity range of $5\times10^{18}\mathrm{Wcm}^{-2}$ up to $5\times10^{21}\mathrm{Wcm}^{-2}$. Over this range, the effects of incident laser energy or laser intensity on target heating can be explored with this novel diagnostic for comparison to previous measurements. This can also be used to assess the change in electron beam divergence over the range

with energy and intensity.

The difference in Z between the CH and Al buried layer in the buried targets already in place, produces magnetic fields and potentially has impact on the propagation of fast electrons within the target. To reduce the jump in Z and the resistivity gradient between the two materials, a lower Z material such as chlorine could be used for the buried layer, or silicon used for the bulk target.

The effects of lattice structure on fast electron transport in laser-solid interaction has been investigated by McKenna et al., showing that the proton beam produced is more uniform for ordered target lattice structures [143]. Modulations in the spatial intensity profile caused by a filamented electron beam could further cause local regions of intense target heating, which will be imprinted in a 2D x-ray image. It is possible that the effects of the target structure on heating could be assessed by spectral line emission.

Calculating a quantitative value for the required electron flux has not been possible in this case. A small amount of related experimental work to calibrate the film with a well characterised x-ray source, will enable the films exposure to be analysed quantitatively and the number of photons on the film calculated. This reveals the total number of emitting ions and hence the population of the KL state. This information can be used to calculate the minimum flux required to produce that many electron collisional ionisation events over the time of the experiment. The work described by Evans et al. (2006) [109] shows time resolved KK emission as a streaked spectra, which could also be an avenue for investigation.

7.1.2 Further Simulation and Analysis

In Section 4.6 the electron divergence angle was estimated and the values of the electron source size and laser-target coupling efficiency were also inferred. Two tasks can improve this estimate. Firstly, use of a weighted function to account for the emission of the He-β line from a distribution of temperatures and secondly, the availability of more simulation results at a greater number of divergence angles to

increase the accuracy of the estimation of divergence angle.

Synthetic data is created using the relationship of line flux with temperatures, for simulated slabs of CH to represent the transport of energy leading up to the buried layer. Data presented here shows depths of up to 15μm, as experimental data is available up to this depth. Simulation data exists for up to 30μm and a different emission profile is seen. This has not been included in this thesis due to time constraints but remains an area of study.

The effect of the buried layer on electron transport has been estimated by simulation of CH slabs containing a 1μm buried layer, to represent the 0.1μm layer used experimentally. Simulation of a 0.1μm layer has not been completed for this thesis due to time constraints, as the computational expense of simulation a layer of that thickness is not trivial. The ability of the Zephyros code to evolve on these very small timescales to provide accurate descriptions of the plasma parameters would also need to be considered.

The modelling employed to look at the electron kinetics with regards to the polarised x-ray emission in Chapter 6 could equally be applied to the buried layer simulations present in Chapter 4. Spatially resolved information about the fast electrons in this material could be used to compare the region over which the target has been heated as a result of the return current, and the region of which large numbers of electrons propagate in a slice of the target. This slice can be conveniently chosen to be the buried layer itself, or material elsewhere in the target. Currently, the Zephyros code output momentum information that relates to macro particles and not the individual electrons that it contains. The properties of the macro particle reflect the properties of the electrons which it represents but the number of electrons, and the potential to generate a velocity distribution of fast electrons is lost. A new version of the code has been created in recent weeks leading up to the submission of this thesis, that allows the number of electrons per macro particle to be part of the output. However at present, this is at the expense of the spatial resolution and analysis of the electron kinetics going forward is likely to be an amalgam of

simulations where spatially resolved and absolute electron numbers are obtained. This work is ongoing.

The polarisation data which is analysed in Chapter 6 and presented in the above conclusions, is for a single shot. To increase the accuracy of this value, the polarisation degree obtained over a number of shots would be analysed and averaged. The same shot could also be analysed multiple times to assess the human error in identifying spectral lines and applying a dispersion. Furthermore, the model described in the analysis of the hollow ion spectra [97, 122] has been recently updated to include the resolution of individual magnetic sub levels. As such this could be a powerful tool in examining the relationship between the velocity of the incoming electrons and the magnetic sub levels to which a bound electron is excited.

References

[1] Max Tabak, James Hammer, Michael E. Glinsky, William L. Kruer, Scott C. Wilks, John Woodworth, E. Michael Campbell, Michael D. Perry and Rodney J. Mason, *Ignition and high gain with ultrapowerful lasers*, Phys. Plasmas, **1**(5), 1626 (1994), ISSN 1070664X

[2] S.C. Wilks and W.L. Kruer, *Absorption of ultrashort, ultra-intense laser light by solids and overdense plasmas*, Quantum Electronics, IEEE Journal of, **33**, 1954 (1997), ISSN 0018-9197

[3] J. Meyer-Ter-Vehn S. Atzeni, *The Physics of Inertial fusion* (Clarendon Press - Oxford, 2004)

[4] Y. Sentoku, T. E. Cowan, A. Kemp and H. Ruhl, *High energy proton acceleration in interaction of short laser pulse with dense plasma target*, Phys. Plasmas, **10**(5), 2009 (2003), ISSN 1070664X

[5] R. A. Snavely, M. H. Key, S. P. Hatchett, T. E. Cowan, M. Roth, T. W. Phillips, M. A. Stoyer, E. A. Henry, T. C. Sangster, M. S. Singh, S. C. Wilks, A. MacKinnon, A. Offenberger, D. M. Pennington, K. Yasuike, A. B. Langdon, B. F. Lasinski, J. Johnson, M. D. Perry and E. M. Campbell, *Intense High-Energy Proton Beams from Petawatt-Laser Irradiation of Solids*, Phys. Rev. Lett., **85**, 2945 (2000)

[6] P. Mora, *Plasma Expansion into a Vacuum*, Phys. Rev. Lett., **90**, 185002 (2003)

[7] S. C. Wilks, A. B. Langdon, T. E. Cowan, M. Roth, M. Singh, S. Hatchett, M. H. Key, D. Pennington, A. MacKinnon and R. A. Snavely, *Energetic proton generation in ultra-intense laser–solid interactions*, Physics of Plasmas, **8**(2), 542 (2001)

[8] M. Borghesi, D.H. Campbell, A. Schiavi, O. Willi, A.J. Mackinnon, D. Hicks, P. Patel, L.A. Gizzi, M. Galimberti and R.J. Clarke, *Laser-produced protons and their application as a particle probe*, Laser and Particle Beams, **20**, 269 (2002), ISSN 1469-803X

[9] K W D Ledingham and W Galster, *Laser-driven particle and photon beams and some applications*, New Journal of Physics, **12**(4), 045005 (2010)

[10] M. Roth, T. E. Cowan, M. H. Key, S. P. Hatchett, C. Brown, W. Fountain, J. Johnson, D. M. Pennington, R. A. Snavely, S. C. Wilks, K. Yasuike, H. Ruhl, F. Pegoraro, S. V. Bulanov, E. M. Campbell, M. D. Perry and H. Powell, *Fast Ignition by Intense Laser-Accelerated Proton Beams*, Phys. Rev. Lett., **86**, 436 (2001)

[11] S Fujioka, H Nishimura, H Takabe, N Yamamoto, K Nishihara, D Salzmann, T Norimatsu, N Miyanaga, K Mima, H Azechi, A Sunahara, Y Shimada, Y Izawa, K Nagai, F Wang, J Zhong, G Zhao, Y Li, Q Dong, S Wang, Y Zhang, J Zhang, Y-J Rhee, Y-W Lee and D-H Kwon, *Laser-produced plasmas as unique x-ray souces for industry and astrophysics*, Journal of Physics: Conference Series, **244**(1), 012001 (2010)

[12] P. J. Mallozzi, H. M. Epstein, R. G. Jung, D. C. Applebaum, B. P. Fairand, W. J. Gallagher, R. L. Uecker and M. C. Muckerheide, *Lasergenerated plasmas as a source of x rays for medical applications*, Journal of Applied Physics, **45**(4) (1974)

[13] J.C. Kieffer, A. Krol, Z. Jiang, C.C. Chamberlain, E. Scalzetti and Z. Ichalalene, *Future of laser-based X-ray sources for medical imaging*, Applied Physics B, **74**(1), s75 (2002), ISSN 0946-2171

[14] R.W. Lee, H.A. Baldis, R.C. Cauble, O.L. Landen, J.S. Wark, A. NG, S.J. Rose, C. Lewis, D. Riley, J.-C. Gauthier and P. Audebert, *Plasma-based studies with intense X-ray and particle beam sources*, Laser and Particle Beams, **20**, 527 (2002), ISSN 1469-803X

[15] J. A. Koch, M. H. Key, R. R. Freeman, S. P. Hatchett, R. W. Lee, D. Pennington, R. B. Stephens and M. Tabak, *Experimental measurements of deep directional columnar heating by laser-generated relativistic electrons at near-solid density*, Phys. Rev. E, **65**, 016410 (2001)

[16] D. J. Hoarty, P. Allan, S. F. James, C. R. D. Brown, L. M. R. Hobbs, M. P. Hill, J. W. O. Harris, J. Morton, M. G. Brookes, R. Shepherd, J. Dunn, H. Chen, E. Von Marley, P. Beiersdorfer, H. K. Chung, R. W. Lee, G. Brown and J. Emig, *Observations of the Effect of Ionization-Potential Depression in Hot Dense Plasma*, Phys. Rev. Lett., **110**, 265003 (2013)

[17] C. R. D. Brown, D. J. Hoarty, S. F. James, D. Swatton, S. J. Hughes, J. W. Morton, T. M. Guymer, M. P. Hill, D. A. Chapman, J. E. Andrew, A. J. Comley, R. Shepherd, J. Dunn, H. Chen, M. Schneider, G. Brown, P. Beiersdorfer and J. Emig, *Measurements of Electron Transport in Foils Irradiated with a Picosecond Time Scale Laser Pulse*, Phys. Rev. Lett., **106**, 185003 (2011)

[18] U. Zastrau, P. Audebert, V. Bernshtam, E. Brambrink, T. Kämpfer, E. Kroupp, R. Loetzsch, Y. Maron, Yu. Ralchenko, H. Reinholz, G. Röpke, A. Sengebusch, E. Stambulchik, I. Uschmann, L. Weingarten and E. Förster, *Temperature and Kα-yield radial distributions in laser-produced solid-density plasmas imaged with ultrahigh-resolution x-ray spectroscopy*, Phys. Rev. E, **81**, 026406 (2010)

[19] J. S. Green, V. M. Ovchinnikov, R. G. Evans, K. U. Akli, H. Azechi, F. N. Beg, C. Bellei, R. R. Freeman, H. Habara, R. Heathcote, M. H. Key, J. A. King, K. L. Lancaster, N. C. Lopes, T. Ma, A. J. MacKinnon, K. Markey, A. McPhee, Z. Najmudin, P. Nilson, R. Onofrei, R. Stephens, K. Takeda, K. A. Tanaka, W. Theobald, T. Tanimoto, J. Waugh, L. Van Woerkom, N. C. Woolsey, M. Zepf, J. R. Davies and P. A. Norreys, *Effect of Laser Intensity on Fast-Electron-Beam Divergence in Solid-Density Plasmas*, Phys. Rev. Lett., **100**, 015003 (2008)

[20] K. L. Lancaster, J. S. Green, D. S. Hey, K. U. Akli, J. R. Davies, R. J. Clarke, R. R. Freeman, H. Habara, M. H. Key, R. Kodama, K. Krushelnick, C. D.

Murphy, M. Nakatsutsumi, P. Simpson, R. Stephens, C. Stoeckl, T. Yabuuchi, M. Zepf and P. A. Norreys, *Measurements of Energy Transport Patterns in Solid Density Laser Plasma Interactions at Intensities of* $5\times10^{20}\,Wcm^{-2}$, Phys. Rev. Lett., **98**, 125002 (2007)

[21] R. H. H. Scott, F. Perez, J. J. Santos, C. P. Ridgers, J. R. Davies, K. L. Lancaster, S. D. Baton, Ph. Nicolai, R. M. G. M. Trines, A. R. Bell, S. Hulin, M. Tzoufras, S. J. Rose and P. A. Norreys, *A study of fast electron energy transport in relativistically intense laser-plasma interactions with large density scalelengths*, Physics of Plasmas, **19**(5), 053104 (2012)

[22] V. M. Ovchinnikov, G. E. Kemp, D. W. Schumacher, R. R. Freeman and L. D. Van Woerkom, *How well do time-integrated K-α images represent hot electron spatial distributions?*, Phys. Plasmas, **18**(7), 072704 (2011), ISSN 1070664X

[23] S. D. Baton, J. J. Santos, F. Amiranoff, H. Popescu, L. Gremillet, M. Koenig, E. Martinolli, O. Guilbaud, C. Rousseaux, M. Rabec Le Gloahec, T. Hall, D. Batani, E. Perelli, F. Scianitti and T. E. Cowan, *Evidence of Ultrashort Electron Bunches in Laser-Plasma Interactions at Relativistic Intensities*, Phys. Rev. Lett., **91**, 105001 (2003)

[24] J. J. Santos, F. Amiranoff, S. D. Baton, L. Gremillet, M. Koenig, E. Martinolli, M. Rabec Le Gloahec, C. Rousseaux, D. Batani, A. Bernardinello, G. Greison and T. Hall, *Fast Electron Transport in Ultraintense Laser Pulse Interaction with Solid Targets by Rear-Side Self-Radiation Diagnostics*, Phys. Rev. Lett., **89**, 025001 (2002)

[25] M. Storm, A. A. Solodov, J. F. Myatt, D. D. Meyerhofer, C. Stoeckl, C. Mileham, R. Betti, P. M. Nilson, T. C. Sangster, W. Theobald and Chunlei Guo, *High-Current, Relativistic Electron-Beam Transport in Metals and the Role of Magnetic Collimation*, Phys. Rev. Lett., **102**, 235004 (2009)

[26] F. F. Chen, *Introduction to Plasm Physics and Controlled Fusion 2nd Edition* (Springer, 2006)

[27] Richard Pitzpatrick, *The Physics of Plasmas* (University of Texas at Austin)

[28] William. L. Kruer, *The Physics of Laser-Plasma Interactions* (ABP, 2003)

[29] R. P. Drake, *High Energy Density Physics - Fundamentals, Inertial Fusion and Experimental Astrohysics* (Springer - Shock Wave and High Pressure Phenomena (ISBN 3-540-29314-0))

[30] I O Musgrave, C Hernandez-Gomez, D Canny, R Heathcote, R J Clarke, J L Collier and S Bandyopadhyay, *Nanosecond contrast measurements of the Vulcan Petawatt facility*, CLF Annual Report, pp. 197–199 (2004)

[31] Paul Gibbon, *Short Pulse Laser Interactions with Matter* (Imperial College Press)

[32] W. L. Kruer and Kent Estabrook, *JB heating by very intense laser light*, Phys. Fluids, **28**(1), 430 (1985), ISSN 00319171

[33] S. C. Wilks, W. L. Kruer, M. Tabak and A. B. Langdon, *Absorption of ultraintense laser pulses*, Phys. Rev. Lett., **69**, 1383 (1992)

[34] D. C. Carroll, *Laser-Driven Ion Acceleration: Source Optimisation and Optical Control*, Ph.D. thesis, University of Strathclyde (2008)

[35] F. Brunel, *Not-so-resonant, resonant absorption*, Phys. Rev. Lett., **59**, 52 (1987)

[36] Hong bo Cai, Wei Yu, Shao ping Zhu, Chun yang Zheng, Li hua Cao and Wen bing Pei, *Vacuum heating in the interaction of ultrashort, relativistically strong laser pulses with solid targets*, Phys. Plasmas, **13**(6), 063108 (2006), ISSN 1070664X

[37] Paul Gibbon and A. R. Bell, *Collisionless absorption in sharp-edged plasmas*, Phys. Rev. Lett., **68**, 1535 (1992)

[38] A. J. Kemp, Y. Sentoku and M. Tabak, *Hot-Electron Energy Coupling in Ultraintense Laser-Matter Interaction*, Phys. Rev. Lett., **101**, 075004 (2008)

[39] C. D. Chen, P. K. Patel, D. S. Hey, A. J. Mackinnon, M. H. Key, K. U. Akli, T. Bartal, F. N. Beg, S. Chawla, H. Chen, R. R. Freeman, D. P. Higginson, A. Link, T. Y. Ma, A. G. MacPhee, R. B. Stephens, L. D. Van Woerkom, B. Westover and M. Porkolab, *Bremsstrahlung and K fluorescence measurements for inferring conversion efficiencies into fast ignition relevant hot electrons*, Physics of Plasmas (1994-present), **16**(8), 082705 (2009)

[40] D. W. Forslund, J. M. Kindel and K. Lee, *Theory of Hot-Electron Spectra at High Laser Intensity*, Phys. Rev. Lett., **39**, 284 (1977)

[41] F. N. Beg, A. R. Bell, A. E. Dangor, C. N. Danson, A. P. Fews, M. E. Glinsky, B. A. Hammel, P. Lee, P. A. Norreys and M. Tatarakis, *A study of picosecond lasersolid interactions up to 1019 Wcm2*, Physics of Plasmas (1994-present), **4**(2) (1997)

[42] M. G. Haines, M. S. Wei, F. N. Beg and R. B. Stephens, *Hot-Electron Temperature and Laser-Light Absorption in Fast Ignition*, Phys. Rev. Lett., **102**, 045008 (2009)

[43] A. G. MacPhee, K. U. Akli, F. N. Beg, C. D. Chen, H. Chen, R. Clarke, D. S. Hey, R. R. Freeman, A. J. Kemp, M. H. Key, J. A. King, S. Le Pape, A. Link, T. Y. Ma, H. Nakamura, D. T. Offermann, V. M. Ovchinnikov, P. K. Patel, T. W. Phillips, R. B. Stephens, R. Town, Y. Y. Tsui, M. S. Wei, L. D. Van Woerkom and A. J. Mackinnon, *Diagnostics for fast ignition science (invited)*, Rev. Sci. Instrum., **79**(10), 10F302 (2008), ISSN 00346748

[44] C. D. Chen, J. A. King, M. H. Key, K. U. Akli, F. N. Beg, H. Chen, R. R. Freeman, A. Link, A. J. Mackinnon, A. G. MacPhee, P. K. Patel, M. Porkolab, R. B. Stephens and L. D. Van Woerkom, *A Bremsstrahlung spectrometer using K-edge and differential filters with image plate dosimeters*, Rev. Sci. Instrum., **79**(10), 10E305 (2008), ISSN 00346748

[45] Paul Gibbon, *Efficient production of fast electrons from femtosecond laser interaction with solid targets*, Phys. Rev. Lett., **73**, 664 (1994)

[46] M. I. K. Santala, M. Zepf, I. Watts, F. N. Beg, E. Clark, M. Tatarakis, K. Krushelnick, A. E. Dangor, T. McCanny, I. Spencer, R. P. Singhal, K. W. D. Ledingham, S. C. Wilks, A. C. Machacek, J. S. Wark, R. Allott, R. J. Clarke and P. A. Norreys, *Effect of the Plasma Density Scale Length on the Direction*

of Fast Electrons in Relativistic Laser-Solid Interactions, Phys. Rev. Lett., **84**, 1459 (2000)

[47] A. P. L. Robinson and H. Schmitz, *Elliptical magnetic mirror generated via resistivity gradients for fast ignition inertial confinement fusion*, Physics of Plasmas (1994-present), **20**(6), 062704 (2013)

[48] D. A. MacLellan, D. C. Carroll, R. J. Gray, N. Booth, M. Burza, M. P. Desjarlais, F. Du, B. Gonzalez-Izquierdo, D. Neely, H. W. Powell, A. P. L. Robinson, D. R. Rusby, G. G. Scott, X. H. Yuan, C.-G. Wahlström and P. McKenna, *Annular Fast Electron Transport in Silicon Arising from Low-Temperature Resistivity*, Phys. Rev. Lett., **111**, 095001 (2013)

[49] X H Yuan, A P L Robinson, M N Quinn, D C Carroll, M Borghesi, R J Clarke, R G Evans, J Fuchs, P Gallegos, L Lancia, D Neely, K Quinn, L Romagnani, G Sarri, P A Wilson and P McKenna, *Effect of self-generated magnetic fields on fast-electron beam divergence in solid targets*, New Journal of Physics, **12**(6), 063018 (2010)

[50] R. J. Gray, X. H. Yuan, D. C. Carroll, C. M. Brenner, M. Coury, M. N. Quinn, O. Tresca, B. Zielbauer, B. Aurand, V. Bagnoud, J. Fils, T. Khl, X. X. Lin, C. Li, Y. T. Li, M. Roth, D. Neely and P. McKenna, *Surface transport of energetic electrons in intense picosecond laser-foil interactions*, Applied Physics Letters, **99**(17), 171502 (2011)

[51] A R Bell, A P L Robinson, M Sherlock, R J Kingham and W Rozmus, *Fast electron transport in laser-produced plasmas and the KALOS code for solution of the VlasovFokkerPlanck equation*, Plasma Physics and Controlled Fusion, **48**(3), R37 (2006)

[52] Hannes Alfvén, *On the Motion of Cosmic Rays in Interstellar Space*, Phys. Rev., **55**, 425 (1939)

[53] A. R. Bell and R. J. Kingham, *Resistive Collimation of Electron Beams in Laser-Produced Plasmas*, Phys. Rev. Lett., **91**, 035003 (2003)

[54] A. P. L. Robinson and M. Sherlock, *Magnetic collimation of fast electrons produced by ultraintense laser irradiation by structuring the target composition*, Phys. Plasmas, **14**(8), 083105 (2007), ISSN 1070664X

[55] J R Davies, J S Green and P A Norreys, *Electron beam hollowing in lasersolid interactions*, Plasma Physics and Controlled Fusion, **48**(8), 1181 (2006)

[56] S. Kar, A. P. L. Robinson, D. C Carroll, O Lundh, K. Markey, P. McKenna, P. Norreys and M. Zepf, *Guiding of Relativistic Electron Beams in Solid Targets by Resistively Controlled Magnetic Fields*, Phys. Rev. Lett., **102**, 055001 (2009)

[57] M L Rogelstad, F B Yousif, T J Morgan and J B A Mitchell, *Stimulated radiative recombination of H+ and He+*, Journal of Physics B: Atomic, Molecular and Optical Physics, **30**(17), 3913 (1997)

[58] David Salzmann, *Atomic Physics in Plasmas* (International series of monographs on physics, Oxford University press, 1998)

[59] Lecture by Prof. Steve Rose, Excitation and ionisation in high energy density plasmas, 68th Scottish Universities Summer School in Physics (SUSSP) - Laser-Plasma Interactions and Applications

[60] J.J. MacFarlane, I.E. Golovkin, P. Wang, P.R. Woodruff and N.A. Pereyra, *SPECT3D A multi-dimensional collisional-radiative code for generating diagnostic signatures based on hydrodynamics and PIC simulation output*, High Energy Density Physics, **3**(12), 181 (2007), ISSN 1574-1818, radiative Properties of Hot Dense Matter

[61] J. J. MacFarlane, I. E. Golovkin, P. R. Woodruff, D. R. Welch, B. V. Oliver, T. A. Mehlhorn and R. B. Campbell, *Simulation of the ionisation dynamics of Aluminium irradiated by intense short-pulse lasers*, Prism Computation Sciences Internal Report, **WPo3.3** (obtained 2014)

[62] R. C. Mancini, J. E. Bailey, J. F. Hawley, T. Kallman, M. Witthoeft, S. J. Rose and H. Takabe, *Accretion disk dynamics, photoionized plasmas, and stellar opacities*, Physics of Plasmas (1994-present), **16**(4), 041001 (2009)

[63] P. M. Nilson, W. Theobald, C. Mileham, C. Stoeckl, J. F. Myatt, J. A. Delettrez, J. MacFarlane, I. A. Begishev, J. D. Zuegel, R. Betti, T. C. Sangster and D. D. Meyerhofer, *Target-heating effects on the K-alpha 1,2-emission spectrum from solid targets heated by laser-generated hot electrons*, Physics of Plasmas (1994-present), **18**(4), 042702 (2011)

[64] P. F. Knapp, S. B. Hansen, S. A. Pikuz, T. A. Shelkovenko and D. A. Hammer, *Calibration and analysis of spatially resolved x-ray absorption spectra from a nonuniform plasma*, Review of Scientific Instruments, **83**(7), 073502 (2012)

[65] Y. T. Lee and R. M. More, *An electron conductivity model for dense plasmas*, Physics of Fluids (1958-1988), **27**(5) (1984)

[66] J. R. Davies, *How wrong is collisional Monte Carlo modeling of fast electron transport in high-intensity laser-solid interactions?*, Phys. Rev. E, **65**, 026407 (2002)

[67] A. P. L. Robinson, *Zephyros User Manual v0.72* (Central Laser Facility, STFC, 2013)

[68] J. R. Davies, A. R. Bell, M. G. Haines and S. M. Guérin, *Short-pulse high-intensity laser-generated fast electron transport into thick solid targets*, Phys. Rev. E, **56**, 7193 (1997)

[69] N J Sircombe, S J Hughes and M G Ramsay, *Integrated calculations of short-pulse laser interactions with matter*, New Journal of Physics, **15**(2), 025025 (2013)

[70] Los Alamos National Laboratory suite of atomic physics codes

[71] N. H. Magee, J. Abdallah, J. Colgan, P. Hakel, D. P. Kilcrease, S. Mazevet, M. Sherrill, C. J. Fontes and H. L. Zhang, *Los Alamos Opacities: Transition from LEDCOP to ATOMIC*, AIP Conference Proceedings, **730**(1) (2004)

[72] Douglas H. Sampson, Hong Lin Zhang and Christopher J. Fontes, *A fully relativistic approach for calculating atomic data for highly charged ions*, Physics Reports, **477**(46), 111 (2009), ISSN 0370-1573

[73] James Colgan, Los Alamos National Laboratory - Private Correpondence November 2013

[74] C. N. Danson, P.A. Brummitt, R.J. Clarke, J.L. Collier, B. Fell, A.J. Frackiewicz, S. Hancock, S. Hawkes, C. Hernandez-Gomez, P. Holligan, M.H.R. Hutchinson, A. Kidd, W.J. Lester, I.O. Musgrave, D. Neely, D.R. Neville, P.A. Norreys, D.A. Pepler, C.J. Reason, W. Shaikh, T.B. Winstone, R.W.W. Wyatt and B.E. Wyborn, *Vulcan Petawattan ultra-high-intensity interaction facility*, Nuclear Fusion, **44**(12), S239 (2004)

[75] C.N. Danson, R. Allott, G. Booth, J. Collier, C.B. Edwards, P.S. Flintoff, S.J. Hawkes, M.H.R. Hutchinson, C. Hernanez-Gomez, J. Leach, D. Neely, P. Norreys, M. Notley, D.A. Pepler, I.N. Ross, J.A. Walczak and T.B. Winstone, *Generation of focused intensities of 5x1019 Wcm-2*, Laser and Particle Beams, **17**, 341 (1999), ISSN 1469-803X

[76] C.N. Danson, P.A. Brummitt, R.J. Clarke, J.L. Collier, B. Fell, A.J. Frackiewicz, S. Hawkes, C. Hernandez-Gomez, P. Holligan, M.H.R. Hutchinson, A. Kidd, W.J. Lester, I.O. Musgrave, D. Neely, D.R. Neville, P.A. Norreys, D.A. Pepler, C.J. Reason, W. Shaikh, T.B. Winstone, R.W.W. Wyatt and B.E. Wyborn, *Vulcan petawatt: Design, operation and interactions at 5x1020 Wcm-2*, Laser and Particle Beams, **23**, 87 (2005), ISSN 1469-803X

[77] Hiromitsu Kiriyama, Mori Michiaki, Yoshiki Nakai, Takuya Shimomura, Hajime Sasao, Momoko Tanaka, Yoshihiro Ochi, Manabu Tanoue, Hajime Okada, Shuji Kondo, Shuhei Kanazawa, Akito Sagisaka, Izuru Daito, Daisuke Wakai, Fumitaka Sasao, Masayuki Suzuki, Hideyuki Kotakai, Kiminori Kondo, Akira Sugiyama, Sergei Bulanov, Paul R. Bolton, Hiroyuki Daido, Shunichi Kawanishi, John L. Collier, Cristina Hernandez-Gomez, Chris J. Hooker, Klaus Ertel, Toyoaki Kimura and Toshiki Tajima, *High-spatiotemporal-quality petawatt-class laser system*, Appl. Opt., **49**(11), 2105 (2010)

[78] Donna Strickland and Gerard Mourou, *Compression of amplified chirped optical pulses*, Optics Communications, **56**(3), 219 (1985), ISSN 0030-4018

[79] I.N Ross, P Matousek, M Towrie, A.J Langley and J.L Collier, *The prospects for ultrashort pulse duration and ultrahigh intensity using optical parametric chirped pulse amplifiers*, Optics Communications, **144**(13), 125 (1997), ISSN 0030-4018

[80] C Hernandez-Gomez, D Canny, I O Musgrave and J L Collier, *Picosecond contrast measurements of the Vulcan Petawatt facility*, CLF Annual Report, p. 200 (2004)

[81] Ian Musgrave, Waseem Shaikh, Marco Galimberti, Alexis Boyle, Cristina Hernandez-Gomez, Kate Lancaster and Robert Heathcote, *Picosecond optical parametric chirped pulse amplifier as a preamplifier to generate high-energy seed pulses for contrast enhancement*, Appl. Opt., **49**(33), 6558 (2010)

[82] Y. Inubushi, T. Kai, T. Nakamura, S. Fujioka, H. Nishimura and K. Mima, *Analysis of x-ray polarization to determine the three-dimensionally anisotropic velocity distributions of hot electrons in plasma produced by ultrahigh intensity lasers*, Phys. Rev. E, **75**, 026401 (2007)

[83] E. Martinolli, M. Koenig, J. M. Boudenne, E. Perelli, D. Batani and T. A. Hall, *Conical crystal spectrograph for high brightness x-ray K-α spectroscopy in subpicosecond laser-solid interaction*, Rev. Sci. Instrum., **75**(6), 2024 (2004), ISSN 00346748

[84] H Nishimura, Y Inubushi, M Ochiai, T Kai, T Kawamura, S Fujioka, M Hashida, S Simizu, S Sakabe, R Kodama, K A Tanaka, S Kato, F Koike, S Nakazaki, H Nagatomo, T Johzaki and K Mima, *Study of fast electron transport in hot dense matter using x-ray spectroscopy*, Plasma Physics and Controlled Fusion, **47**(12B), B823 (2005)

[85] Kaye and Laby Online Version 1.0, *Table of Physical and Chemical Constants, 4.2.1 X-ray absorption edges, characteristic X-ray lines and fluorescence yields* (NPL, 2005)

[86] T. Missalla, I. Uschmann, E. Forster, G. Jenke and D. von der Linde, *Monochromatic focusing of subpicosecond x-ray pulses in the keV range*, Review of Scientific Instruments, **70**(2), 1288 (1999)

[87] I. M. Hall, *Experimental and computational K-shell spectroscopy of laser produced plasmas*, Ph.D. thesis, University of York (2006)

[88] Dr. Ingo Uschmann, University of Jena - Private Correspondence 2011

[89] B. L. Henke, J. Y. Uejio, G. F. Stone, C. H. Dittmore and F. G. Fujiwara, *High-energy x-ray response of photographic films: models and measurement*, J. Opt. Soc. Am. B, **3**(11), 1540 (1986)

[90] Institute for Optics G. Hoelzer, courtesy of I. Uschmann and University of Jena quantum electronic

[91] A. Pak, G. Gregori, J. Knight, K. Campbell, D. Price, B. Hammel, O. L. Landen and S. H. Glenzer, *X-ray line measurements with high efficiency Bragg crystals*, Review of Scientific Instruments, **75**(10) (2004)

[92] H. Legall, H. Stiel, A. Antonov, I. Grigorieva, V. Arkadiev *et al.*, *A new generation of X-ray optics based on pyrolytic graphite*, pp. 798–801 (2006)

[93] ESRF, Version 2.3, 2011 - Freely downloadable at http://www.esrf.eu/computing/scientific/xop2.1

[94] H. Legall, H. Stiel, V. Arkadiev and A. A. Bjeoumikhov, *High spectral resolution x-ray optics with highly oriented pyrolytic graphite*, Opt. Express, **14**(10), 4570 (2006)

[95] Manuel Sanchez del Rio, Mauro Gambaccini, Giovanni Pareschi, Angelo Taibi, Alessandra Tuffanelli and Andreas K. Freund, *Focusing properties of mosaic crystals* (1998)

[96] University of Rochester, *Laboratory for Laser Energetics Review 66 p. 60, DOE/SF/19460-125*

[97] S.A. Pikuz, A.Ya. Faenov, J. Colgan, R.J. Dance, J. Abdallah, E. Wagenaars, N. Booth, O. Culfa, R.G. Evans, R.J. Gray, T. Kaempfer, K.L. Lancaster, P. McKenna, A.L. Rossall, I.Yu. Skobelev, K.S. Schulze, I. Uschmann, A.G. Zhidkov and N.C. Woolsey, *Measurement and simulations of hollow atom X-ray spectra of solid-density relativistic plasma created by high-contrast $\{PW\}$ optical laser pulses*, High Energy Density Physics, **9**(3), 560 (2013), ISSN 1574-1818

[98] A. Ya. Faenov, A. I. Magunov, T. A. Pikuz, I. Yu. Skobelev, S. A. Pikuz, A. M. Urnov, J. Abdallah, R. E. H. Clark, J. Cohen, R. P. Jonson, G. A. Kyrala, M. D. Wilke, A. Maksimchuk, D. Umstadter, N. Nantel, R. Doron, E. Behar, P. Mandelbaum, J. J. Schwob, J. Dubau, F., B. Rosmej and A. Osterheld, *High-Resolved X-ray Spectra of Hollow Atoms in a Femtosecond Laser-Produced Solid Plasma*, Physica Scripta, **T80**, 536 (1999)

[99] P. M. Nilson, W. Theobald, J. F. Myatt, C. Stoeckl, M. Storm, J. D. Zuegel, R. Betti, D. D. Meyerhofer and T. C. Sangster, *Bulk heating of solid-density plasmas during high-intensity-laser plasma interactions*, Phys. Rev. E, **79**, 016406 (2009)

[100] K. U. Akli, S. B. Hansen, A. J. Kemp, R. R. Freeman, F. N. Beg, D. C. Clark, S. D. Chen, D. Hey, S. P. Hatchett, K. Highbarger, E. Giraldez, J. S. Green, G. Gregori, K. L. Lancaster, T. Ma, A. J. MacKinnon, P. Norreys, N. Patel, J. Pasley, C. Shearer, R. B. Stephens, C. Stoeckl, M. Storm, W. Theobald, L. D. Van Woerkom, R. Weber and M. H. Key, *Laser Heating of Solid Matter by Light-Pressure-Driven Shocks at Ultrarelativistic Intensities*, Phys. Rev. Lett., **100**, 165002 (2008)

[101] Ch. Reich, P. Gibbon, I. Uschmann and E. Förster, *Yield Optimization and Time Structure of Femtosecond Laser Plasma K-α Sources*, Phys. Rev. Lett., **84**, 4846 (2000)

[102] H.-S. Park, D. M. Chambers, H.-K. Chung, R. J. Clarke, R. Eagleton, E. Giraldez, T. Goldsack, R. Heathcote, N. Izumi, M. H. Key, J. A. King, J. A. Koch, O. L. Landen, A. Nikroo, P. K. Patel, D. F. Price, B. A. Remington, H. F. Robey, R. A. Snavely, D. A. Steinman, R. B. Stephens, C. Stoeckl, M. Storm, M. Tabak, W. Theobald, R. P. J. Town, J. E. Wickersham and B. B. Zhang, *High-energy K alpha radiography using high-intensity, short-pulse lasers*, Physics of Plasmas, **13**(5), 056309 (2006)

[103] J. R. Davies, *Alfvén limit in fast ignition*, Phys. Rev. E, **69**, 065402 (2004)

[104] K. U. Akli, M. J. Storm, M. McMahon, S. Jiang, V. Ovchinnikov, D. W. Schumacher, R. R. Freeman, G. Dyer and T. Ditmire, *Time dependence of fast electron beam divergence in ultraintense laser-plasma interactions*, Phys. Rev. E, **86**, 026404 (2012)

[105] V. T. Tikhonchuk, *Interaction of a beam of fast electrons with solids*, Physics of Plasmas (1994-present), **9**(4), 1416 (2002)

[106] M Nakatsutsumi, R Kodama, Y Aglitskiy, K U Akli, D Batani, S D Baton, F N Beg, A Benuzzi-Mounaix, S N Chen, D Clark, J R Davies, R R Freeman, J Fuchs, J S Green, C D Gregory, P Guillou, H Habara, R Heathcote, D S Hey, K Highbarger, P Jaanimagi, M H Key, M Koenig, K Krushelnick, K L Lancaster, B Loupias, T Ma, A Macphee, A J Mackinonn, K Mima, A Morace, H Nakamura, P A Norrys, D Piazza, C Rousseaux, R B Stephans, M Storm, M Tampo, W Theobald, L V Woerkom, R L Weber, M S Wei and N C Woolsey, *Heating of solid target in electron refluxing dominated regime with ultra-intense laser*, Journal of Physics: Conference Series, **112**(2), 022063 (2008)

[107] George A. Kyrala, *Cross calibration of AGFA-D7 x-ray film against direct exposure film from 2to8.5keV using laser generated x-rays*, Review of Scientific Instruments, **77**(5), 055104 (2006)

[108] M Nakatsutsumi, J R Davies, R Kodama, J S Green, K L Lancaster, K U Akli, F N Beg, S N Chen, D Clark, R R Freeman, C D Gregory, H Habara, R Heathcote, D S Hey, K Highbarger, P Jaanimagi, M H Key, K Krushelnick, T Ma, A MacPhee, A J MacKinnon, H Nakamura, R B Stephens, M Storm, M Tampo, W Theobald, L Van Woerkom, R L Weber, M S Wei, N C Woolsey and P A Norreys, *Space and time resolved measurements of the heating of solids to ten million kelvin by a petawatt laser*, New Journal of Physics, **10**(4), 043046 (2008)

[109] R. G. Evans, E. L. Clark, R. T. Eagleton, A. M. Dunne, R. D. Edwards, W. J. Garbett, T. J. Goldsack, S. James, C. C. Smith, B. R. Thomas, R. Clarke, D. J. Neely and S. J. Rose, *Rapid heating of solid density material by a petawatt laser*, Appl. Phys. Lett., **86**(19), 191505 (2005), ISSN 00036951

[110] Ozgur Culfa, University of York - Private Correspondence 2012

[111] A.G.R. Thomas, M. Tzoufras, A.P.L. Robinson, R.J. Kingham, C.P. Ridgers, M. Sherlock and A.R. Bell, *A review of VlasovFokkerPlanck numerical modeling of inertial confinement fusion plasma*, Journal of Computational Physics, **231**(3), 1051 (2012), ISSN 0021-9991, special Issue: Computational Plasma Physics Special Issue: Computational Plasma Physics

[112] H.-K. Chung, M.H. Chen, W.L. Morgan, Y. Ralchenko and R.W. Lee, *FLYCHK: Generalized population kinetics and spectral model for rapid spectroscopic analysis for all elements*, High Energy Density Physics, **1**(1), 3 (2005), ISSN 1574-1818

[113] Xiaohu Yang, Han Xu, Hongbin Zhuo, Yanyun Ma, Fuqiu Shao, Yan Yin and Marco Borghesi, *Effects of buried high-Z layers on fast electron propagation*, The European Physical Journal D, **68**(2), 1 (2014), ISSN 1434-6060

[114] R.G. Evans, *Modelling short pulse, high intensity laser plasma interactions*, High Energy Density Physics, **2**(12), 35 (2006), ISSN 1574-1818

[115] D A Chapman, S J Hughes, D J Hoarty and D J R Swatton, *Hot electron transport modelling in fast ignition relevant targets with non-Spitzer resistivity*, Journal of Physics: Conference Series, **244**(2), 022031 (2010)

[116] G. Gregori, A. Ravasio, C. D. Murphy, K. Schaar, A. Baird, A. R. Bell, A. Benuzzi-Mounaix, R. Bingham, C. Constantin, R. P. Drake, M. Edwards, E. T. Everson, C. D. Gregory, Y. Kuramitsu, W. Lau, J. Mithen, C. Niemann, H.-S. Park, B. A. Remington, B. Reville, A. P. L. Robinson, D. D. Ryutov, Y. Sakawa, S. Yang, N. C. Woolsey, M. Koenig and F. Miniati, *Generation of scaled protogalactic seed magnetic fields in laser-produced shock waves*, Nature, **481**, 480 (2012)

[117] Lyman Spitzer and Richard Härm, *Transport Phenomena in a Completely Ionized Gas*, Phys. Rev., **89**, 977 (1953)

[118] A. R. Bell, J. R. Davies and S. M. Guerin, *Magnetic field in short-pulse high-intensity laser-solid experiments*, Phys. Rev. E, **58**, 2471 (1998)

[119] S. M Vinko, O Ciricosta, B. I. Cho, K. Chung Engelhorn, C. R. D. H.-K. Brown, T. Burian, J. Chalupsky, R. W. Falcone, C. Graves, V. Hajkova, A. Higginbotham, L. Juha, J. Krzywinski, H. J. Lee, M. Messerschmidt, C. D. Murphy, Y. Ping, A. Scherz, W. Schlotter, S. Toleikis, J. J. Turner, L. Vysin,

T. Wang, B. Wu, U. Zastrau, D. Zhu, R. W. Lee, P. A. Heimann, B. Nagler and J. S. Wark, *Creation and diagnosis of a solid-density plasma with an X-ray free-electron laser*, Nature, **482**, 59 (2012)

[120] *Femtosecond electronic response of atoms to ultra-intense X-rays*, **466**(7302), 56 (2010), ISSN 7302

[121] Igor Yu Skobelev, A Ya Faenov, Tat'yana A Pikuz and Vladimir E Fortov, *Spectra of hollow ions in an ultradense laser plasma*, Physics-Uspekhi, **55**(1), 47 (2012)

[122] J. Colgan, J. Abdallah, A. Ya. Faenov, S. A. Pikuz, E. Wagenaars, N. Booth, O. Culfa, R. J. Dance, R. G. Evans, R. J. Gray, T. Kaempfer, K. L. Lancaster, P. McKenna, A. L. Rossall, I. Yu. Skobelev, K. S. Schulze, I. Uschmann, A. G. Zhidkov and N. C. Woolsey, *Exotic Dense-Matter States Pumped by a Relativistic Laser Plasma in the Radiation-Dominated Regime*, Phys. Rev. Lett., **110**, 125001 (2013)

[123] S. B. Hansen, J. Colgan, A. Ya. Faenov, J. Abdallah, S. A. Pikuz, I. Yu. Skobelev, E. Wagenaars, N. Booth, O. Culfa, R. J. Dance, G. J. Tallents, R. G. Evans, R. J. Gray, T. Kaempfer, K. L. Lancaster, P. McKenna, A. K. Rossall, K. S. Schulze, I. Uschmann, A. G. Zhidkov and N. C. Woolsey, *Detailed analysis of hollow ions spectra from dense matter pumped by xray emission of relativistic laser plasma*, Physics of Plasmas, **21**(3) (2014)

[124] James H. Scofield, *Radiative Decay Rates of Vacancies in the K and L Shells.*, Phys. Rev., **179**, 9 (1969)

[125] National Institute of Standards and Technology Spectral Lines Database - http://www.nist.gov/pml/data/asd.cfm

[126] Centre for X-Ray Optics, *X-Ray Data Booklet* (Lawrence Berkeley National Laboratory, 2009)

[127] G. Cristoforetti, M. P. Anania, A. Ya. Faenov, A. Giulietti, D. Giulietti, S. B. Hansen, P. Koester, L. Labate, T. Levato, T. A. Pikuz and L. A. Gizzi, *Spatially resolved analysis of K_α x-ray emission from plasmas induced by a femtosecond weakly relativistic laser pulse at various polarizations*, Phys. Rev. E, **87**, 023103 (2013)

[128] R. Stephens, R. A. Snavely, Y. Aglitskiy, F. Amiranoff, C. Andersen, D. Batani, S. D. Baton, T. Cowan, R. R. Freeman, T. Hall, S. P. Hatchett, J. M. Hill, M. H. Key, J. A. King, J. A. Koch, M. Koenig, A. J. MacKinnon, K. L. Lancaster, E. Martinolli, P. Norreys, E. Perelli-Cippo, M. Rabec Le Gloahec, C. Rousseaux, J. J. Santos and F. Scianitti, *K-alpha uorescence measurement of relativistic electron transport in the context of fast ignition*, Phys. Rev. E, **69**, 066414 (2004)

[129] R. D. Cowan, *Theory of Atomic Spectra* (University of California Press, Berkeley, 1981)

[130] J. Colgan, J. Abdallah Jr., A. Ya. Faenov, T.A. Pikuz, I. Yu. Skobelev, Y. Fukuda, Y. Hayashi, A. Pirozhkov, K. Kawase, T. Shimomura, H. Kiriyama, Y. Kato, S.V. Bulanov and M. Kando, *Observation and modeling of high resolution spectral features of the inner-shell X-ray emission produced by 1010 contrast femtosecond-pulse laser irradiation of argon clusters*, High Energy Density Physics, **7**(2), 77 (2011), ISSN 1574-1818

[131] M. I. K. Santala, Z. Najmudin, E. L. Clark, M. Tatarakis, K. Krushelnick, A. E. Dangor, V. Malka, J. Faure, R. Allott and R. J. Clarke, *Observation of a Hot High-Current Electron Beam from a Self-Modulated Laser Wakefield Accelerator*, Phys. Rev. Lett., **86**, 1227 (2001)

[132] T. E. Cowan, A. W. Hunt, T. W. Phillips, S. C. Wilks, M. D. Perry, C. Brown, W. Fountain, S. Hatchett, J. Johnson, M. H. Key, T. Parnell, D. M. Pennington, R. A. Snavely and Y. Takahashi, *Photonuclear Fission from High Energy Electrons from Ultraintense Laser-Solid Interactions*, Phys. Rev. Lett., **84**, 903 (2000)

[133] K. W. D. Ledingham, I. Spencer, T. McCanny, R. P. Singhal, M. I. K. Santala, E. Clark, I. Watts, F. N. Beg, M. Zepf, K. Krushelnick, M. Tatarakis, A. E. Dangor, P. A. Norreys, R. Allott, D. Neely, R. J. Clark, A. C. Machacek, J. S. Wark, A. J. Cresswell, D. C. W. Sanderson and J. Magill, *Photonuclear Physics when a Multiterawatt Laser Pulse Interacts with Solid Targets*, Phys. Rev. Lett., **84**, 899 (2000)

[134] M. Honda, J. Meyer ter Vehn and A. Pukhov, *Two-dimensional particle-in-cell simulation for magnetized transport of ultra-high relativistic currents in plasma*, Phys. Plasmas, **7**(4), 1302 (2000), ISSN 1070664X

[135] Y. Inubushi, Y. Okano, H. Nishimura, H. Cai, H. Nagatomo, T. Kai, T. Kawamura, D. Batani, A. Morace, R. Redaelli, C. Fourment, J. J. Santos, G. Malka, A. Boscheron, O. Bonville, J. Grenier, Ph. Canal, B. Lacoste, C. Lepage, L. Marmande, E. Mazataud, A. Casner, M. Koenig, S. Fujioka, T. Nakamura, T. Johzaki and K. Mima, *X-ray polarization spectroscopy to study anisotropic velocity distribution of hot electrons produced by an ultra-high-intensity laser*, Phys. Rev. E, **81**, 036410 (2010)

[136] J. C. Kieffer, J. P. Matte, H. Pépin, M. Chaker, Y. Beaudoin, T. W. Johnston, C. Y. Chien, S. Coe, G. Mourou and J. Dubau, *Electron distribution anisotropy in laser-produced plasmas from x-ray line polarization measurements*, Phys. Rev. Lett., **68**, 480 (1992)

[137] J. C. Kieffer, J. P. Matte, M. Chaker, Y. Beaudoin, C. Y. Chien, S. Coe, G. Mourou, J. Dubau and M. K. Inal, *X-ray-line polarization spectroscopy in laser-produced plasmas*, Phys. Rev. E, **48**, 4648 (1993)

[138] Peter Hakel, Roberto C. Mancini, Jean-Claude Gauthier, Emilio M'inguez, Jacques Dubau and Marguerite Cornille, *X-ray line polarization of He-like Si satellite spectra in plasmas driven by high-intensity ultrashort pulsed lasers*, Phys. Rev. E, **69**, 056405 (2004)

[139] N.C. Woolsey, R.J. Clarke, D. Doria, L.A. Gizzi, G. Gregori, P. Hakel, S.B. Hansen, P. Koester, L. Labate, T. Levato, B. Li, M. Makita, R.C. Mancini, J. Pasley, P.P. Rajeev, A.P.L. Robinson, E. Wagenaars, J.N. Waugh and N. Booth, *Precision X-ray spectroscopy of intense laser-plasma interactions*, High Energy Density Physics, **7**(2), 105 (2011), ISSN 1574-1818

[140] WenXi Liang, YuTong Li, MiaoHua Xu, XiaoHui Yuan, ZhiYuan Zheng, Yi Zhang, Feng Liu, ZhaoHua Wang, HanMing Li, Zhan Jin, ZhiYi Wei, Wei Zhao, YingJun Li and Jie Zhang, *Study of hot electrons generated from intense laser-plasma interaction employing Image Plate*, Science in China Series G: Physics Mechanics and Astronomy, **51**, 1455 (2008), ISSN 1672-1799, 10.1007/s11433-008-0146-y

[141] RR Freeman, D Batani, S Baton, M Key and R Stephens, *The generation and transport of large currents in dense materials: The physics of electron transport relative to fast ignition*, Fusion science and technology, **49**(3), 297 (2006)

[142] S. N. Chen, P. K. Patel, H.-K. Chung, A. J. Kemp, S. Le Pape, B. R. Maddox, S. C. Wilks, R. B. Stephens and F. N. Beg, *X-ray spectroscopy of buried layer foils irradiated at laser intensities in excess of 1020W/cm2*, Physics of Plasmas (1994-present), **16**(6), 062701 (2009)

[143] P. McKenna, A. P. L. Robinson, D. Neely, M. P. Desjarlais, D. C. Carroll, M. N. Quinn, X. H. Yuan, C. M. Brenner, M. Burza, M. Coury, P. Gallegos, R. J. Gray, K. L. Lancaster, Y. T. Li, X. X. Lin, O. Tresca and C.-G. Wahlstrom, *Effect of Lattice Structure on Energetic Electron Transport in Solids Irradiated by Ultraintense Laser Pulses*, Phys. Rev. Lett., **106**, 185004 (2011)